Dissertation zur Erlangung des Doktorgrades

der Fakultät für Chemie und Pharmazie

der Ludwig-Maximilians-Universität München

Synthesis and Applications of Inorganic-Organic Hybrid Materials

von

Norma Karla Minar

aus

Zeitz, Deutschland

2014

Erklärung

Diese Dissertation wurde im Sinne von §7 der Promotionsordnung vom 28. November 2011 von Herrn Prof. Dr. Thomas Bein von der Fakultät für Chemie und Pharmazie betreut.

Eidesstattliche Versicherung

Diese Dissertation wurde eigenständig und ohne unerlaubte Hilfe erarbeitet.

München, den 11. Oktober 2014

Dissertation eingereicht am 13.10.2014

1. Gutachter: Prof. Dr. Thomas Bein
2. Gutachter: Prof. Dr. Konstantin Karaghiosoff

Mündliche Prüfung am 11.11.2014

"The most exciting phrase in science, the one that heralds new discoveries, is not 'EUREKA!' but '*That's funny...*'."

Isaac Asimov (1920 - 1992)

Danksagung

An erster Stelle möchte ich mich ganz herzlich bei meinem Doktorvater Prof. Thomas Bein für das entgegengebrachte Vertrauen und die Unterstützung in den vergangenen Jahren während meiner Doktorarbeit bedanken. Durch die sehr interessanten und immer wieder herausfordernden Projekte im Grenzbereich zwischen Materialwissenschaften und Nanochemie konnte ich meinen 'chemischen' Horizont stark erweitern. Eine große Hilfe dabei war der nahezu perfekt ausgestattete 'Analytik-Gerätepark T.Bein'. Vor allem die große Freiheit zu eigenverantwortlicher Forschung habe ich in den letzten Jahren sehr zu schätzen gelernt. Auch möchte ich mich für die zahlreichen Möglichkeiten, verschiedene Konferenzen und Meetings im In- und Ausland besuchen zu können, bedanken. Vielen Dank Thomas!

Prof. Konstantin Karaghiosoff möchte ich dafür danken, dass er ohne zu zögern die Aufgabe des Zweitgutachters übernommen hat und immer wieder großes Interesse an unserer Forschung zeigt.

Prof. Dina Fattakhova-Rohlfing möchte ich für die vielen hilfreichen Diskussionen, Ratschläge und Ideen danken. Auch für ihre Hilfe bei der Koordination von möglichen Kooperationen bin ich ihr dankbar.

Bei meinem Kooperationspartner Christian Westermeier aus der Physik möchte ich mich für die sehr gute Zusammenarbeit auf dem Gebiet der Kapazitätsmessungen und die interessanten 'Physikgespräche' bedanken. Dank gilt natürlich auch seinem

Chef PD Dr. Bert Nickel für das zur Verfügung gestellte Equipment. Professor Shinji Inagaki vom Toyota Central R & D Labs aus Japan danke ich für die organische Synthese des Startmaterials für elektroaktive PMO Materialien. Kun Hou danke ich für die umfangreiche synthetische Arbeit im Projekt der kovalenten Fulleren-Netzwerke. Für die gute Starthilfe am Anfang meiner Doktorarbeit (bzw. noch davor während meiner Diplomarbeit) mit vielen hilfreichen Tipps und Ratschlägen (aber auch vielen netten Späßen [Oliver, er spielt longline, longline! Oliver!]) bin ich Dr. Johann Szeifert sehr dankbar.

Auch Dr. ('Lord') Docampo danke ich für die große Mithilfe beim Verfassen und Korrigieren des Manuskriptes über die in-situ Polymerisation. Prof. Laurie Peter und Dr. Yan Li möchte ich für die sehr konstruktive und schnelle Hilfe per Email danken. Dr. Florian Auras danke ich für die zahlreichen Diskussionen über 'High'-Performance Solarzellen und die Hilfsbereitschaft bei jedem photovoltaischen Problemchen.

Meinen Praktikanten Sergio, Liz, Elliard, Michi, Bianca, Enrico und Henrik gebührt großer Dank für die zahlreichen Experimente und Messungen im Labor. Besonders möchte ich meinem Bachelor-Studenten Stephan danken, der das Projekt der in-situ Polymerisation durch viel kreative Eigenleistung ein ganzes Stück vorangebracht hat.

Allen Kollegen aus dem Arbeitskreis Bein bin ich sehr dankbar für all die Unterstützung egal ob im Wissenschaftsalltag oder bei privaten Angelegenheiten. Ich habe die Zeit mit all den Unternehmungen wie zum Beispiel Wandertagen, Stammtischabenden, Weihnachtsfeiern und Skitagen sehr genossen und möchte sie nicht missen!

Meinen zahlreichen Bürokumpanen angefangen mit Johann, Benni, Hans, Aurator, Stefan und Fabi bin ich dankbar für die (zumeist) sehr angenehme Atmosphäre bis hin zu Markus für die nette Aufnahme in sein '3er'-Büro (Doktor Döblingers geschmackvolles Kasperltheater). Mona möchte ich für ihren unverbesserlichen Optimismus danken und Basti für seine scheinbar unerschöpfliche Hilfsbereitschaft und

Expertise (in fast Allem). Bini danke ich für die gute Versorgung mit bolivianischem Mate-Tee, ohne den ich die Endphase nicht so gut durchgestanden hätte.
Und nun zu den mitunter wichtigsten Personen die uns allen eigentlich erst einen so reibungslosen Forschungsalltag ermöglichen: Tina und Regina.
Tina, vielen vielen Dank, dass Du unermüdlich versuchst das überall lauernde Chaos zurück zu drängen und uns somit eine super Grundlage für gute Forschung schaffst.
Regina, Dir möchte ich herzlich danken, dass Du Dir immer all unsere Wehwehchen anhörst und das organisatorische und administrative Chaos im Schach hältst. Ohne Dich wären wir manchmal ganz schön verloren.
Hans, Dir möchte ich dafür danken, dass Du mich, vor allem in der Endphase, so gut persönlich und auch wissenschaftlich 'gemanaged' hast!
Besonderer Dank gilt meiner Familie die mein Interesse an der Wissenschaft geweckt und immer gefördert hat. Danke für die persönliche und finanzielle Unterstützung, ohne die mein bisheriger Werdegang so nicht möglich gewesen wäre! Danke!

Abstract

The demands on modern products and components rise relentlessly. As a result, increasingly higher requirements on the properties and the performance of the constituent materials are imposed. For example, in modern transportation vehicles an ultra-light weight construction is desired in addition to strength and stiffness to decrease the fuel consumption. Other fields of application, such as photovoltaic or optoelectronic devices in general, require new efficient materials with optimized properties for light-absorption and charge transfer.

The research field of hybrid inorganic-organic materials offers vast potential through the nearly endless possible combinations of building blocks, allowing for the development of customized intriguing properties.

In this work two different concepts to synthesize functional hybrid inorganic-organic materials were developed. On the one hand, a hybrid material was produced by covalently linking a conducting polymer to a mesoporous metal oxide scaffold by in-situ polymerization starting from a grafted molecular linker. The other concept employed the application of soft-templating methods to organosilica materials chemistry, enabling the development of periodically structured hybrid materials with tuneable optoelectronic properties.

In the first project we incorporated the conducting polymer poly(2-methoxy-5-(2'-ethylhexyloxy)-p-phenylene vinylene) (MEH-PPV) into surface-functionalized meso-

porous titania films *via* in-situ polymerization. The influence of the titania surface functionalization on the amount (absorbance) and quality (optical band gap) of the synthesized MEH-PPV was investigated via UV-Vis spectroscopy. Surface functionalization with linker molecules mimicking the monomer or its activated form, respectively, resulted in a greatly enhanced absorbance and a smaller band gap of the grafted polymer compared to samples obtained with non-functionalized titania scaffolds. The performance of the differently attached polymer chains in photovoltaic devices was examined. Shunting or series resistance limitations of the devices can be observed depending on the surface functionalization prior to in-situ polymerization of MEH-PPV. The results help to draw conclusions about the parameters, such as interface connection and orientation of the polymer chains, which are essential for an efficiently working MEH-PPV-titania hybrid material.

A greatly different synthesis method for hybrid materials on the atomic scale is to employ organically bridged silsesquioxane precursors to build a periodic network by soft-templating. This synthesis concept for periodic mesoporous organosilica (PMO) was applied in the second and third project.

In the second project a highly symmetric fullerene framework based on a functionalized C_{60} fullerene building block was successfully synthesized. The octahedral addition pattern of the building block was designed to facilitate the self-assembly process with an amphiphilic block-copolymer. The orthorhombic structure with *Fmmm* symmetry and 7.5 nm pores was investigated with small-angle X-ray scattering (SAXS) and transmission electron microscopy (TEM), while solid-state NMR experiments confirmed the integrity of the fullerene core and provided insights into the degree of condensation of the fullerene building blocks. A BET surface area of 494 $m^2\,g^{-1}$ and a total pore volume of 0.34 $m^3\,g^{-1}$ were observed via N_2 sorption. In addition to the structural information, the electronic properties of thin fullerene

PMO films were investigated using transistor and capacitance measurements, carried out in collaboration with Christian Westermeier of the group of Prof. B. Nickel (LMU, physics department). The fullerene PMO framework exhibits a low dielectric constant of around 3 in a frequency range from 100 kHz to 1 MHz.

The third project dealt with the synthesis and characterization of a PMO material based on an optically active donor-acceptor-donor unit. The synthesis of the dithienyl-benzothiadiazole (DTBT) silsesquioxane precursor was carried out in the group of Prof. Inagaki (Toyota Central R&D Labs., Inc). Applying the evaporation-induced self-assembly (EISA) approach with the block copolymer F127 serving as template, a lamellar mesostructure was formed with the DTBT silsesquioxane precursor. After a stabilizing vapor treatment with HCl and tetraethyl orthosilcate (TEOS), the structure converted into an approximately hexagonal pore arrangement, as demonstrated by SAXS and TEM measurements. Remarkably, the structure is not prone to shrinkage upon heating and template removal, showing a large *d*-spacing of 14.5 nm. The porosity was investigated by N_2 sorption, which revealed a BET surface area of 92 $m^2\,g^{-1}$. Due to the planarity of the DTBT unit, the molecule has a strong tendency to form π-stacks. The π-π interactions and the packing of the DTBT units inside the walls of the structured network were examined by wide-angle X-ray scattering as well as UV-Vis and photoluminescence (PL) spectroscopy. The results from these measurements showed a strong influence of the HCl-TEOS vapor treatment on the π-interactions of the DTBT units: the π interactions of the DTBT units vanished through the structure formation and hydrolysis, seen in a blue-shift of the UV-Vis absorbance and the disappearance of a longer-lived PL process. Thin films of the structured porous DTBT organosilica were also tested in photovoltaic devices as electron donor materials. The photovoltaic performance of dense films of hydrolyzed DTBT precursor alone is higher compared to porous structured DTBT

films, which is attributed to the introduction of insulating silica (50 wt%) during the structure formation process.

The fourth and last part is focused on the synthesis of a structured fullerene-silica hybrid material via a sol-gel route. In contrast to the two preceding projects a co-condensation approach of a hydroxylated fullerene and a silica precursor was used instead of silsesquioxane precursors.

The number of hydroxy groups added to the fullerene was selected to achieve a solubility of the resulting fullerenol suitable for polar solvents used in the EISA approach. The homogeneous mesophases, produced with the templates P123 and F127, inherit over 80 wt% fullerenol in the organosilica phase. The structural properties were characterized with SAXS, 2D grazing-incidence small-angle X-ray scattering and TEM. Fullerenol-silica films templated with P123 shows a lamellar structure oriented parallel to the substrate, and with F127 a more disordered structure of possibly non-oriented lamellar domains. Remarkably, both structures show a high thermal stability. The organosilica templated with P123 shows a high porosity with a BET surface area of 180 $m^2\,g^{-1}$ revealed by N_2 sorption. The integration of the fullerenol moieties into a stable porous network opens the posssiblity to study this material in various applications.

Contents

Chapter 1

Introduction to Hybrid Organic-Inorganic Materials

Over 50 years ago Richard Feynman gave his famous talk 'There's Plenty of Room at the Bottom'[1] and in this way became one of the 'founding fathers' of nanotechnology. He envisioned a technological journey towards the atomic scale and even set up two 'nano'-challenges with 1000 $ reward for each: One was to build a motor smaller than 0.4 mm, the other one to scale down a whole book page by a factor of 25 000.

Both challenges are already fulfilled, but nanotechnology still is viewed as the technology of the future - *the* technology of the 21st century. *Nano* and *hybrid* today are popular buzzwords for entrepreneurs and scientists similar to *micro* in the 70s and 80s (e.g. Microsoft, AMD - Advanced Micro Devices) and the prefix *e-* in the 90s (e.g. eBanking, eGovernment, eBusiness, etc.). However, nano- and hybrid materials are part of human culture and knowledge since ancient times: for example, many ancient pigments such as 'Egyptian'[2] or 'Mayan' Blue[3] are based on nanostructured and/or hybrid materials. However, it was not until the end of the 20th century that scientists realized the cornucopia of possibilities for new materials that

opened up through the field of nanoscience. One major reason for the rise of the nanosciences was the availability of novel physico-chemical characterization methods, such as electron and atomic-force microscopy, that gave novel insights into the properties of nanomaterials.

The term nanotechnology refers to objects and research on a scale from the atomic level up to 100 nm ($100 \cdot 10^{-9}$ m). At these extremely small dimensions, materials exhibit modified properties such as color, melting point, catalytic activity, reactivity and other electronic or magnetic properties, compared to bulk material. This "size effect" is often related to the increased fraction of surface atoms compared to the total number of atoms, or to changes in the electronic structure with shrinking dimensions.[4]

In principle there exist two basic approaches for the synthesis of nanostructures: the *bottom-up* and the *top-down* approach. Typical examples for a top-down approach are milling for nanoparticle synthesis or lithographic etching processes to nanostructure thin films. Bottom-up methods are more versatile and include, e.g., building up structures atom-by-atom, growing crystals or polymers, or the deposition of thin films.[5]

An interesting group of nanomaterials is the class of hybrid materials, which interfaces two worlds of chemistry - organics and inorganics - with the intention to seek for synergistic effects.[6] Nature offers many examples of hybrid materials with unique and intriguing properties such as bone tissue or nacre. One definition of 'hybrid materials' is the following: a material that includes two differing moieties blended on the molecular scale is called a hybrid material.[7]

Depending on the type of interactions between the two moieties, hybrid materials can be categorized into two classes shown schematically in figure 1.1. Class I hybrid materials are characterized by weak interactions such as van der Waals, hydrogen

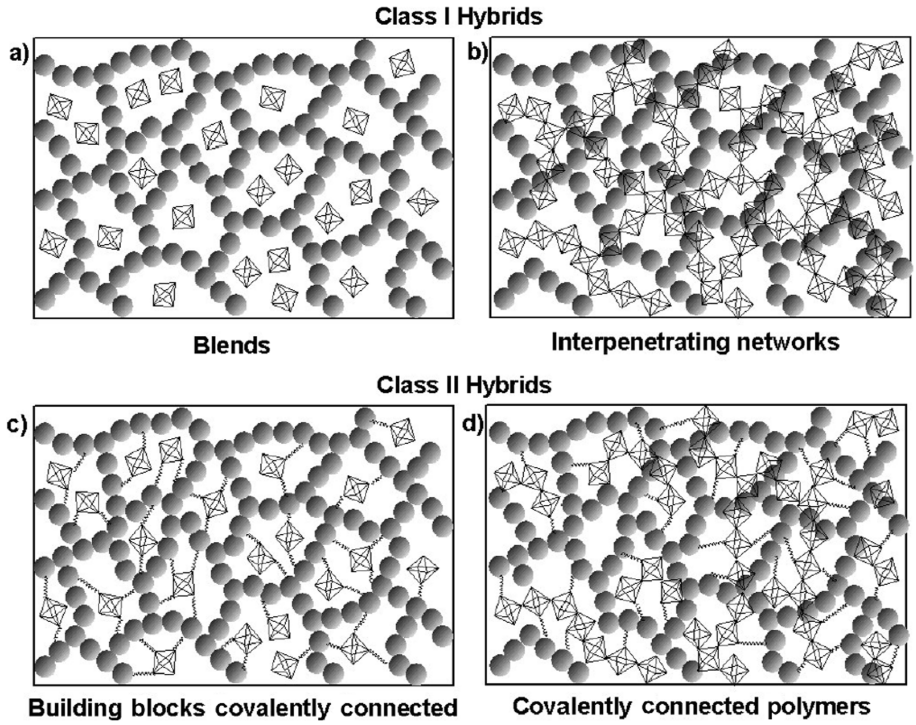

Figure 1.1: The different classes of hybrid materials based on the character of the interactions.[7]

bonding or weak electrostatic interactions between the two components. Contrary to this, the units in Class II hybrid materials are connected by strong chemical interactions such as covalent bonds.[7,8]

Given the multitude of available components and connectivities, it is obvious that hybrid materials comprise a vast space for materials design.

One frequent advantage of hybrid materials is increased mechanical strength based on the inorganic structures.[8] Furthermore, organic materials are often stabilized in an inorganic matrix. For example, the enhanced mechanical and thermal properties of conducting polymers obtained by the inclusion of inorganic units suggest these nanocomposites as a light-weight alternative to classical conductors based on metals.[7,9] Another favorable aspect relates to the mild reaction conditions such as solution-based processing and comparably low synthesis temperatures.[3]

The following introduction will provide the reader with background information on

the fundamental principles of the various materials syntheses studied in this work.

1 Porous Hybrid Materials Based on Sol-Gel Chemistry

1.1.1 The Sol-Gel Approach

The discovery of the silica sol-gel approach dates back as early as the middle of the 19th century, with J-J. Ebelmen performing first experiments.[10] But it took nearly one hundred years until, with the work of Geffcken and Berger[11], the potential for industrial applications was unleashed. They used the advantage of the sol-gel method as a wet chemistry route to form inorganic glasses at room temperature. The mild synthesis conditions open up the possibility to incorporate all kinds of organic compounds.

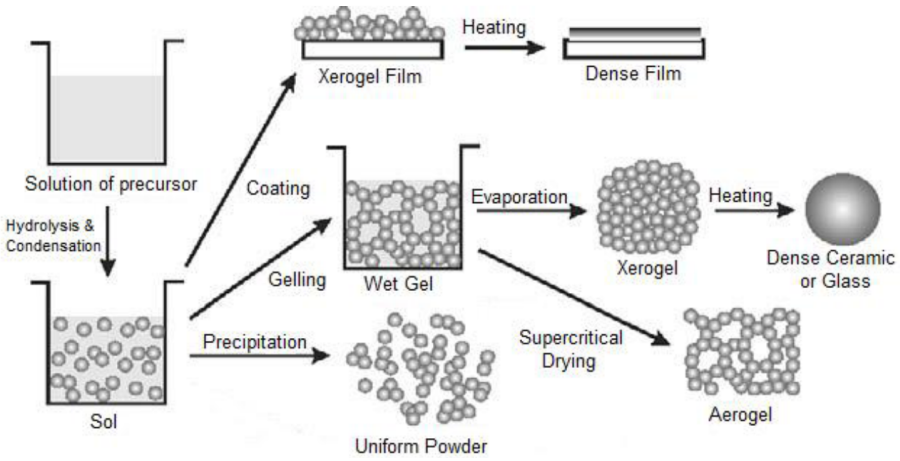

Figure 1.2: Overview of the synthesis steps and resulting materials of the sol-gel approach.[12]

The sol-gel process is based on the combination of hydrolysis and condensation reactions of metal halides or alkoxide precursors in water or oxygen-containing solvents.

Figure 1.2 shows an overview of the synthesis steps and the possible routes to various morphologies. In the first step of the sol-gel reaction the molecular precursor is transformed into inorganic oligo- and polymers. This hydrolysis reaction leads to the so-called *sol*, i.e. a colloidal suspension of the formed species. Further condensation of the sol results in an interconnected, porous inorganic network enclosing a continuous liquid phase - the *gel*. An *aerogel* is formed if the solvent is extracted under supercritical conditions. Aerogels are highly porous materials that are composed of over 90 % pore volume. Simple drying of the wet gel leads to *xerogels*, which exhibit a much lower porosity due to the partial collapse of the network. Ageing the gel under different reaction conditions has a great influence on the properties of the final material.[12]

Due to its enormous flexibility, the sol-gel approach is suitable for the synthesis of nanoparticles, dense or porous networks in the form of films, fibers or bulk material. Especially at the early stage of the sol synthesis, changing the reaction parameters, such as water/alkoxide ratio, pH and temperature enables the control over the particle size, crystallinity and morphology. An example is the pH-dependence of the sol morphology (c.f. figure 1.3): At low pH values the hydrolysis of the alkoxide precursor yields more polymer-like small partially cross-linked particles. Highly cross-linked colloidal, spherical particles, on the other hand, are formed in basic conditions.

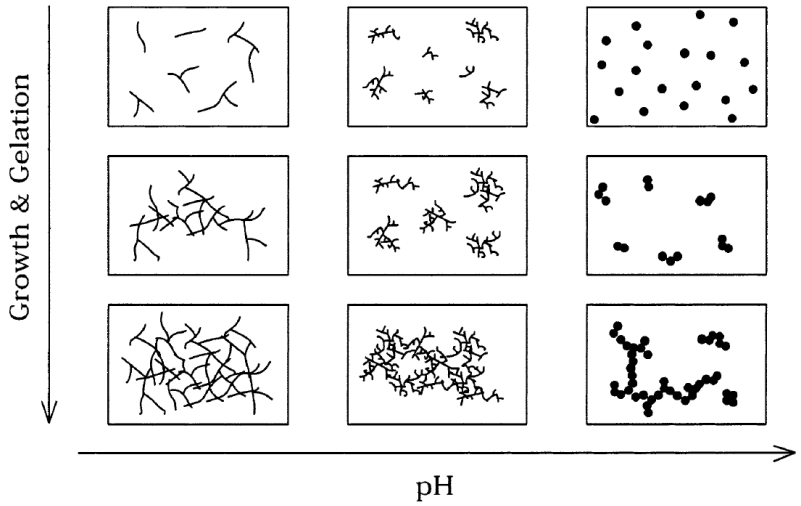

Figure 1.3: Schematic view on the effects of the pH value on the morphology of the synthesized silica sol.[13]

1.1.2 Surfactant-Templated Mesoporous Materials

Porous materials can be categorized according to IUPAC rules regarding their pore size into three classes: microporous (d < 2 nm), mesoporous (2 nm < d < 50 nm) and macroporous (d > 50 nm) materials.[14]

Although the aforementioned aerogels and xerogels exhibit a high mesoporosity, their pore size distributions are quite broad and the shape of the pores is typically irregular. An early and prominent example of controlling the pore size, shape and periodicity in solids by templates is the application of alkylammonium ions in zeolite syntheses developed at the Mobil Oil Corporation.[15]

The first ordered mesoporous silica materials were also discovered by Mobil company researchers by adapting a zeolite synthesis route, but applying amphiphilic longer-chain alkylammonium ions.[16] In polar solvents and at high concentrations, the amphiphilic molecules form micelles, which can act as a template for the resulting pores. Regarding its origin, this materials class was named MCM - Mobil Composition of Matter. The MCM family exhibits uniform pores of over 4 nm in size arranged in a long-range order, although the wall material is, different to ze-

olites, composed of amorphous silica. Even bigger pore diameters of up to 30 nm could be achieved a few years later by using larger block co-polymers as templates, for example in the SBA-15 silica, templated by non-ionic triblock co-polymers consisting of polyethylene and polypropylene blocks.[17]

These synthesis routes were originally designed to produce porous particles with various applications in different fields. However, for certain applications such as membranes, low-dielectric constant interlayers, sensors or optoelectronic devices thin films are indispensable. During first attempts towards sol-gel thin film synthesis a substrate was introduced into a solvent-template-silica system, with a high initial concentration of the surfactant such that a micellar mesophase was formed.[18,19]

The micelle formation of surfactant molecules at and above a critical micelle concentration (cmc) can be predicted by the so-called packing parameter P. Israelachvili et al. correlated the effective area of the hydrophobic head group a with the volume V of the hydrocarbon part and the length l_c of the hydrophobic tail (see equation 1.1 and figure 1.4).[20]

$$P = \frac{V}{a \cdot l_c} \tag{1.1}$$

The packing parameter and the resulting micellar assembly can be influenced not only by the structure of the surfactant used, but also by the polarity of the solvent and the presence of other ionic or non-ionic species.

A mechanism for the surfactant-templated film formation was introduced by Brinker and coworkers in 1999 with the concept of the evaporation-induced self-assembly (EISA). For the EISA approach the surfactant concentration in the homogeneous synthesis solution, including the inorganic precursor, is far below the cmc. By evaporation of the solvent during film synthesis, e.g. dip or spin coating, the surfactant concentration increases progressively. This drives the self-assembly of the surfactant-

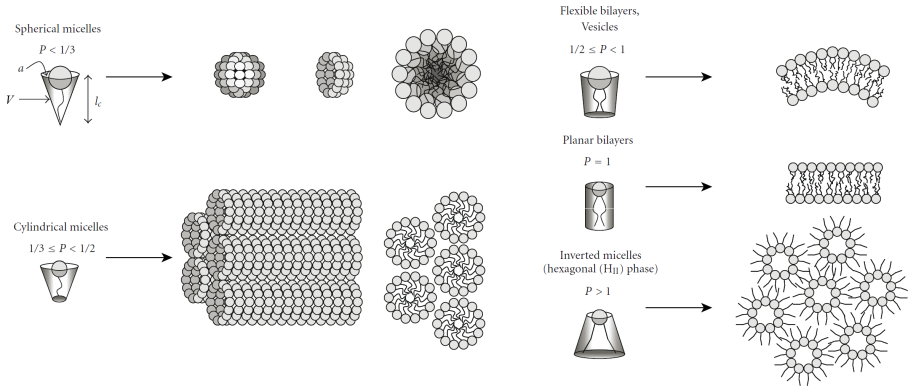

Figure 1.4: The different values of the packing parameters and the resulting micellar shapes.[21]

micelles and the inorganic precursor into a liquid-crystalline mesophase.[22]

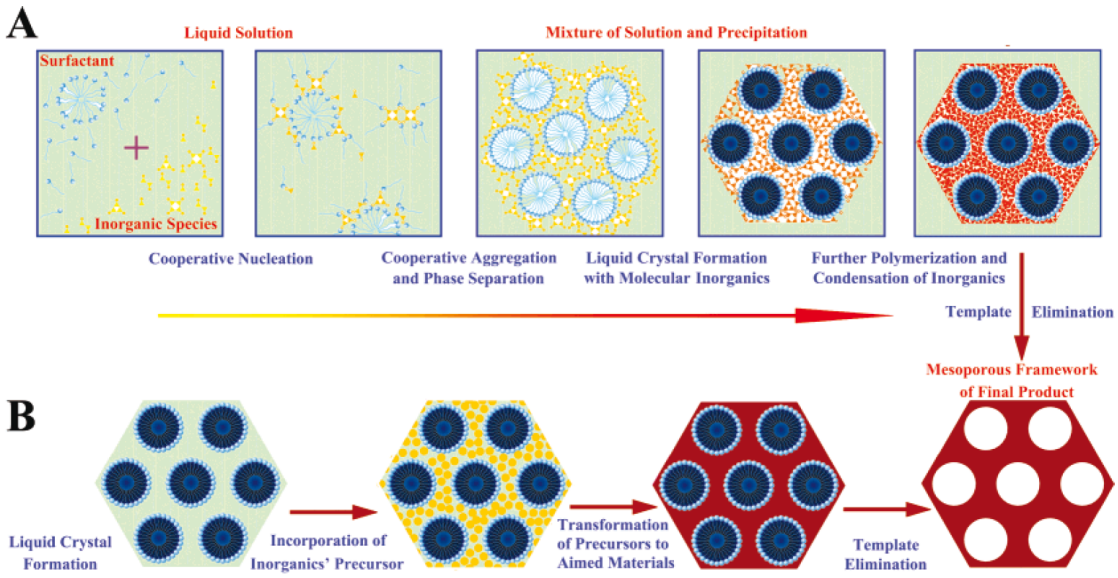

Figure 1.5: There are two proposed mechanisms for the structure formation of mesoporous materials by soft-templating: A: Cooperative self-assembly. B: 'True' liquid-crystal templating.[23]

Two different concepts are proposed for the assembly mechanism: On the one hand a cooperative self-assembly (CSA) mechanism is proposed with simultaneous assembly of the micelles and condensation of the inorganic species in the interstitial volume. On the other hand a liquid crystal templating (LCT) mechanism is discussed in which the template micelles build a stable mesophase in the first place. The in-

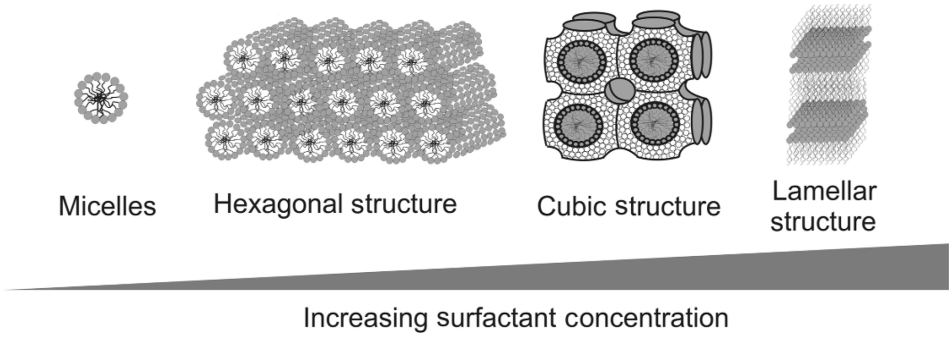

Figure 1.6: Examples of ordered 3D-structure obtained by self-assembly of amphiphilic surfactants.[7] This applies for example for the synthesis of nanostructured silica and titania with the template Pluronic® P123.[29]

dividual steps of the two proposed mechanisms are shown in figure 1.5. Several studies investigated the film formation process in detail, for example with in-situ grazing-incidence small-angle X-ray scattering.[24–26] It seems that depending on the chemical parameters and processing conditions the exact nature of the process is often a combination of both mechanisms.

A key parameter for the resulting 3D arrangement of the template-micelles is the ratio of inorganic precursor to surfactant and solvent.[27,28] Several parameters such as the composition and temperature together with the resulting mesophase can be summarized in a phase diagram, which can be an advantageous tool to reproduce or adapt a certain synthesis. A common trend for the type of mesophases depending on the surfactant concentration is shown in figure 1.6.

The synthesized films show liquid-crystalline behavior and in the so-called tuneable steady state the mesophase can still be influenced by factors such as solvent vapor or heat treatments.[28] This initial extraordinary flexibility of the mesophase was already shown by the group of G. D. Stucky in the early 90s. For example, a lamellar silica-template phase was transformed into a hexagonal micellar arrangement through a hydrothermal treatment.[30]

This concept was later expanded to the introduction of a gaseous inorganic precursor – tetraethyl orthosilicate – into a liquid-crystal mesophase of the plain template. In

this approach the lamellar phase of the pure template phase could be transformed into a hexagonally ordered stable silica structure.[31,32] Only recently, such a vapor phase synthesis was applied to a non-classical phospholipid template phase.[33]
Concluding, it can be said that the surfactant-templated synthesis of mesoporous materials is a delicate process with many crucial parameters that have to be tuned, but at the same time already numerous possibilities and alternative routes have been found due to the intensive research in this field in the last 20 years.

1.1.3 Periodic Mesoporous Organosilicas

Prior to the development of the sol-gel process there was, apart from the application of inorganic filler materials for organic polymers such as rubber, hardly any scientific activity on hybrid inorganic-organic materials.[7] The mild sol-gel reaction conditions allowed for the incorporation of organic components into an inorganic network. The special role of silica can be explained mainly by its good processability, flexibility for shaping and the stability of the Si-C bond during the network formation.[34]
In principle there exist three different routes for the synthesis of organic-silica porous hybrid materials: 1) post-synthetic modification (= *grafting*) of the porous surface of a purely inorganic silica material, 2) simultaneous condensation (= *co-condensation*) of the silica and organosilica precursor and 3) the incorporation of organic moieties directly and specifically into the pore-walls by using a bis- or poly(trialkoxysiliyl) precursor R—$[Si(OR')_3]_n$ (silsesquioxane, $n \geq 2$).[35]
The third approach is the basis for the new materials class of periodic mesoporous organosilicas - PMOs - discovered in 1999.[37–39] The periodic order of the PMO materials can be achieved by applying the above-mentioned (see section 1.1.2) EISA approach with soft-templates.
The advantage of PMO materials over otherwise synthesized organosilica is that

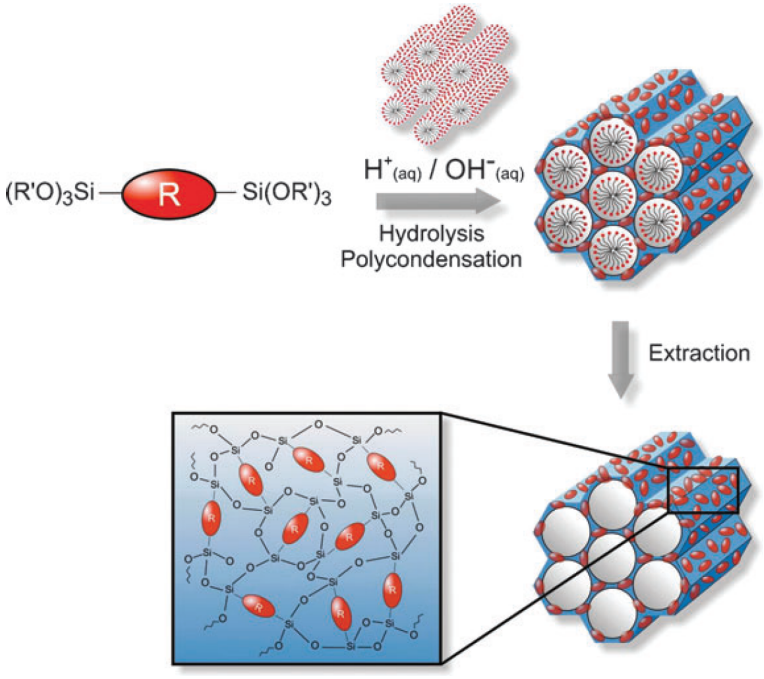

Figure 1.7: Schematic synthetic pathway to PMOs that are constructed from bis-silylated organic bridging units R. R′ denotes an alkyl group, in most cases a methyl or ethyl group.[36]

the organic units are uniformly distributed within the entire porous network (see figure 1.7). There is no limitation of the organic content based on the surface area of the pores as observed for the *grafting* method. PMOs are attractive candidates for applications in various fields such as catalysis and adsorption.[40] The first PMOs were synthesized with small organic bridges such as ethylene having limited functionality. However, the establishment of relatively simple synthesis routes for various silsesquioxane precursor molecules is mirrored in the plethora of PMO materials already a short time after the introduction of this new field.[41]

Surprisingly, some PMO materials show not only a periodicity at the mesoscale but also exhibit a crystal-like arrangement of the organic moieties within the framework. This behavior was first shown for phenylene-bridged PMO materials in 2002 from the group of Inagaki.[42,43] The formation of crystal-like pore walls is favored for precursor molecules that are rather rigid, linear/symmetric and do not carry

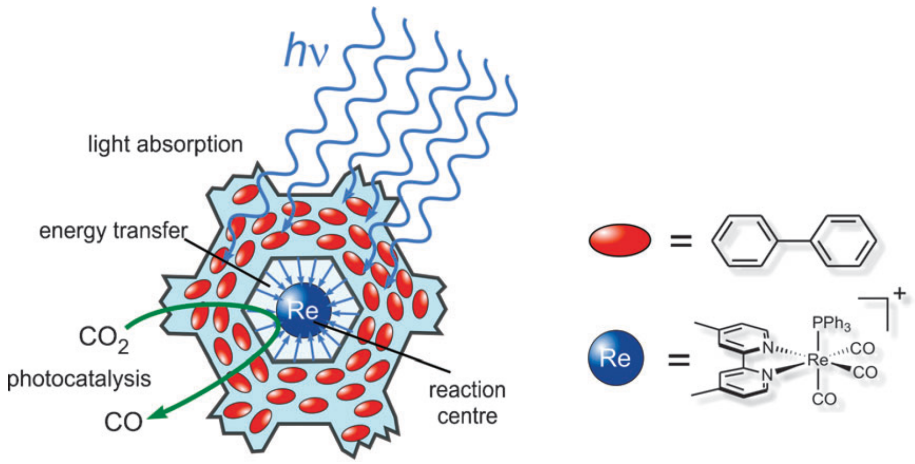

Figure 1.8: Schematic representation of the application of a PMO as light-harvesting antenna. The energy of the incident light is funneled and transferred to the incorporated Re-complex. This way the catalytic activity of the Re-complex is enhanced.[36]

bulky substituents.[36] The molecular arrangement is often reflected by the optical properties of the material. This unique feature opens up the possibility to control the optical and electronic properties by tuning the interactions between the organic bridges.[34]

One impressive example for the potential of this crystal-like arrangement is depicted in figure 1.8. The biphenylene bridges in the walls acts as a light-harvesting antenna. The photocatalytic reduction of CO_2 is sensitized through resonance energy transfer towards an incorporated Re-complex. The antenna effect of the PMO leads to an enhanced photocatalysis, and through the incorporation in the porous matrix the Re-complex is additionally protected from degradation.[44]

In the last few years precursor molecules with large organic bridges having dimensions of several nanometers such as phorphyrin[45], three-armed phenylenevinylene[46] or dithienyl-benzothiadiazole[47] have been successfully applied to build periodically ordered networks. The incorporation of large conjugated systems as organic moieties in PMOs is aimed at obtaining light-sensitive materials with special properties such as conductivity. New applications in optoelectronic fields such as light-emitting diodes, photovoltaic devices or artificial photosynthesis are expected from

π-conjugated silsesquioxane precursors.

A major challenge will be if it is possible to implement a large-scale commercial application of PMOs. One crucial point to become competitive with other 'traditional' materials will be the development of low-cost synthesis routes for the silsesquioxane precursors.[36]

One goal of this thesis was to develop synthetic sol-gel routes for new electronically active PMO materials. Two different approaches for the silsesquioxane building blocks were applied and are focus of the chapters 4 and 5. The introduction of new properties and the subsequent characterization in applications such as photovoltaic devices was investigated. In addition, chapter 6 deals with the introduction of fullerenol precursor molecules into a stable nanostructured silica matrix. This was also done via a sol-gel synthetic route.

1.2 Polymer-Oxide Hybrid Materials

One perfect example of the synergistic effects that can be gained in polymer-oxide hybrid materials is set by nature with the nanocomposite nacre (also called 'mother of pearl'): it is composed of layers of hexagonal platelets of $CaCO_3$ that are vertically stacked and separated by an organic biopolymer (see figure 1.9). This evolutionary design leads to the extraordinary strength and resilience of the 'mother of pearl'.[48]

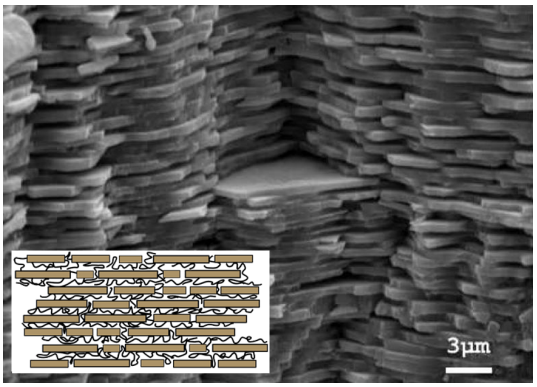

Figure 1.9: Scanning electron microscope image of a cross section of nacre.[49] The inset shows a schematic view of the nanoscale structure (scheme from Kebes, distributed under CC BY-SA-3.0 license).

This role model of a synergistic nanocomposite illustrates the potential of polymer-oxide hybrid materials.

The focus of this introductory section will be on polymer-silica and polymer-metal oxide hybrid materials, with special attention to conjugated polymers.

The simplest method to synthesize a polymer-oxide composite is the direct mixing of both components by melt blending or solution blending. However, inorganic nanoparticles have a strong tendency to agglomerate, which often prevents the formation of a uniform blend at the nanoscale.[50] Due to this, it is often not possible to produce thin homogeneous films from these blends. A better control over the morphology of at least one phase can be achieved by using pre-formed mesoporous

inorganic materials as a host for the polymer. For pre-formed mesoporous films of inorganic oxides, the infiltration of a polymer by melting or simple soaking of a polymer solution is quite successful.[51] Several studies show that the encapsulation of a photo-active polymer, e.g. poly[2-methoxy-5-(2'-ethyl-hexyloxy)-1,4-phenylene vinylene] (MEH-PPV) into mesoporous silica led to an enhancement of the photo-stability, color purity and photoluminescence of the polymer. The orientation and the isolation of the polymer chains seem to be essential for this behavior.[52,53] The infiltration of conjugated polymer into a mesoporous semiconductor network is also one of the major synthesis routes for efficient hybrid photovoltaic devices.[9] Thereby the morphology of the polymer-oxide interface is essential for efficient charge-transfer and for the performance of the device.[54]

Enhanced miscibility of the polymer and oxide components on the molecular-,nano- or micro-scale can be achieved by a different, widely adopted synthesis method: the in-situ generation of one or both phases. Numerous studies have been published in the field of preparing composite materials from macromolecular polymers introduced into the sol-gel synthesis process.[8] However, the uncontrolled morphology and often only weak interactions between the two phases are common issues with this approach.[55]

An alternative route is the in-situ polymerization of the polymer inside a pre-formed inorganic network.[56,57] This way, the nanoscale morphology of the network is already predetermined through an appropriate sol-gel process: for example in ref.[58] Möller et al. reported in 1998 on the synthesis of poly(methyl methacrylate) (PMMA) mesoporous silica composites obtained by adsorption of MMA into the pores of mesoporous silica, followed by intra-pore polymerization. The polymerization was initiated with benzoyl peroxide. The polymer confined in the 30–35 Ådiameter channels of the hosts did not show characteristic bulk behavior with respect to the

glass transition temperature.[58] Similar to the earlier mentioned enhanced photoluminescence of infiltrated MEH-PPV chains, Alvaro et al. observed an enhanced luminescene for in-situ polymerized poly(phenylene vinylene) oligomers in zeolites.[56] Nearly all of the previously described methods yield hybrid materials with only weak and non-covalent interactions between the polymer and the inorganic metal oxide. On the other hand, grafting methods are a feasible alternative to design polymer-metal oxide composites with covalent interactions between the phases.

The '*grafting-to*' approach refers to the attachment of end-functionalized preformed polymer chains to a substrate. However, this method often yields low grafting densities due to steric repulsion between already grafted and incoming polymer chains.[59] Moreover, this method is not suitable to fill porous substrates with narrow pores such as mesoporous metal oxides: the functionalized macromolecules have only limited access to the pores due to their size, conformational entropy and stiffness and could also block the pores quite early in the grafting procedure.

The alternative method of growing the polymer directly from the functionalized surface of the substrate (*grafting-from*) is probably better suited for hybrid materials based on mesoporous inorganic networks.[50] This in-situ method introduces versatility, and some degree of control to the formation of covalently linked polymer chains and can be implemented with almost all available polymerization routes.[59] With photocatalytically active mesoporous frameworks such as titania it is even possible to initiate a photopolymerization directly from the surface without any previously attached initiator by UV light irradiation.[60,61]

Although many subjects of the surface-initiated polymerization and its mechanism such as the influence of the confined space[62,63] or diffusion limitations[64] have been investigated lately, there are still many open questions in this field. For example, the influence of the nature of the covalent coupling of a conducting polymer on the

charge-transfer behavior of the resulting interface, or the polymer packing in the confined space are rarely addressed.

Therefore one topic of this thesis, discussed in chapter 3, was to develop a new synthesis method to infiltrate the photoactive polymer MEH-PPV into a pre-formed titania scaffold. Surface functionalization of the titania was applied to guide the growing polymer chains towards the TiO_2 network and this way achieve a higher infiltration. The influence of the nature of the interfacial connection between the MEH-PPV and TiO_2 on the charge-transfer was characterized by photovoltaic performance measurements.

Chapter 2

Characterization Techniques

2.1 X-Ray Diffraction

X-ray diffraction (XRD) is a powerful technique to analyze on the one hand the nature of crystalline materials and on the other hand to gain structural information of macromolecules or periodically ordered nanostructures.[65]

One common technique to produce X-rays is to bombard a target with high-energy electrons. Due to interactions with the target the electrons are slowed down and a part of their energy is radiated as a continuous background spectrum called 'Bremsstrahlung'. Depending on the elemental composition of the target, the emitted spectrum also exhibits characteristic narrow lines resulting from X-ray fluorescence. Fairly monochromatic X-rays can be isolated from the single energy spikes by applying blocking filters. The wavelength of the resulting photons is in the Ångstrom range, which is at the same order of magnitude as the distance of atoms in solid matter. Mostly Cu-K_α and Mo-K_α radiations with a wavelength of about 1.54 and 0.71 Å are used.

XRD characterization is based on the elastic X-ray scattering by atoms in a periodic three-dimensional array (see figure 2.1).

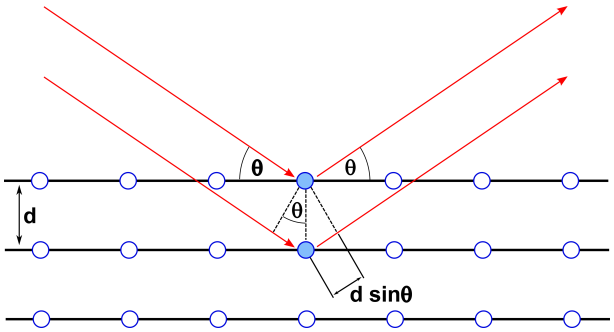

Figure 2.1: Schematic diagram of X-ray diffraction at a crystal lattice plane illustrating the Bragg relation. Constructive interference occurs when the path-length difference is an integer multiple of the incident wavelength.

The atoms act like a three-dimensional diffraction grating. Coherent scattering occurs only when the phase difference between the scattered waves is a multiple of 2π. This condition is geometrically met when the path length difference of the scattered waves is an integral number of the wavelength λ (see eq. **2.1**) and known as the Bragg equation.[66]

$$n \cdot \lambda = 2 \cdot d_{hkl} \cdot sin(\frac{\theta_i + \theta_d}{2}) \tag{2.1}$$

θ_i and θ_d denote the incident and diffracted beam angle, d_{hkl} corresponds to the lattice plane spacing.

XRD measurements can be divided into two groups according to the measured angle range. Measurements below 10° 2θ are typically called small-angle X-ray scattering — SAXS —, those with higher 2θ values wide-angle X-ray scattering — WAXS.

WAXS spectra are commonly used to determine the crystal unit cell and the mean crystalline domain size. The broadening of the coherent diffraction signals of the crystalline phase is used to determine the crystallite size via the Debye-Scherrer Equation (see equation 2.2). The reason for the reflex broadening is an incomplete destructive interference of the out-of-phase X-rays. In the Debye-Scherrer equation (equation 2.2), k is an instrument dependent proportionality factor, usually about 0.94 for spherical particles, λ the X-ray wavelength, B the full width at half max-

imum and θ the Bragg angle. D is the mean crystalline domain size - the average dimension of material volume producing coherent diffraction. It should be noted that the results for the crystalline domain size are volume-based and therefore small amounts of larger particles will lead to an overestimation of the average crystallite size.[67,68]

$$D = \frac{k\,\lambda}{B\,cos\theta} \tag{2.2}$$

Contrary to this, SAXS measurements can provide information on the shape and size of macromolecules, characteristic distances of partially ordered materials and wall-to-wall distances in porous systems. In a usual θ-θ setup only information of the structure in one dimension, resulting from lattice planes parallel to the substrate, can be obtained.

More detailed information can be collected by 2D grazing-incidence SAXS (GISAXS). This specialized method provides two-dimensional SAXS diffraction patterns originating also from lattice planes that are not parallel to the substrate. The resulting signals are called out-of-plane reflections. In some cases it is possible to index the reflections of highly periodic and oriented mesoporous materials and to assign a corresponding space group.[69] 2D-SAXS data can be collected in transmission or reflection mode. In transmission mode the sample must be thin enough to allow transmission. The GISAXS setup in reflection mode is more suitable for films on substrates (see fig. **2.2**).

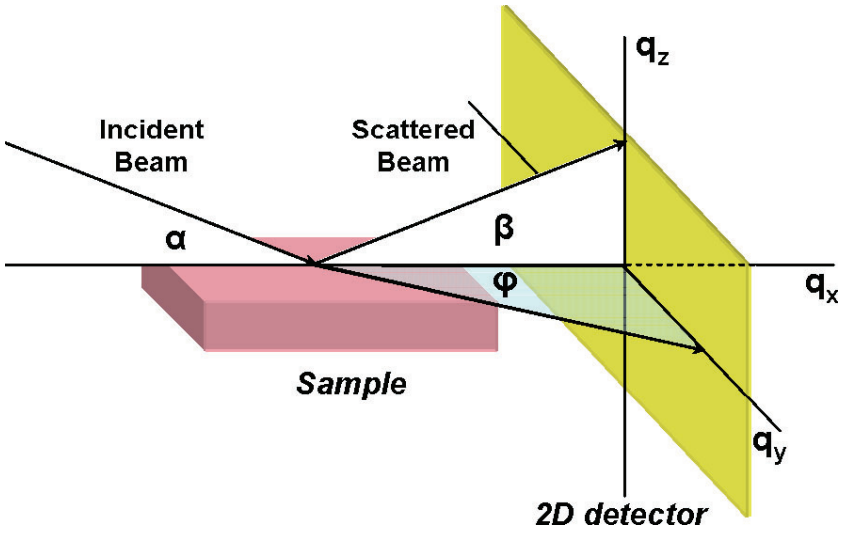

Figure 2.2: 2D grazing-incidence small angle X-ray scattering: In-plane and out-of-plane reflections shown for a thin-film XRD measurement configuration in reflection mode.[28]

2.2 Electron Microscopy

Electron microscopy is an essential technique for the characterization of the structure and composition of materials on the nanoscale. Similar to XRD, it is in principle a scattering technique, but instead of photons with wavelengths of several 100 nm in optical microscopy or a few Ångstrom in XRD, it uses electrons with a wavelength in the range of picometers. Therefore, the possible resolution according to Abbe's equation is increased dramatically. The smallest resolvable distance between two objects Δd depends on the wavelength λ, refractive index of the sample n and half of the opening angle α of the focusing beam (see eq. **2.3**).[70]

$$\Delta d = \frac{\lambda}{2nsin\alpha} \tag{2.3}$$

In most cases, an electron beam is generated either by thermal emission (using a tungsten filament or a LaB_6-crystal) or by thermally assisted field emission (Schottky field emitter). The wavelength of the emitted electrons depends on the acceleration voltage. The electron beam is focused on the examined specimen by a series of electrostatic and magnetic lenses. The interaction of the electrons with matter is much stronger compared to light or X-rays and the various signals emanating from a sample upon irradiation with a beam of high energy, primary electrons, can be classified as shown in figure 2.3.[71]

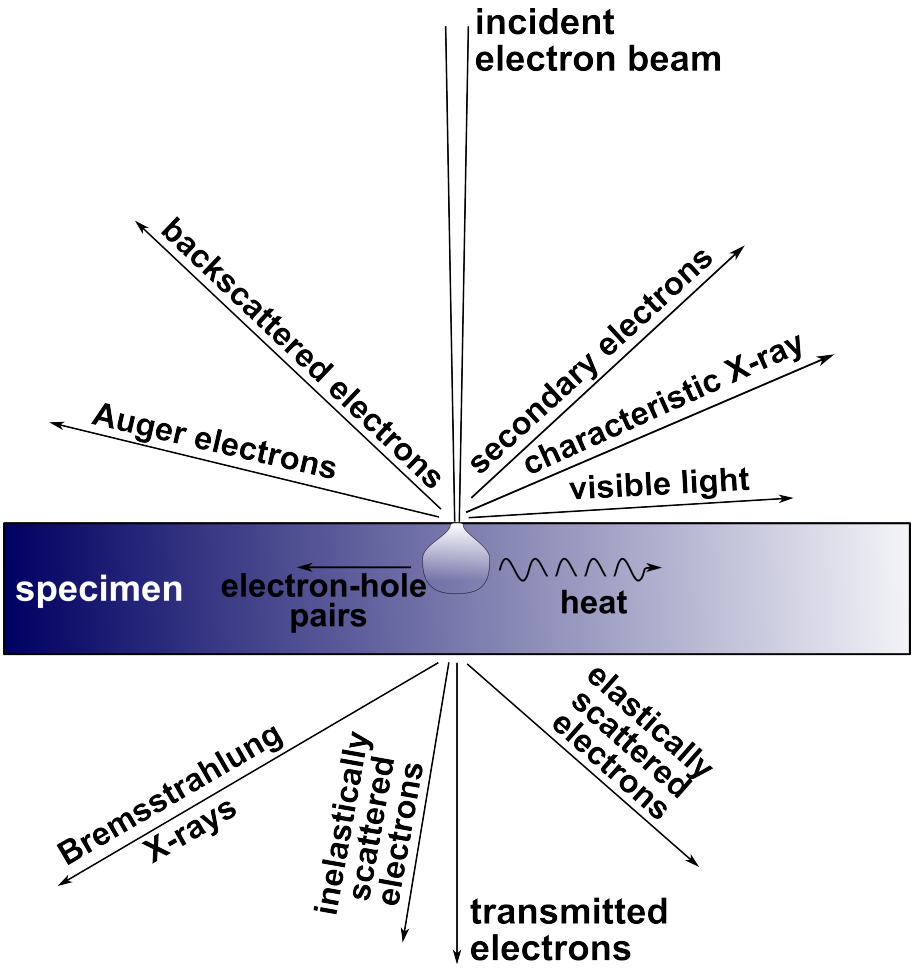

Figure 2.3: Scheme of electron beam interactions with the sample. Depending on the sample thickness and atomic structure different interaction types dominate.

Transmission Electron Microscopy

In transmission electron microscopy (TEM) only electrons transmitted through an ultra-thin specimen (below ca. 100 nm) are detected. Behind the specimen the modulated electron beam is focused and magnified through several lenses and projected on a fluorescent screen or a CCD camera. This projection results in limited depth resolution and superimposition of structural data on the image plane in TEM studies. Due to the high acceleration voltages of around 100–300 keV, micrographs with a high lateral spatial resolution can be achieved. Heavy atomic nuclei scatter electrons more effectively and to higher angles of deflection than those of light atoms.

Therefore heavy elements exhibit a higher contrast in TEM imaging. Together with the structural information in real space obtained from scattering contrast, electron diffraction patterns can be recorded from the transmitted scattered electrons.

Scanning Electron Microscopy

In contrast to TEM, scanning electron microscopy (SEM) detects only electrons and radiation that are reflected off the specimen surface after interaction with the electron beam. Therefore the electron beam is scanning over the surface of the specimen in a raster scan pattern to record the final images. Depending on the applied acceleration voltage, the interaction volume and the amount of secondary and backscattered electrons can be varied. However, these factors are also dependent upon the sample morphology and composition and will increase with a decreasing glancing angle of incidence as more scattering occurs close to the surface. This change in the number of detected electrons and thus signal intensity depending on the surface curvature of the sample is responsible for the high topological contrast in SEM.
In addition, collisions of primary electrons with core electrons from atoms in the sample result in excited atomic states. Upon decaying to their ground state, the atoms in the sample emit X-ray photons with characteristic wavelength distributions for different elements. In this way, SEM allows one to obtain topographical information as well as elemental composition and spatial distribution of near surface regions of the investigated sample.

2.3 Atomic Force Microscopy

Atomic force microscopy (AFM) was invented in 1986 by Gerd Binnig, Calvin Quate and Christoph Gerber by combining the principles of the scanning tunneling microscope and the stylus profilometer.[72] Unlike electron microscopy, AFM is an imaging technique to investigate surfaces of insulators of an atomic scale. The sample does not suffer from beam damage, no ultra-high vacuum conditions are needed and the obtained topographic information resembles more accurately the actual three-dimensional surface topology rather than just giving a two-dimensional projection. However, image acquisition takes usually several minutes and imaging artefacts can make data interpretation more challenging.

For AFM imaging a sharp nanoscopic tip attached to the end of a cantilever is scanned line by line in a defined pattern over the surface of the sample. Due to the surface topology and forces - mainly Coulomb and Van-der-Waals forces - between the tip and the surface atoms the cantilever is deflected. This deflection is monitored by a laser that is reflected off the backside of the cantilever onto a photodiode detector (see figure 2.4). The spatial resolution depends mainly on the dimensions of the radius of curvature of the tip, which is normally in the range between 10 and 20 nm. In an ideal case this can be sufficient to resolve single atoms.

Depending on the type of interactions that are used for the measurement, different measurement modes can be distinguished. In the so-called contact mode, the tip of the cantilever is in close contact with the sample all the time during the scanning. The second method, the non-contact mode is opposed to the first: the tip does not touch the surface of the sample at any given time. Thereby the cantilever is excited near its resonance frequency. Interactions with the surface change the resonance frequency, which changes the amplitude and phase of the oscillation. This method

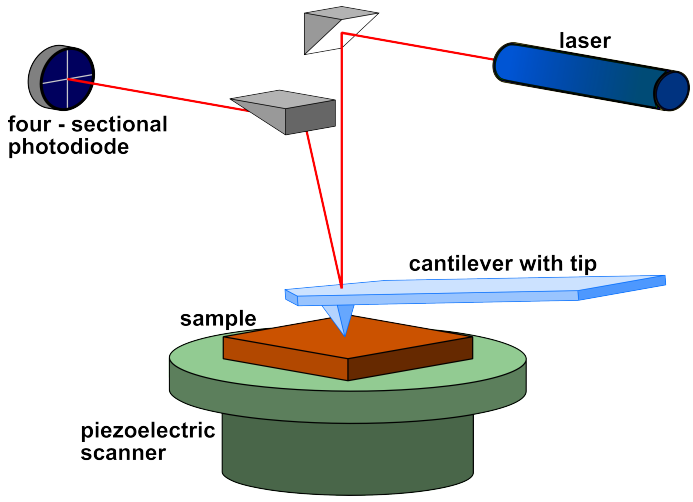

Figure 2.4: Schematic working principle of an atomic force microscope.

is especially suitable for mechanically delicate samples or for measuring the change of the interaction forces between tip and surface due to different material phases. The third method is the intermittent or tapping mode.[73] It is an intermediate between the two extremes contact and non-contact mode. The distance to the surface is much closer and the tip is touching the surface during the oscillation.

Next to the three categories of interactions described above, there are two other methods that relate to the way the movement of the tip is operated. On the one hand there is the constant-height method. Thereby the tip is moved at a fixed height above the scanned area. It is the simplest measurement approach because it is least demanding on the control and feedback systems. This method is only suitable for very smooth samples, because the rougher the surface, the higher the forces working on the cantilever. To avoid destroying the cantilever and tip by crashing into high features of the sample surface, another method - the constant force method - was developed. The distance between tip and sample surface is regulated at a constant value by feeding the position of the laser on the photodiode into a feedback loop and adjusting the height such that the deflection of the cantilever is constant.

2.4 UV-Vis Spectroscopy

One method to quantitatively and qualitatively characterize compounds, that absorb light in the range of ultra violet to near infrared light is called UV-Vis spectroscopy. The relation between absorbance and concentration of the absorbing species is given by the Beer-Lambert law:

$$A(\lambda) = -\log \frac{I}{I_0} = \epsilon(\lambda)\, c\, L \tag{2.4}$$

In equation 2.4, $A(\lambda)$ denotes the measured absorbance, I the light intensity after passing through the sample compartment, I_0 the intensity of the incident light, $\epsilon(\lambda)$ the extinction coefficient, c the concentration of the absorbing species and L the length of the pathway through the sample.[74,75]

By absorbing light of a defined wavelength, electrons from the highest occupied molecular orbital (HOMO) will be excited into the lowest unoccupied molecular orbital (LUMO). Therefore, the energy level distance of molecules or the band gap in semiconducting materials can be evaluated through UV-Vis spectra. It has to be taken into account that vibrational energy levels lie in between the different electronic energy levels. UV-visible light can excite these molecular vibrational levels as well and as a result, often there is not one sharp peak observed in the spectra, but rather a set of overlapping vibronic modes. While for small molecules the absorption maximum is usually determined as the HOMO-LUMO gap, the Tauc relation (equation 2.5) is used for estimating the band gap of semiconductors. According to the Tauc equation 2.5 the absorption coefficient α multiplied with the photon energy $h\nu$ is related to the band gap energy E_g. C is a constant and the value of n specifies the type of transition. For direct transitions n has the value of $\frac{1}{2}$, for

indirect transitions n equals 2.[76]

$$\alpha h\nu = C(h\nu - E_g)^n \tag{2.5}$$

The optical band gap is estimated from the so called Tauc plot by plotting $(\alpha h\nu)^2$ against $h\nu$ for direct transitions, for example. The intersection with the abscissa obtained from extrapolating the linear regime of the resulting plot, yields the E_g value of the examined material (see figure 2.5).[77]

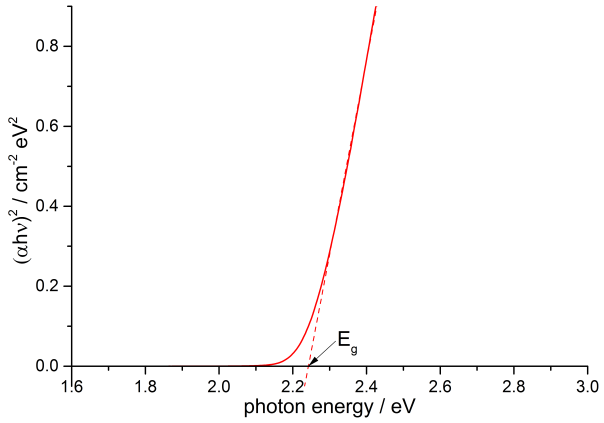

Figure 2.5: Example of a Tauc Plot of a direct transition. The intersection with the abscissa of the linear fit gives the value of the optical band gap energy E_g.

A common setup of a UV-Vis spectrometer consists of a light source (e.g. a deuterium arc lamp or a tungsten filament), a prism or a monochromator to separate the different wavelengths, a sample holder and a detector, which is often a photodiode or a charge-coupled device (CCD).

2.5 Nuclear Magnetic Resonance

Nuclear magnetic resonance spectroscopy (NMR) is a powerful technique to study the electronic environment of magnetic isotopes and their interactions with neighboring atoms. This way, detailed information on the topology, dynamics and three-dimensional structure of molecules in solution and in the solid state can be obtained. An essential requirement for NMR measurements is that the nucleus of interest has a spin momentum. Nuclei with an odd number of protons, neutrons or both exhibit a spin momentum, which is proportional to a magnetic momentum $\vec{\mu}$ (eq. **2.6**). In equation 2.6 $\vec{\mu}$ corresponds to the nuclear magnetic momentum, γ to the gyromagnetic ratio and $\vec{S}$ to the spin angular momentum.[78]

$$\vec{\mu} = \gamma \vec{S} \tag{2.6}$$

A few examples of isotopes suitable for NMR studies are ^{1}H, ^{13}C, ^{15}N, ^{19}F, ^{29}Si and ^{31}P.[78]

In the presence of an external magnetic field the possible orientations of the nuclear magnetic momentum are limited to discrete quantum states (*Zeeman* effect). The number of possible states is $2I+1$ with I as the spin quantum number. The transition between these states occurs by absorption of electromagnetic radiation in the radio frequency range, which meets the resonance condition of equation **2.7**.[79]

$$\omega = \gamma B_{loc} = \gamma(B_0 + B_{int}) \tag{2.7}$$

Here, ω denotes the resonance frequency, B_{loc} the local magnetic field, B_0 the external magnetic field and B_{int} the internal magnetic field.[80]

The measured difference of the local magnetic field and the applied external field gives insights into the electronic and chemical environment of the relevant atoms.

In the solid state the dipole-dipole interactions between neighboring nuclei give rise to line broadening and this can make the interpretation of the spectra more difficult. This anisotropy effect is eliminated by rotating the sample at the *magic angle* of 54.7° with respect to the applied field. For that reason this special method for solid samples is called magic angle spinning NMR spectroscopy (MAS-NMR).[79] The above mentioned line broadening effect does not occur in liquids because the Brownian motion of the molecules averages the anisotropic effects.

2.6 Physisorption of Nitrogen

Sorption analysis is a non-destructive widespread technique to characterize porous materials. By recording the adsorption and desorption isotherms of appropriate probe molecules such as nitrogen, fundamental properties including the surface area, pore size distribution and pore volume can be obtained. The process of adsorption, i.e. the accumulation of one or more components in an interfacial layer occurs when a solid material is exposed to a gas or vapor. In this case, the solid is considered as *adsorbent*, the adsorbed gas molecules as *adsorbate* and the gas in equilibrium with the adsorbate as *adsorptive*.

The following discussion will center on physisorption, i.e. the process in which the adsorbate is bound to the surface via weak van-der-Waals forces such as dipole-dipole or London forces or via hydrogen bonding. In contrast, the adsorption in chemisorption processes involves a chemical reaction between the adsorbate and the surface and therefore results in a strong interaction.

The two main methods for the determination of adsorption isotherms are the volumetric and the gravimetric method. In both cases, the adsorbent is kept at a constant temperature, usually at or near the boiling point of the adsorptive, for example by cooling in liquid nitrogen in the case of nitrogen sorption. The adsorptive pressure is increased step-wise and followed by equilibration of the system. The increase in adsorbed molecules is measured with the gravimetric method by detecting the mass gain after each step. On the other hand, for the volumetric method the adsorbed gas volumes are usually calculated by comparison of the actual pressure change with the expected pressure change in absence of the absorbent. The amount of adsorbate is plotted against the relative pressure of the absorptive (normalized to the vapor pressure at that temperature) in a sorption isotherm diagram. After

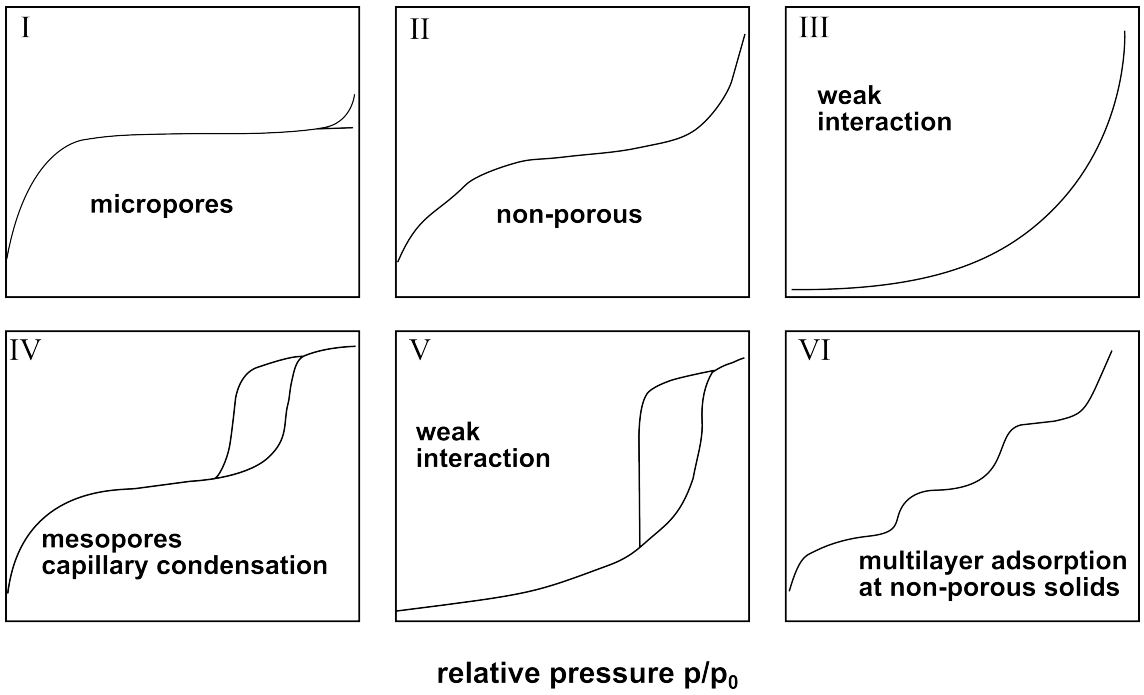

Figure 2.6: IUPAC classification of six different isotherm types.

increasing the partial pressure of the absorptive close to the saturation pressure, the corresponding desorption isotherm is recorded by decreasing the partial pressure of the adsorptive step-wise back to zero. The resulting isotherms can be classified as one of six types corresponding to IUPAC nomenclature[81,82]. Materials with different porosity show characteristic isotherm shapes and hystereses, which are shown in figure 2.6. The development of sorption analysis is based on the work of I. Langmuir in 1916[83], who created a kinetic model of the adsorption processes on surfaces. The sorption analysis is one of the standard methods of instrumental surface analysis. Various refinements based on this method have been developed, among which the Brunauer-Emmett-Teller (BET) theory for determining the specific surface area, the Barret-Joyner-Halenda method (BJH) and density functional theory (DFT) for the pore size distribution (PSD) are the most commonly used.

The macroscopic BET theory is based on several assumptions:

- the gas molecules physically adsorb on a solid in multilayers with an infinite

number of layers,

- there is no interaction between the particles in each adsorption layer and
- the Langmuir theory can be applied for each layer, i.e. the adsorption enthalpy is the same except for the first layer where the enthalpy is only based on interactions between adsorbent and adsorptive.

Based on these assumptions, the BET equation was derived (see equation 2.8 for its linear form).

$$\frac{p}{n^a \cdot (p^0 - p)} = \frac{1}{n_m^a \cdot C} + \frac{(C-1)}{n_m^a \cdot C} \frac{p}{p^0} \tag{2.8}$$

The variable n^a refers to the adsorbed amount at relative pressure $\frac{p}{p^0}$. The monolayer capacity is represented by n_m^a and C is the BET constant, which is related to the adsorption enthalpy of the first monolayer. In the range between 0.05 and 0.35 $\frac{p}{p^0}$ the term $\frac{p}{n^a \cdot (p^0 - p)}$ is linear proportional to the relative pressure $\frac{p}{p^0}$. From the linear fit of the isotherm in this region the monolayer capacity n_m^a and the BET constant C can be calculated, and subsequently with these values the specific surface area can be estimated.

The classical method for estimating the pore size distribution is the BJH method, which is based on the Kelvin equation:

$$\frac{1}{r_1} + \frac{1}{r_2} = -\frac{RT}{\sigma^{lg} \nu^l} \ln \frac{p}{p^0} \tag{2.9}$$

It relates the principal radii, r_1 and r_2, of the curvature of the liquid meniscus in the pore to the relative pressure $\frac{p}{p_0}$ at which condensation occurs. The surface tension of the liquid condensate and its molar volume are denoted by σ^{lg} and ν^l, respectively.[84,85]

In the Kelvin equation a change in vapor pressure due to a curved liquid-vapor interface (meniscus) with radius r is described and can be applied to the capillary

condensation in mesopores. Experience shows that the results obtained with the BJH method deviate from pore sizes estimated by different methods such as TEM for example. This is especially the case for micropores and small mesopores, where the BJH method underestimates the pore size.

A more recent approach that often yields more reliable results is the DFT theory. This microscopic method describes the local field structure near curved walls more accurately. For a correct estimation, specific knowledge of the pore shape, pore connections and surface atoms is required to calculate the appropriate interaction forces and choose the matching input parameters. In the past few years several new calculation kernels (e.g., for carbon materials) for different surface compositions and pore structures were developed and this way the accuracy of the estimated pore size distributions could be improved.[86,87]

2.7 IR and Raman Spectroscopy

The chemical bonding in materials can be studied through absorption of infrared light via the excitation of vibrational and rotational modes. Two major techniques are used for vibrational spectroscopy. On the one hand infrared(IR)-spectroscopy, which is based on the direct absorption of infrared light. On the other hand, Raman spectroscopy relies on the inelastic scattering of monochromatic light by interaction with the electron clouds in the molecules.

IR spectra are obtained by measuring the intensity of a beam of electromagnetic radiation, usually in a range between 400–4000 cm^{-1}, directly after interaction with the sample. This mid-IR radiation is capable of inducing transitions between molecular vibrational energy levels, thus providing information about the nature of the chemical bonds in the sample. A general selection rule for photon absorption in IR spectroscopy is the required change of the dipole moment of the molecule during the vibration. The molecule itself, however, does not need to have a permanent dipole.[78]

As both IR and Raman spectroscopy use different physical processes to investigate the vibrational modes of a sample, they also display different selection rules for the observable vibrational states and are thus complementary characterization techniques. The general selection rule for Raman scattering is that a change in bond polarizability during the vibration has to occur, i.e. the signal intensity is determined by the amount of deformation of the electron cloud. The more complex relationship between the energy levels of the vibrations and the Raman scattering is depicted in figure 2.7. Most of the incident light is subject to elastic scattering and released with the same energy. This process is called Rayleigh scattering. Much weaker signals created by Stokes scattering are shifted towards lower wavenumbers compared to

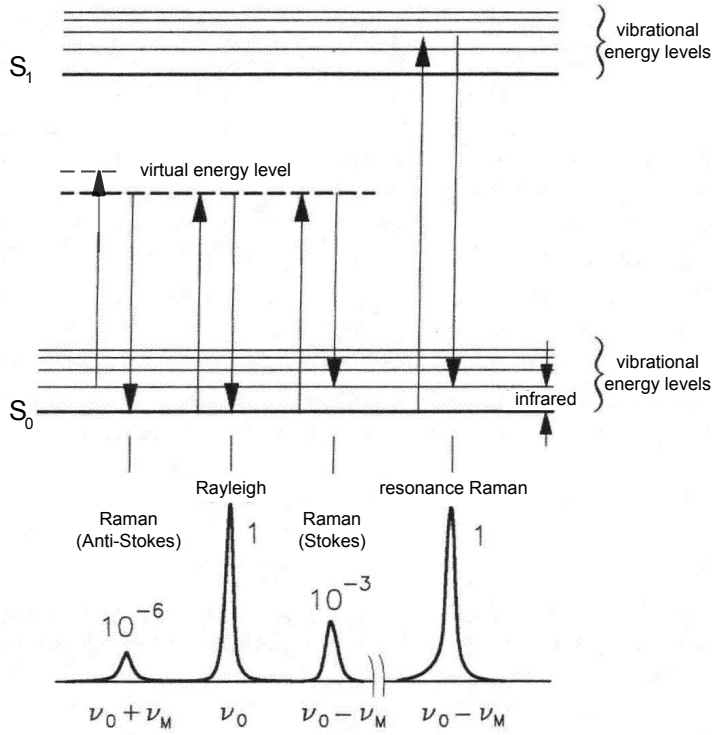

Figure 2.7: Energy diagram with virtual energy state to point out the particular processes during Raman scattering.[88]

the incident beam. The corresponding anti-Stokes lines exhibit wavenumbers higher than the excitation energy. Similar to IR spectroscopy, both Stokes and anti-Stokes shifts can be used to determine vibrational information, which is specific to the chemical bonds and symmetry of molecules. This way, both Raman and IR spectra can be used to identify molecules or functional groups.

2.8 Thermogravimetric Analysis and Differential Scanning Calorimetry

Thermal analysis is a general term for a multitude of analytical methods to determine the physical or chemical properties of a sample in dependence of the temperature. In materials sciences this method is commonly used to characterize material like alloys, ceramics, polymers, glasses or composites.[89]

Two of the most important techniques are the thermogravimetric analysis (TGA) and differential scanning calorimetry (DSC).

In TGA measurements the sample is subjected to a controlled heating or cooling rate, respectively. Commonly the measurements are performed under a defined gas atmosphere with a constant gas flux, or under vacuum. The exact temperature determination is ensured by a calibration with a reference material. The resulting thermogram, obtained by plotting the weight change of the sample against the temperature, gives information about desorption of adsorbed molecules, evaporation of volatile compounds and thermal decomposition reactions.

The complementary method of differential scanning calorimetry (DSC) can be measured simultaneously with the TGA. DSC is based on the quantitative determination of the energy needed to heat the sample compared to a reference at the corresponding temperature. This way endo- and exothermic enthalpies for various processes, e.g. desorption of adsorbed molecule, combustion processes and phase transitions can be obtained.

2.9 Size Exclusion Chromatography

The principle of size exclusion chromatography (SEC) was presented for the first time by G.H. Lathe and C.R. Ruthven in the middle of the 1950s.[90,91] They used swollen starch matrices to separate various sugars according their different molecular weight. A few years later columns with cross-linked dextran were introduced as a more reliable synthetic gel.[92] However, not until J.C. Moore established a way to synthesize cross-linked polystyrene columns with controllable pore sizes, SEC developed into a versatile and important separation and 'cleaning' method for polymers and large biomolecules such as proteins.[93]

Contrary to other chromatographic methods, the working principle is not based on adsorption of the molecules on the surface of the column medium - the stationary phase, but depends on the porous structure of the same and the size of the molecules. All chromatographic methods have in common that the relevant component mixture is dissolved in a mobile phase, here an organic solvent, and transported by this phase through a column filled with the stationary phase. In SEC the molecules, in relation to their molecular size, are retarded on their way through the stationary phase as depicted in figure 2.8. The stationary phase is built of porous particles that exhibit different pore sizes. A large macromolecule cannot enter these pores and will travel through the column in the direction of the flow of the mobile phase quite quickly and elute first. Smaller molecules can access the pores and channels of the material and have therefore a longer retention time in the stationary phase.

The eluent flow can be analyzed continuously by spectroscopic techniques such as refractometry and UV spectroscopy. Additional methods include multi-angle laser scattering (MALS) and viscosity measurements.

In the beginning, the size of an unknown molecule, for example a polymer, could

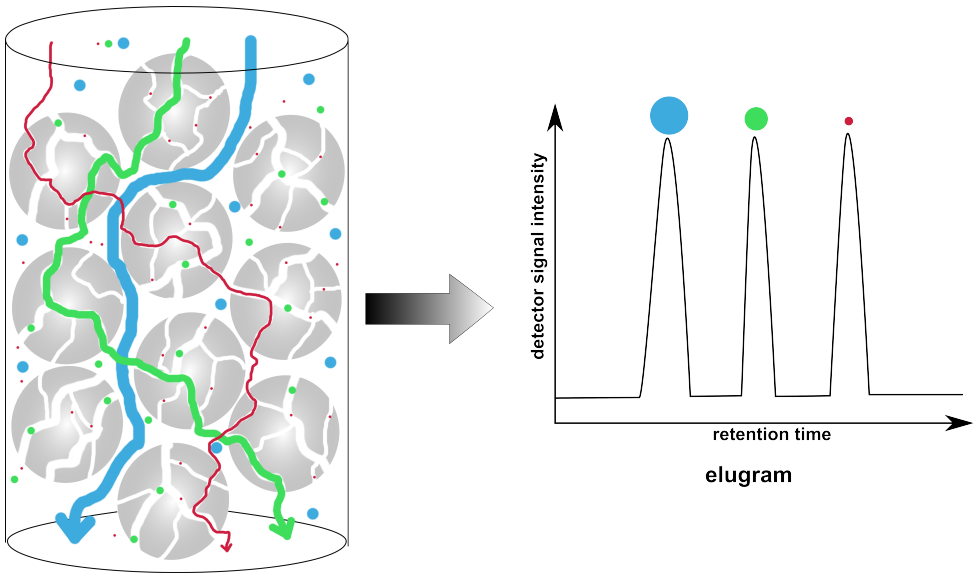

Figure 2.8: Schematic picture of the separation principle of size exclusion chromatography. The retention time on the stationary phase depends strongly on the molecular size.

only be determined via calibration with standards of a polymer of known molecular weight and similar in chemical nature and morphological structure. The obtained molecular weight of the sample was therefore only an estimate and sometimes strongly deviated for branched molecules or polymers without access to well-defined calibration standards. Moreover, for every single polymer a suitable calibration procedure had to be applied.

The discovery of the hydrodynamic volume as the crucial parameter for the retention time partially resolved this issue. With this knowledge an universal calibration could be applied that is suitable for many different polymers.[94]

The molecular weight obtained in this weight was nevertheless still only an estimate. An absolute determination of the molecular weight is possible with light-scattering detectors. Therefore the angle-dependent light scattering of the macromolecules is used to calculate the molecular size. For this analysis method additional information such as the differential refractive index and the precise concentration are crucial for a reliable result.[95]

2.10 Photovoltaic Characterization

The main concept of a photovoltaic device is to generate electricity from light. Upon illumination, photons are absorbed by an active layer - often a semiconducting polymer for hybrid solar cells - and electron-hole pairs, also called excitons, are generated. Contrary to inorganic semiconductors such as silicon, conjugated polymers exhibit relatively low dielectric constants and therefore the Coulomb interactions between electrons and holes are strong, with binding energies typically ranging from ∼0.1–0.4 eV.[96] Therefore exciton dissociation into free mobile charges can only take place at a donor-acceptor (D-A) interface, to which the excitons need to diffuse beforehand. The resulting electrons and holes have to travel to the electrodes through their corresponding percolating pathways.[97] The device performance is influenced by six main consecutive factors affecting these processes (c.f. figure 2.9):

1. photon absorption (η_A)
2. exciton generation (η_{ex})
3. exciton diffusion (η_{diff})
4. exciton dissociation (η_{ed})
5. charge transport (η_{ctr})
6. charge collection (η_{cc}).

The efficiencies η of the single processes combined, result in the external quantum efficiency of the device (EQE). The EQE is also defined by the ratio of the number of charge carriers collected at the electrodes to the number of incident photons of one wavelength at short-circuit conditions. The number of collected charges depends on the combination of all above mentioned efficiencies(see equation 2.10).

$$EQE = \frac{collected\,charges}{incident\,photons\,of\,one\,energy} = \eta_A \cdot \eta_{ex} \cdot \eta_{diff} \cdot \eta_{ed} \cdot \eta_{ctr} \cdot \eta_{cc} \qquad (2.10)$$

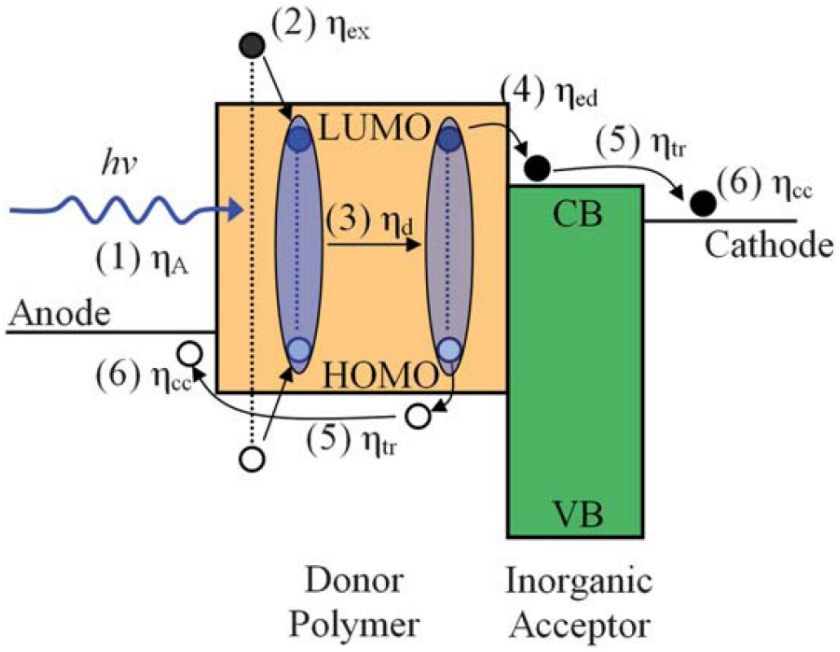

Figure 2.9: Energy level diagram of a polymer- inorganic hybrid solar cell with the schematic mechanism of photocurrent generation. Scheme adapted from reference [97].

Apart from the EQE, the performance of photovoltaic devices are characterized via their current density-voltage curves (I-V curves). Several values are needed to calculate the overall power conversion efficiency η of a device. The current that flows under short circuit conditions I_{SC} is closely related to the number of charges collected at the electrodes. The open-circuit voltage V_{OC} is the voltage at open-circuit conditions and therefore zero current, which is mainly determined by the difference between the quasi-Fermi levels in the donor and acceptor phase.[98] In addition the role of the contacts to the active layer has to be considered.[99] The maximum obtainable power of the solar cell P_{max} is given by the maximum power point at I_{maxP} and V_{maxP} and corresponds to the area of the rectangle underneath the I-V curve (see figure 2.10). These values are correlated by the fill factor FF, which gives a measure of the maximum power of the solar cell related to I_{SC} and V_{OC}:

$$FF = \frac{I_{maxP}\, V_{maxP}}{I_{SC}\, V_{OC}} = \frac{P_{max}}{I_{SC}\, V_{OC}} \tag{2.11}$$

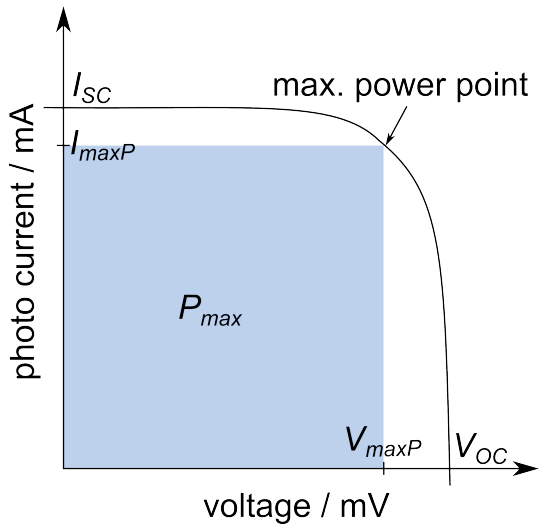

Figure 2.10: I-V-curve of an idealized photovoltaic device marked with the characteristic key parameters.

The overall power conversion efficiency η is a key factor for comparing the efficiency of different solar cells in converting light into electrical energy, and is defined as the ratio of P_{max} and the power of the incident light P_{inc} (equation 2.12).

$$\eta = \frac{P_{max}}{P_{inc}} = \frac{I_{SC}\, V_{OC}\, FF}{P_{inc}} \tag{2.12}$$

Well-defined measurement conditions, especially the applied light spectrum, are the basis for a reliable comparison of devices assembled in different laboratories. The current standard for terrestrial use is the ASTM G173-03 air mass 1.5 global (AM1.5G) spectrum with a total light intensity of 100 $\mathrm{mW\,cm^{-1}}$. The spectrum includes hemispheric illumination by diffuse light and absorption and scattering effects by atmospheric gases. To simulate this artificial 'sun light', laboratory setups typically use a xenon lamp and appropriate filters. The measured photocurrent I is commonly divided by the active area of the solar cells and converted to the current density J.

Chapter 3

Guided In-Situ Polymerization inside a Porous Metal Oxide

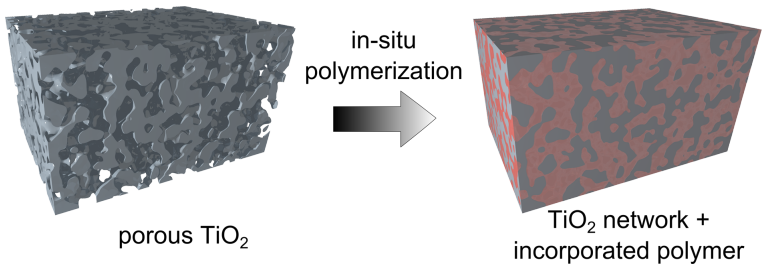

This chapter is based on the following manuscript for an article:

"Guided In-Situ Polymerization inside a Porous Metal Oxide"

Norma K. Minar, Pablo Docampo, Dina Fattakhova-Rohlfing, Thomas Bein,

in preparation for *Applied Materials and Interfaces*

3.1 Abstract

Incorporation of conjugated polymers into a porous metal oxide network is a challenging task, pursued via many different approaches. Here, we developed a guided in-situ polymerization of poly(2-methoxy-5-(2'-ethylhexyloxy)-p-phenylene vinylene) (MEH-PPV) into porous titania films by surface functionalization. The controlled polymerization via the Gilch route was induced by an alkoxide base and increasing the temperature. The selected and specially designed functionalizing linker molecules mimic the monomer or its activated form, respectively. In this way, we drastically enhanced the amount of MEH-PPV incorporated into the porous titania phase compared to non-functionalized samples by a factor of six. Additionally, photovoltaic measurements were performed. The devices show shunting or series resistance limitations depending on the surface functionalization prior to in-situ polymerization of MEH-PPV. We suggest that the reason for this behavior can be found in the orientation of the grown polymer chains with respect to the titania surface. Therefore the geometry of the anchoring via the linker molecules is very important to exploit the full electronic potential of the conjugated polymer in the resulting hybrid composite. This observation will help to design future synthesis methods for new hybrid materials from conjugated polymers and n-type semiconductors to take full advantage of a good electronic interaction between the two phases.

3.2 Introduction

Since their introduction by Heeger et al. in the late 70ties, conducting polymers have inspired a wide breadth of research activities and applications.[100] The great appeal of this new class of materials is the unusual combination of semiconductor and polymer properties. The advantages of polymeric materials - their potential low cost, low weight, good processability and possible fine tuning by organic synthesis are coupled to the enormous diversity of electronic applications. In particular, poly(p-phenylene vinylene) (PPV) was discovered in 1990 as the first electroluminescence polymer[101] and has - together with its derivatives -emerged as the most classical conjugated polymer used in polymer light-emitting diodes (PLEDs) and solar cells.[102,103] Especially, poly(2-methoxy-5-(2'-ethylhexyloxy)-p-phenylene vinylene) (MEH-PPV)has attracted much attention due to its relatively good solubility and easy processability.[104,105] The appeal for commercial applications of electroactive polymers such as MEH-PPV originates mainly from their solution processability which includes advantageous methods such as inkjet and roll-to-roll printing, stamping, drop casting, spin-coating and dip-coating.[106] Nevertheless, the processing on top of a cast polymer film can be severely limited because most solvents will cause swelling, reorganization of the polymer chains and even delamination.[59]

An interesting approach to overcome these stability issues is the covalent attachment of brushes of conjugated polymers onto surfaces. Polymer brushes in general are applied to tailor the interface and thus control surface properties such as wettability, biofouling resistance, adhesion, and stimuli responsiveness.[107] By anchoring conducting polymers such as MEH-PPV, the surface-related electronic properties of various materials can be tuned.[108–110] Through this approach, well-defined morphologies in heterojunction materials can in principle be constructed which result

in controlled electronic properties and enhanced interaction efficiencies between the two phases.[111,112]

Generally there are two methods for tethering polymer brushes: " grafting to" and " grafting from" approaches.[59] The " grafting to" method employs a preformed polymer with a reactive end group to attach the polymer chain to the surface. Opposite to this, in the " grafting from" approach polymer chains are grown directly from the surface. Several advantages of the " grafting from" strategy include a higher surface coverage, better suitability for high molecular weight polymers and improved access to inner and outer surfaces of porous inorganic matrices.[59] The incorporation of polymers within nanostructured inorganic scaffolds opens up opportunities to engineer advanced materials with highly tunable features such as mechanical, chemical, optical, and electrical properties.[55,113–117] Since the mid-1990ties there have been several attempts to integrate conjugated polymers into porous substrates by various polymerization techniques.[56,117–120] One elaborate way to introduce a conjugated polymer into a porous titania scaffold efficiently was shown by Zhang et al. for poly(3-hexyl)thiophene (P3HT).[121] In this approach, a surface functionalization of the porous material steered the growth of the P3HT onto the inner surface of the porous inorganic substrate. Employing this method, a larger surface coverage and consequently a more efficient photoinjection from the P3HT to the titania could be achieved compared to *ex-situ* synthesized and infiltrated P3HT .[121]

Here we have, for the first time, adapted the surface functionalization approach for the MEH-PPV polymer and applied it to a mesoporous titania scaffold. The Gilch-route was the synthesis route of choice for MEH-PPV because it is an inexpensive, non-toxic polymerization route initiated with an alkoxide base and by increasing the temperature.[122] The surface-functionalizing molecules were chosen and designed to mimic the monomer units. As a porous matrix we have used mesoporous titania

films with a mean pore size of 20 nm, which are typically used in the hybrid solar cells.[123,124] Moreover, we have tested the feasibility of this approach for incorporation of polymer into titania films with even smaller pores of around 10 nm.[125] The surface functionalization was monitored by reflection-absorption infra-red spectroscopy (RAIR). The properties of the in-situ polymerized MEH-PPV inside the mesoporous titania were characterized via UV-Vis spectroscopy. Atomic force microscopy (AFM) and transmission electron microscopy (TEM) measurements provided information about the morphology of the porous titania films with the incorporated in-situ polymerized MEH-PPV. Additionally, photovoltaic performance measurements provided data about the differing electronic properties depending on the functionalization.

3.3 Experimental

Materials

2-Ethylhexyl bromide was purchased from ACROS ORGANICS and used as received. All other materials were purchased from SIGMA-ALDRICH CO. and used without further purification.

Methods

Reflection-absorption IR (RAIR) spectra were recorded with a BRUKER IFS 66v FTIR spectrometer. The sample chamber with a variable angle reflection accessory (A-513) was maintained at 2 mbar during the entire measurement by means of an EDWARDS rotary-pump. In a typical measurement on silicon substrates, an angle of incidence of 54°to the surface normal was used. UV-Vis measurements were performed on a HITACHI U3501 spectrophotometer equipped with an integrating sphere. Absorbance spectra were recorded in transmission geometry with

plain glass or fluorine-doped tin oxide (FTO) coated glass as reference. Exposure to oxygen plasma was carried out with a Femto Plasma System from DIENER ELECTRONIC typically operated at a power of 50 W and an oxygen flow of 4-5 sccm. Gel-permeation chromatography (GPC) was performed on an AGILENT 1200 Series machine equipped with a PSS SDV Lux precolumn (5 µ, 8.0×50 mm) followed by a PSS SDV Lux (1000 Å, 5 µ, 8.0×300 mm) column. Tetrahydrofurane (THF) was used as eluent with a flow rate of 1 mL min^{-1}. Atomic force microscopy (AFM) images were recorded with a NANOINK NScriptor DPN system in tapping mode. Transmission electron microscopy (TEM) was performed using a FEI Titan 80–300 instrument equipped with a field emission gun operated at 300 kV. Samples for TEM measurements were prepared by removing porous titania films with 20 nm pore size grafted with acrylic acid and subsequent in-situ polymerization from the glass substrate and applied to a holey copper grid. For comparison a bare calcined porous titania film was investigated. Current-voltage characteristics were measured under simulated AM1.5G solar irradiation (SOLAR LIGHT Model 16S) at 100 mW cm^{-2} and argon atmosphere. The light intensity was monitored with a FRAUNHOFER ISE-calibrated silicon reference cell equipped with a KG5 filter for reduced spectral mismatch. *J-V* curves were recorded using a KEITHLEY 2400 source meter. For liquid nuclear-magnetic-resonance (NMR) characterization of the observed signal multiplicities the following abbreviations were used: s (singlet), d (doublet), t (triplet), q (quartet), dd (doublet of a doublet), ddd (doublet of a doublet of a doublet), dt (doublet of triplet), tt (triplet of triplet) and m (multiplet).

Synthesis of Monomer 1,4 - Bis(bromomethyl) - 2 - (2 - ethylhexyloxy) - 5 - methoxybenzene 1

In a first step 1-(2-ethylhexyloxy)-4-methoxybenzene was synthesized according to Anderson et al..[126] 4-Methoxyphenole (≥98 %, 2.48 g, 20 mmol) was dissolved in 10 mL dimethylformamide (DMF) in a 50 mL-flask in ambient atmosphere and 2.24 g of K ^{t}BuO (≥98 %, 20 mmol) was added in one portion under continuous stirring. The solution temperature reached 50 °C. 3.56 mL of 2-ethylhexyl bromide (95 %, 20 mmol) was added drop wise over 45 min. Shortly afterwards the greenish solution turned brown and solids began to precipitate. After 40 min stirring, another portion of K^{t}BuO (1.12 g, 10 mmol) was added and afterwards 2-ethylhexyl bromide (1.8 mL, 10 mmol) was slowly added over 30 min. After another 40 min of stirring, a final addition with 0.56 g K^{t}BuO (5 mmol) and 0.9 mL 2-ethylhexyl bromide (5 mmol) was performed. The reaction mixture was left at room temperature for 3 h. All precipitates were dissolved upon the addition of water (10 mL). The reaction solution was extracted three times with diethyl ether (3×50 mL) and the organic phase was washed with water (50 mL) followed by brine (50 mL) and dried over $MgSO_4$. The solvent was removed under vacuum. The crude product was distilled at 0.1 torr and 100-120 °C to give a colorless liquid.

^{1}H NMR (270 MHz, $CDCl_3$, TMS): δ = 6.80 (s, 4H), 3.74 (d, J = 5.7 Hz, 2H), 3.73 (s, 3H), 1.66 (m, 1H), 1.52-1.21 (m, 8H), 0.90-0.82 (m, 6H) ppm.

^{13}C NMR (270 MHz, $CDCl_3$, TMS): δ = 153.86, 115.68, 114.82, 71.47, 55.95, 39.71, 30.77, 29.34, 24.11, 23.30, 14.29, 11.32 ppm.

The bromomethylation of 1-(2-ethylhexyloxy)-4-methoxybenzene was conducted after a method described by Neef et al..[127] 1-(2-Ethylhexyloxy)-4-methoxybenzene (5 g, 21 mmol) and paraformaldehyde (3 g, 100 mmol) were dissolved in 10 mL

acetic acid and 10 mL hydro bromic acid in acetic acid (33 wt%, 43 mmol) in a 50 mL-flask in ambient atmosphere under continuous stirring. The reaction solution was heated to 70 °C for 4 h under nitrogen atmosphere. After cooling down to room temperature, the reaction solution was diluted with chloroform (15 mL) and washed carefully with water and saturated aqueous $NaHCO_3$ solution (50 mL each). The chloroform phase was dried over $MgSO_4$ and subsequently the chloroform was removed under reduced pressure. The pure product was obtained after recrystallization from hexane as nearly colorless powder.

^{1}H NMR (270 MHz, $CDCl_3$, TMS): δ = 6.86 (s, 4H), 4.52 (s, 4H), 3.87 (s, 5H), 1.8-0.8 (m, 15H) ppm.

^{13}C NMR (270 MHz, $CDCl_3$, TMS): δ = 151.11, 151.05, 127.55, 127.41, 114.37, 113.84, 71.01, 56.32, 39.68, 30.71, 29.19, 28.76, 28.71, 24.10, 23.13, 14.18, 11.33 ppm.

Synthesis of 'Monomer Acid' ((2,5 - bis(bromomethyl) - 4 - methoxyphenoxy) acetic acid) 4

Similar to the synthesis of the monomer **1**, a carboxylated monomer was synthesized in a two-step protocol. First, (4-methoxyphenoxy)acetic acid was synthesized according to a procedure described in the literature.[128] In a 500 mL-flask under ambient atmosphere, methyl chloroacetate (99 %, 17.3 g, 0.16 mmol) was dissolved in an 8 wt% aqueous sodium hydroxide solution (175 mL) and added to a stirred solution of 4-methoxyphenol (10 g, 81 mmol) in 5 wt% aqueous sodium hydroxide solution (67 mL). The reaction mixture was heated to 80 °C for 9 h and afterwards to 65 °C for 14 h. After cooling down to room temperature the solution was acidified with HCl (1M, to pH = 5.2), and extracted with Et_2O (2×150 mL). The organic phase was dried over $MgSO_4$, filtered and the solvent was removed under reduced

pressure to give the crude product. Recrystallization from heptane yielded colorless plate like crystals of (4-methoxyphenoxy)acetic acid.

In the second synthesis step, the (4-methoxyphenoxy)acetic acid was bromomethylated.[129] Under nitrogen atmosphere in a 250 mL-flask, (4-methoxyphenoxy)acetic acid (4 g, 22 mmol) and paraformaldehyde (1.4 g, 16 mmol) were dissolved in 40 mL acetic acid and 10 mL hydrobromic acid in acetic acid (33 wt%, 43 mmol). The reaction solution was heated to 65 °C for 6.5 h. Afterwards 82 mL of water was added and the colorless precipitate was filtered off and washed with water until the filtrate had a pH value around 6. The colorless powder was dried under reduced pressure and yielded clean (2,5-bis(bromomethyl)-4-methoxyphenoxy) acetic acid **4**.

^{1}H NMR (270 MHz, DMSO - d_6): δ = 7.13 (s, 1H), 7.09 (s, 1H), 4.71 (s, 2H), 4.68 (s, 2H), 4.58 (s, 2H), 3.81 (s, 3H) ppm.

^{13}C NMR (270 MHz, DMSO - d_6): δ = 170.63, 152.03, 150.06, 128.38, 127.53, 116.14, 114.61, 66.27, 56.68, 30.07 ppm.

Fabrication of Mesoporous Titania Films

Mesoporous Titania - 10 nm Pore Size

Mesoporous titania with an average pore size of 10 nm was synthesized according to the 'brick and mortar' procedure developed in our group.[130]

Titanium dioxide nanoparticles were prepared using a modified procedure developed by Niederberger et al..[131] Titanium tetrachloride (99.9 %, 1.5 mL, 13.7 mmol) was dissolved in anhydrous toluene (10 mL) and added to benzyl alcohol (30 mL, 291 mmol)in a 100 mL Nalgene^{TM}polycarbonate autoclave under continuous stirring. The solution was kept at 60 °C for 20 h without stirring and was then cooled down to room temperature. The resulting particles were separated by centrifuga-

tion at 50000 rcf for 30 min and used without further treatment. The centrifuged particles (without being subjected to washing procedures) contain about 45 wt% of benzyl alcohol according to thermogravimetric analysis; this was taken into account for the adjustment of the TiO_2-content. To obtain a coating solution with 70 wt% TiO_2 nanoparticles and 30 wt% sol-gel titania precursors (based on the total Ti-content in the final solution), a solution of Pluronic F127 (0.3 g, 0.02 mmol) in THF (4 mL) was added to centrifuged, unwashed particles (0.4 g, 2.2 mmol of TiO_2), ultrasonicated and stirred overnight until the particles were homogeneously redispersed. Subsequently, 0.4 mL (corresponding to 1.1 mmol TiO_2) of a prehydrolyzed sol-gel solution and 2.8 mL THF was added (sol-gel solution, see below), and the mixture was stirred for several minutes. The final solutions were transparent or translucent, being of a yellow to orange color. The sol-gel solution was prepared by adding hydrochloric acid (37 %, 5.1 mL, 62.1 mmol) to tetraethyl orthotitanate (7.2 mL, 34.3 mmol) under continuous stirring for about 10 min at room temperature in a 25 mL glass flask. The films (around 380 nm thick) were prepared on FTO-coated glass (TEC-7 from Pilkington) by spin-coating (50–80 µL per 1 cm^2 substrate area) at 2000 rpm and calcined at 450 °C (0.9 °C min^{-1}) for 30 min.

Mesoporous Titania - 20 nm Pore Size

To synthesize mesoporous titania films with different thicknesses the DSL 18 NR-T paste from DYESOL was diluted with different amounts of ethanol. For a final thickness of around 1 µm 0.25 g paste was diluted with 0.50 mL ethanol. Thinner films with around 450 nm thickness were produced from a dilution of 0.25 g paste with 0.80 mL ethanol. The diluted paste was ultrasonicated for 2 h to ensure a colloidal mixing. The ethanol solution was spin-coated on different substrates (e.g. silicon, glass, fluorine-doped tin oxide) at 2000 rpm. All substrates were treated with

oxygen plasma for 5 min beforehand. The resulting films were calcined at 450 °C for 30 min with a heating rate of 0.9 °C min^{-1}.

Functionalization of Titania Films

The surface of mesoporous titania films was functionalized by immersing the titania films (3 substrates with 1.5×1.5 cm^2 film area each) in a 25 mM (16 mL) solution of the according linker molecule in dry acetone. The films were cleaned in oxygen plasma for 10 min beforehand. The solution was refluxed at 70 °C for 3 h before the films were removed and rinsed with acetone and stored in the dark.

In-situ Polymerization of MEH-PPV

72 mg of monomer (0.17 mmol) was solved in dry THF (17 mL) and stirred under N_2 atmosphere in a 25 mL schlenk tube to get a 10 mM solution. The titania films (3 substrates with 1.5×1.5 cm^2 film area each) were immersed in the solution without touching the walls of the vessel or disturbing the stirring bar. The reaction vessel was cooled down to −80 °C under continuous stirring and a suspension of 114 mg of potassium *tert*-butoxide in THF (2 mL) was added slowly through a septum. The cooling bath was removed after 30 min and the reaction vessel was allowed to warm to room temperature. After 3 h stirring at room temperature, the films were removed and rinsed with dry THF and methanol. Not-attached MEH-PPV was washed off with chlorobenzene and the films were subsequently dried under vacuum for 1 h and kept in the dark.

Solar cell Assembly

For photovoltaic measurements the mesoporous titania films were prepared on FTO substrates coated with a dense titania layer. The dense titania blocking layer was

prepared by spin coating 50 µL of a sol-gel solution at 4000 rpm on a patterned FTO substrate (2×1.5 cm^2). The titania sol-gel solution was produced by adding 0.75 mL (9 mmol) of concentrated hydrochloric acid to 1.05 mL (5 mmol) tetraethyl orthotitanate (TEOT), and was further diluted with 15 mL THF. After calcination at 450 °C for 30 min (0.9 °C min^{-1}), mesoporous titania films (20 nm pore size, 450 nm thick) were applied as mentioned above.

After functionalization and in-situ polymerization as described above, a cover layer of MEH-PPV had to be applied to prevent contacting of the titania with the top electrode and thus prevent short-circuited devices. For this purpose, a solution of MEH-PPV (3 mg mL^{-1}, 150-250 kDa) in chlorobenzene was left soaking for 60 seconds on the mesoporous films (65 µL/2.25 cm^2) and afterwards the films were spin coated at 1000 rpm for 60 sec.

After drying the films for 15 min at 120 °C under reduced pressure (2×10^{-2} mbar), a PEDOT:PSS layer was applied. A diluted PEDOT:PSS solution (2.5/1 = isopropanol/aqueous PEDOT:PSS) was left for 60 sec on the substrates and then spin coated at 1000 rpm for 60 sec. The films were again dried for 15 min at 110 °C under reduced pressure (2×10^{-2} mbar).

100 nm thick silver electrodes were evaporated through a mask to yield an active area of 0.11 cm^2 for the final devices.

3.4 Results and Discussion

Our approach of a guided in-situ polymerization of MEH-PPV into mesoporous titania films was accomplished by grafting different functional molecules onto the surface of the titanium dioxide. The functionalization was intended to enable a targeted polymerization from the titania surface by participating in the process as starting point of a growing polymer chain or as reaction partner of oligomers al-

ready formed in solution.[132] The selection of functional molecules was based on the polymerization mechanism of the applied Gilch route, which is schematically depicted in figure3.1A.[133] This approach is viewed as particularly interesting because it allows control of the polymer chain growth by tuning the reaction temperature. It is generally accepted that the active monomer for chain growth is α-halo-*p*-quinodimethane, which results from an E_2 elimination reaction of the monomer with the non-nucleophilic base potassium *tert*-butoxide.[122,134] Accordingly, the grafted functional molecules mimic either the monomer structure ('monomer acid', molecule **4**) or a part of the already activated monomer **2**(such as acrylic acid, molecule **3**) (see figure 3.1A). Benzoic acid **5** was used as a reference molecule that cannot participate in the polymerization process and therefore cannot interfere with the chain growth of the MEH-PPV on the titania surface.

The successful functionalization of the mesoporous titania films was verified via Reflection-Absorption IR (RAIR) spectroscopy, as shown in figure 3.2. The strongest absorption at around 835 cm^{-1} corresponds to the inorganic Ti-O network.

Signals indicating aromatic moieties of the grafted molecules arise in the range from 1500 to 1600 cm^{-1}. The vibrational modes of the carboxyl groups can be seen in the spectra of the functionalized films at around 1200, 1400 and 1725 cm^{-1}. Especially in the RAIR-spectrum of the sample grafted with 'monomer acid' **4** there are also peaks visible for C-H vibrations of the O-CH_3 and CH_2 groups around and below 3000 cm^{-1}.

The in-situ polymerization of MEH-PPV within the mesoporous titania films was performed by immersing the samples vertically in a solution of 1,4-bis(bromomethyl)-2-(2-ethylhexyloxy)-5-methoxybenzene, the monomer **1**, in tetrahydrofuran (THF). The reaction vessel was cooled down to −80 °C and then the base KO^tBu is added. At this low temperature the monomer is fully converted into the activated form α-

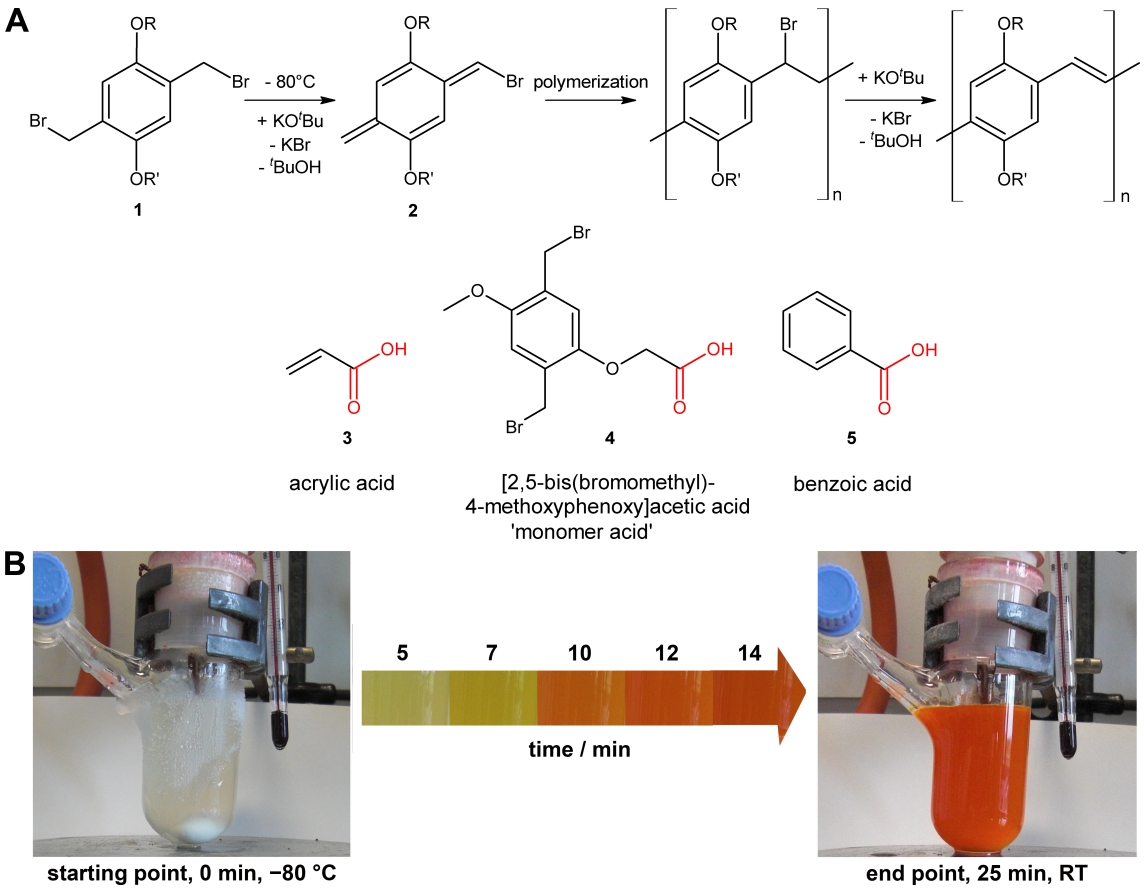

Figure 3.1: **A** Top: Reaction scheme of the polymerization via the activated monomer 2, a *p*-quinodimethane. R = CH_3, R' = 2-Ethyl(hexyl). Bottom: Selected molecules used for the functionalization of the titania surface. Carboxylic acid moieties acting as titania-specific anchor groups are depicted in red. **B**: Illustration of the timeline of the thermally induced polymerization process.

bromo-*p*-quinodimethane **2** (see figure 3.1A).[122] This activated monomer can then react to a diradical induced by increasing the temperature, which is the starting point of the chain growth via a radical polymerization.[135]

The progress of the polymerization reaction can be easily followed by the red shifting and increasing optical absorption of the reaction mixture, illustrated in figure 3.1B. At the starting temperature of −80 °C, the solution of the monomer and the reactants is clear and colorless. Once the thermally-induced polymerization sets off, the increasing chain length of the resulting MEH-PPV induces a bathochromic shift of the absorption and the color of the reaction mixture changes gradually from light

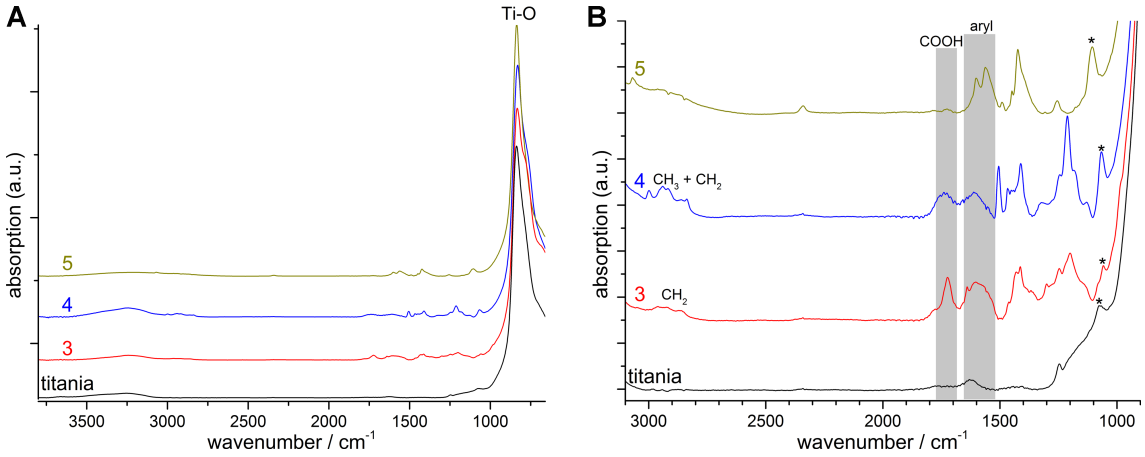

Figure 3.2: **A**, reflection-absorption IR spectra of a non-functionalized titania film and films grafted with different carboxylic acids **3**, **4** and **5**. All spectra are normalized to the Ti-O signal around 835 cm^{-1}. Signals marked with an asterisk correspond to the thin layer of SiO_2 of the silicon substrates underneath the titania films. **B**, zoomed in spectra from **A** to display the signals corresponding to the grafted molecules.

yellow to dark orange (see figure 3.1B).[135]

The pronounced effect of the surface functionalization on the amount of included MEH-PPV is already clearly visible by eye (see figure 3.3A). Films that were grafted with acrylic acid before the in-situ polymerization are intensively orange in contrast to non-functionalized films which show only very light orange coloring. The functionalized and polymerized samples are homogeneously colored which is remarkable, considering the relatively thick porous titania layer of over 1.5 µm. In figure 3.3B the corresponding UV-Vis spectra of titania films with a pore size of 20 nm, typically used in dye-sensitized solar cells, are compared. The grafting of the titania surface with acrylic acid **3** or 'monomer acid' **4** enhances the absorbance at 490 nm by a factor of 3.3 and 5.7 compared to non-functionalized and in-situ polymerized samples, respectively.

One major question related to polymer chains grown from a surface is the influence of the confinement effects imposed by the substrate.[62] Therefore, in addition to the mesoporous titania films with a relatively large pore diameter of 20 nm we investigated the grafting and in-situ polymerization method also with titania films with a

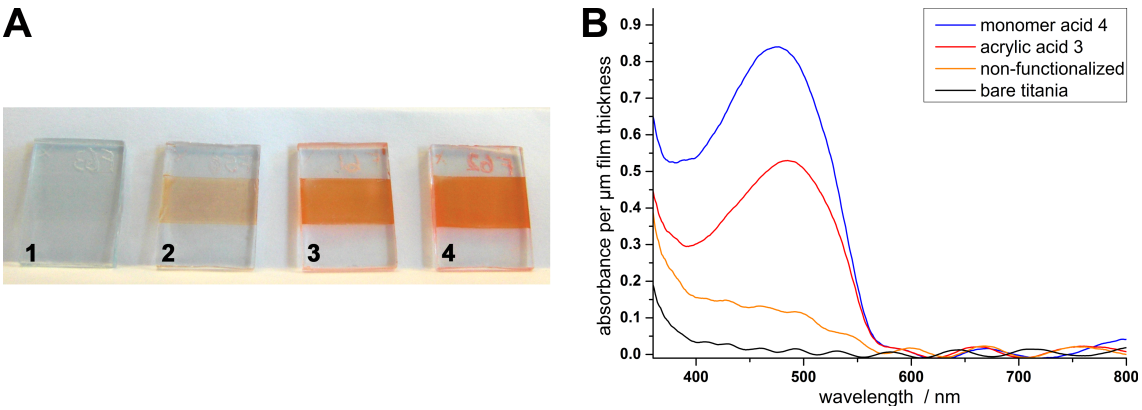

Figure 3.3: Effect of functionalization on in-situ polymerization:**A**, Picture of mesoporous TiO_2 films (20 nm pore diameter) before polymerization (**1**; film thickness 1.5 µm) and after in-situ polymerization: non-functionalized and in-situ polymerized film (**2**, 1.5 µm thickness), acrylic acid functionalized and in-situ polymerized films with the thickness of 1.5 (**3**) and 2 µm (**4**). All films are deposited on FTO - substrates. **B**, Absorbance spectra of in-situ polymerized titania films with different functionalization. The spectra are normalized to the film thickness.

smaller pore diameter of only 10 nm. Even with these small pores the absorbance after in-situ polymerization of the functionalized titania surfaces is strongly enhanced compared to non-functionalized samples (see figure 3.4A).

To prove that the polymerization was indeed guided by the grafted molecules actively participating in the polymer chain growth, and not by other surface effects, we conducted two reference experiments. On the one hand, benzoic acid **5** was grafted onto the titania surface to change the polarity of the titania towards a more hydrophobic character without providing a polymerizable moiety.

On the other hand, to ensure that the surface properties of titania were not affected by other conditions of the grafting process, such as prolonged refluxing, and thus promoted the in-situ polymerization in some way, titania films were refluxed in plain acetone without any linker molecule ('No Linker'). After the in-situ polymerization both samples - benzoic acid and 'No Linker' - show only a low absorbance around 500 nm that is strikingly smaller compared to the acrylic acid grafting (cp. figure 3.4A).

Another difference between the benzoic acid and the acrylic acid grafting is the strength of interaction of the MEH-PPV with the titania films, which was tested by thoroughly washing the in-situ polymerized samples with chlorobenzene. After this washing step, samples functionalized with acrylic acid show a three times less reduced absorbance, and therefore less reduced amount of MEH-PPV, than benzoic acid grafted samples, as shown in figure 3.4B. This indicates that in contrast to the benzoic acid grafted titania, most of the grown polymer chains in the acrylic acid functionalized films are covalently attached to the titania surface and/or remain inside the porous network and cannot be washed off. As expected, the change of the hydrophilic titania surface towards a hydrophobic surface - covered with benzyl groups - did not support the incorporation of the polymer.

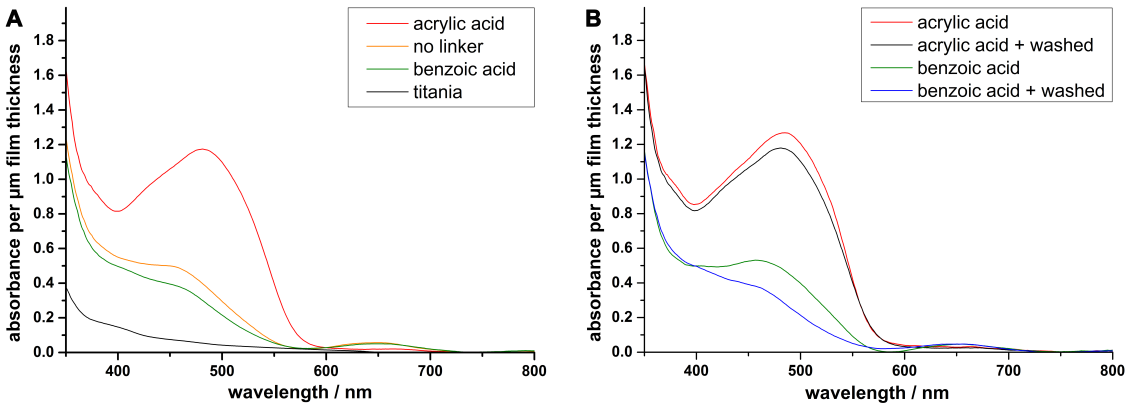

Figure 3.4: UV-Vis spectra of in-situ polymerized 'brick and mortar' titania films (10 nm pore diameter). **A**, comparison of different linker molecules ('acrylic acid', 'benzoic acid') and treatments ('no linker' - reflux in acetone) after in-situ polymerization with non-treated titania ('titania'). **B**, comparison of the impact of rinsing in-situ polymerized samples in chlorobenzene ('washed').

Further information about the quality of the synthesized polymer, in the form of the HOMO-LUMO level energy gap E_g, can be extracted from the Tauc plots[76] of corresponding UV-Vis data (see table 3.1 and figure 3.5). The value of the optical band gap E_g correlates with the conjugation length of the polymer. The latter relies on the overlap of the π-orbitals of the aromatic bonds, which in turn requires the

phenyl rings and the vinyl bonds, i.e. the polymer backbone, to be coplanar.[136] The size of the energy gap E_g decreases with increasing conjugation length and saturates already at 20 monomer repeat units.[137,138]

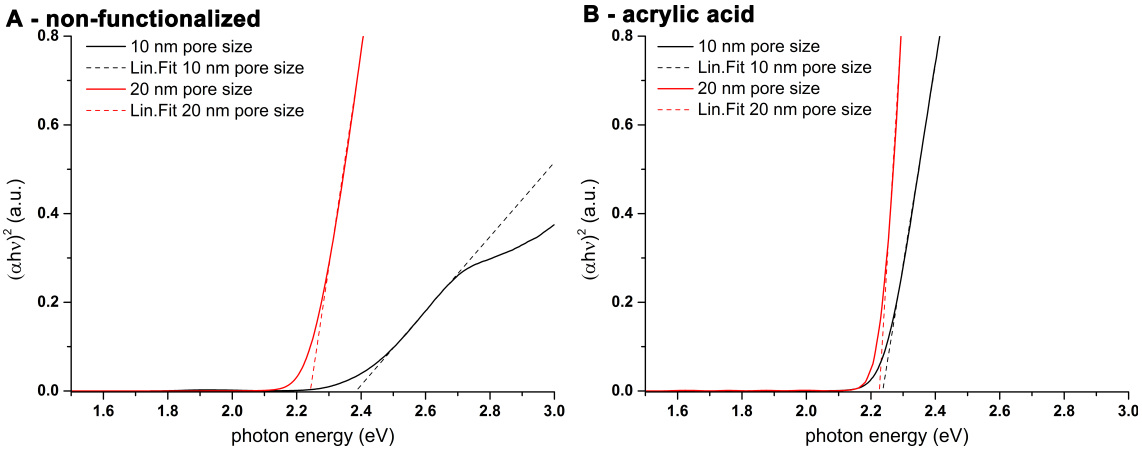

Figure 3.5: Tauc plots of mesoporous titania films with different pore sizes and without functionalization and in-situ polymerization (**A**) and with acrylic acid grafting and in-situ polymerization (**B**), respectively.

Many examples in the literature state that polymers synthesized in a confined space have a limited chain length and more defects compared to solution synthesized polymers, and therefore show a reduced conjugation length.[62,64,118,139,140] We made a similar observation for our systems. UV-Vis measurements reveal that the commercially available MEH-PPV (40–70 kDa) and MEH-PPV synthesized in solution via the Gilch-route exhibit a narrower optical band gap compared to the MEH-PPV synthesized inside the porous host (c.f. table 3.1). Moreover, in a size exclusion chromatography measurement the size of the MEH-PPV synthesized via the Gilch-route was compared with the commercial sample of 40–70 kDa and showed an only slightly decreased chain length (figure 3.6).

Juxtaposing the E_g values of MEH-PPV synthesized in titania with different pore diameters in table 3.1 gives a clear indication that the conjugation length is diminished for the smaller pore size. This seems to be counteracted by the functionalization of the titania surface with active molecules. This way the E_g value for acrylic acid

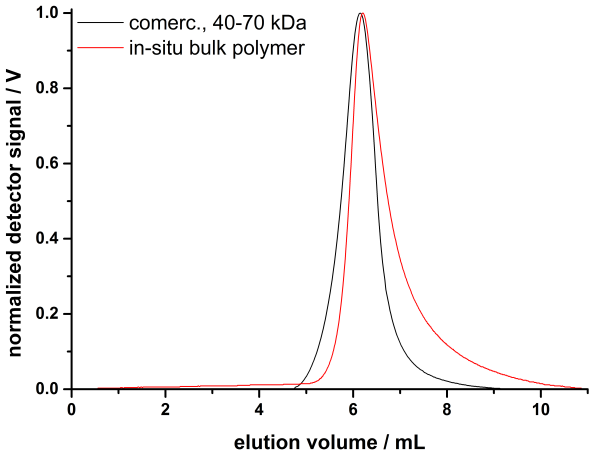

Figure 3.6: Elution diagram comparing a commercial MEH-PPV with the bulk polymer obtained in solution at the in-situ polymerization. The detector signal is taken from the UV-Vis detector at 235 nm. The synthesized bulk polymer has a comparable but slightly decreased chain length compared to the 40–70kDa sample.

functionalized films in the 10 nm pore system is similar to the value of MEH-PPV in non-functionalized 20 nm pore size titania. It appears that the functionalization in the smaller pores facilitates the polymerization and neutralizes limiting factors for the resulting conjugation length. Such a limitation does not seem to be substantial in the 20 nm pore size system, because the obtained E_g values are independent of the titania surface treatment (table 3.1).

Although the optical band gap of the synthesized MEH-PPV is not affected by the functionalization in the bigger pore system, the UV-Vis data show (c.f. figure 3.3 and 3.4) that the amount of polymer that is incorporated increases significantly, regardless of the titania pore size. The surface functionalization with active molecules such as acrylic acid **3** and 'monomer acid' **4** seems to overcome the diffusion limitation and possibly enhances the chain growth inside the titania films. The total amount of conjugated photoactive polymer incorporated into the porous voids of the metal oxide semiconductor network is of special importance for hybrid bulk heterojunction devices.[141]

Table 3.1: E_g values of different functionalization and pore sizes extracted from Tauc Plots. For comparison the energy values of commercial and in-situ synthesized bulk polymer are also listed.

pore diameter in nm	**grafting procedure**	**band gap E_g [eV] of in-situ grown MEH-PPV**
20 nm	no Linker	2.24
	acrylic acid **3**	2.23
	'monomer acid' **4**	2.26
10 nm	no Linker	2.38
	benzoic acid **5**	2.43
	acrylic acid **3**	2.24
bulk in-situ synthesized MEH-PPV		2.10
commercial MEH-PPV (40–70 kDa)		2.15

In hybrid solar cells based on titania and a conjugated polymer, excitons are created in the polymer phase upon photoexcitation and quenched at the titania interface after their diffusion towards the polymer/titania heterojunction.[142] A high interfacial area between the two phases is essential for a good charge transfer between the conjugated polymer and the titania film. This can be achieved through a high degree of pore filling of the nanostructured metal oxide with the conjugated polymer. Abrusci et al. showed that an optimum for an efficient polymer-based hybrid solar cell is reached at about 25 % pore filling.[143] For example, in the case of 'monomer acid' **4** functionalized films (20 nm pores) the absorption due to MEH-PPV obtained by in-situ polymerization inside the pores (figure 3.3B) is equivalent to a 125 nm thick dense film, assuming an extinction coefficient of around $1.5{\cdot}10^5$ cm^{-1}.[144] The film thickness measured by a profilometer was not increased after the polymerization, which implies that the synthesized polymer is located fully inside the pores, rather than being formed on the top of the titania network. This corresponds to a theoretical pore filling of around 25 % assuming a porosity of 50 % for the meso-

porous films prepared from titania paste.[145] This conclusion is further supported by AFM measurements of titania films before and after grafting ('monomer acid' **4**)and subsequent in-situ polymerization as shown in figure 3.7. The surface of the bare titania film features sharp edges and crystal faces of the crystalline anatase particles (c.f. figure 3.7A). In contrast, the surface morphology of a MEH-PPV loaded film displays rounded smoothed features as shown in figure 3.7B. This implies that the polymer completely covers the accessible surface of the anatase particles. The AFM image also shows that there is no closed polymer film on the surface and that the textural porosity is sustained.

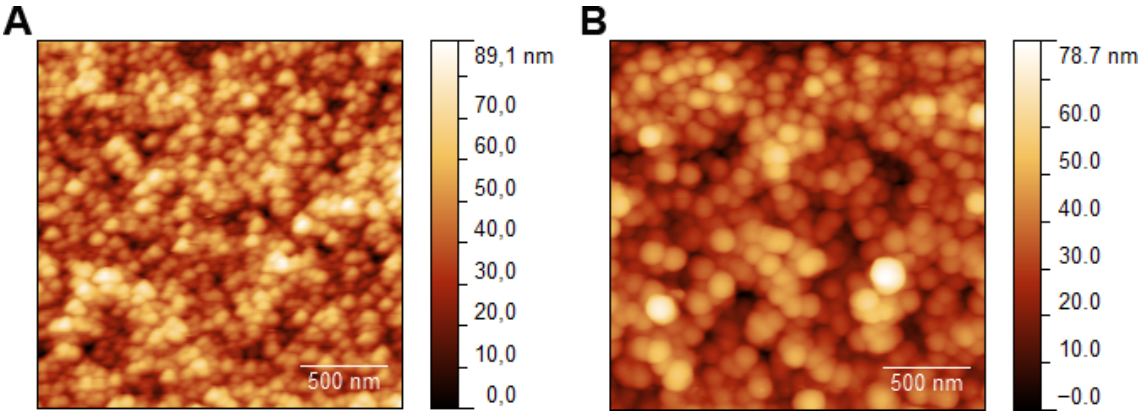

Figure 3.7: AFM measurements of differently treated titania films (20 nm pores, 20 nm anatase particles) in tapping mode. **A**, bare calcined titania. **B**, titania film after 'monomer acid' functionalization and subsequent in-situ polymerization.

To get better insights regarding the coverage of the titania surface with in-situ synthesized polymer, TEM measurements of removed film material were performed. In the TEM micrographs in figure 3.8B1–3, the 20 nm anatase particles can be seen embedded in a layer of MEH-PPV. The accessible surface of the anatase particles seems to be fully covered with polymer, as shown in the AFM images in figure 3.7B. In contrast, the TEM micrographs of bare, calcined titania films show the crystalline titania particles without any organic layer (see figure 3.8A1–3). The contrast of the inorganic oxide particles is clearer and the lattice fringes of anatase

are more prominent.

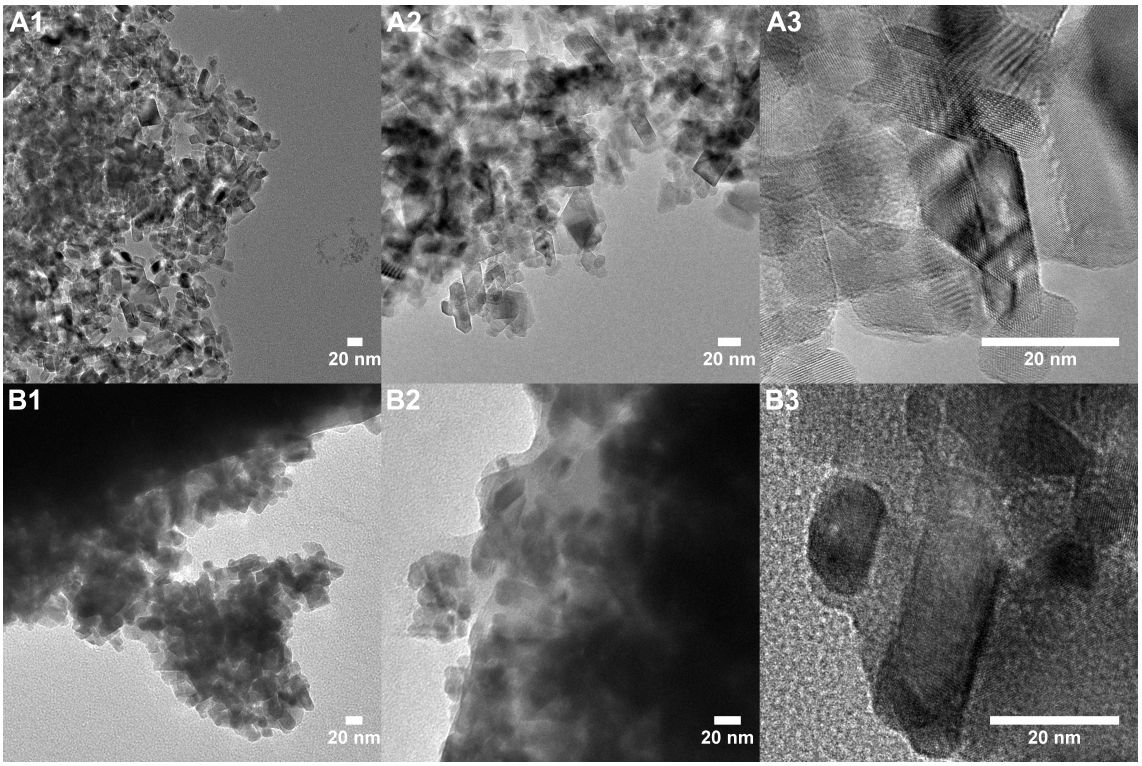

Figure 3.8: TEM micrograph of removed titania films of 1 µm thickness. **A1**–**A3**, titania films after calcination. **B1**–**B3**, titania films grafted with acrylic acid and after in-situ polymerization.

As already mentioned above, conjugated polymers synthesized in a confined space are likely to show a diminished conjugation length and a higher defect density compared to samples synthesized in solution, which may result in reduced charge mobility.[146] In this context, in-situ polymerized MEH-PPV inside porous titania films with 20 nm pores was further studied for applications in photovoltaic devices, as shown in figure 3.9.

Here, we can clearly observe three different regimes for the 3 studied systems. The performance of devices based on non-functionalized TiO_2 samples is clearly limited by shunting, as evidenced by the very low open circuit voltage. This could very likely be the result of incomplete surface coverage of MEH-PPV on the TiO_2 surface. This would result in a direct contact between the evaporated gold cathode and

the exposed TiO_2 surface, which would result in a shorting path.[147]

Devices based on 'monomer acid' **4** functionalized and in-situ polymerized titania films, while showing the highest open circuit voltages, are clearly limited by series resistance losses.[148] These devices also exhibit the lowest short circuit currents, which is counter intuitive if we consider that these films show the highest light capture of the set. In contrast, the series resistance losses for devices based on acrylic acid **3** functionalized titania films are much lower than their 'monomer acid' **4**counterparts, and also resulted in the highest photovoltaic performance of the set.

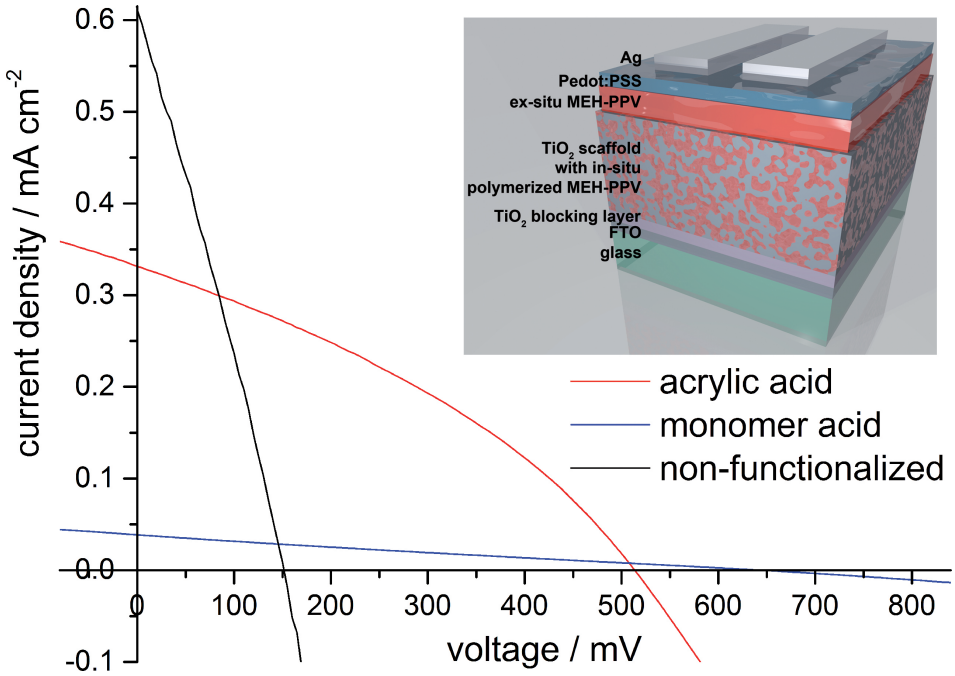

Figure 3.9: *J-V* curves under AM 1.5 sunlight illumination of devices with functionalized and in-situ polymerized titania films. The inset shows schematically the device layout with the different layers.

To understand these differences, we consider the influence of the molecular structure of the surface-linker on the growth of the polymer chains, which is schematically depicted in figure 3.10. We hypothesize that polymer growth seeded by the acrylic acid group results in polymer chains protruding more or less perpendicularly to the titania surface due to the geometry of the molecule, as depicted in figure 3.10A. In

the case of ‚monomer acid' **4** sensitized titania, there exist two nucleation points for the polymer growth on the side of the molecule. Here, we hypothesize that this results in polymer chain growth preferentially lying parallel to the surface of titania as shown in figure 3.10B.

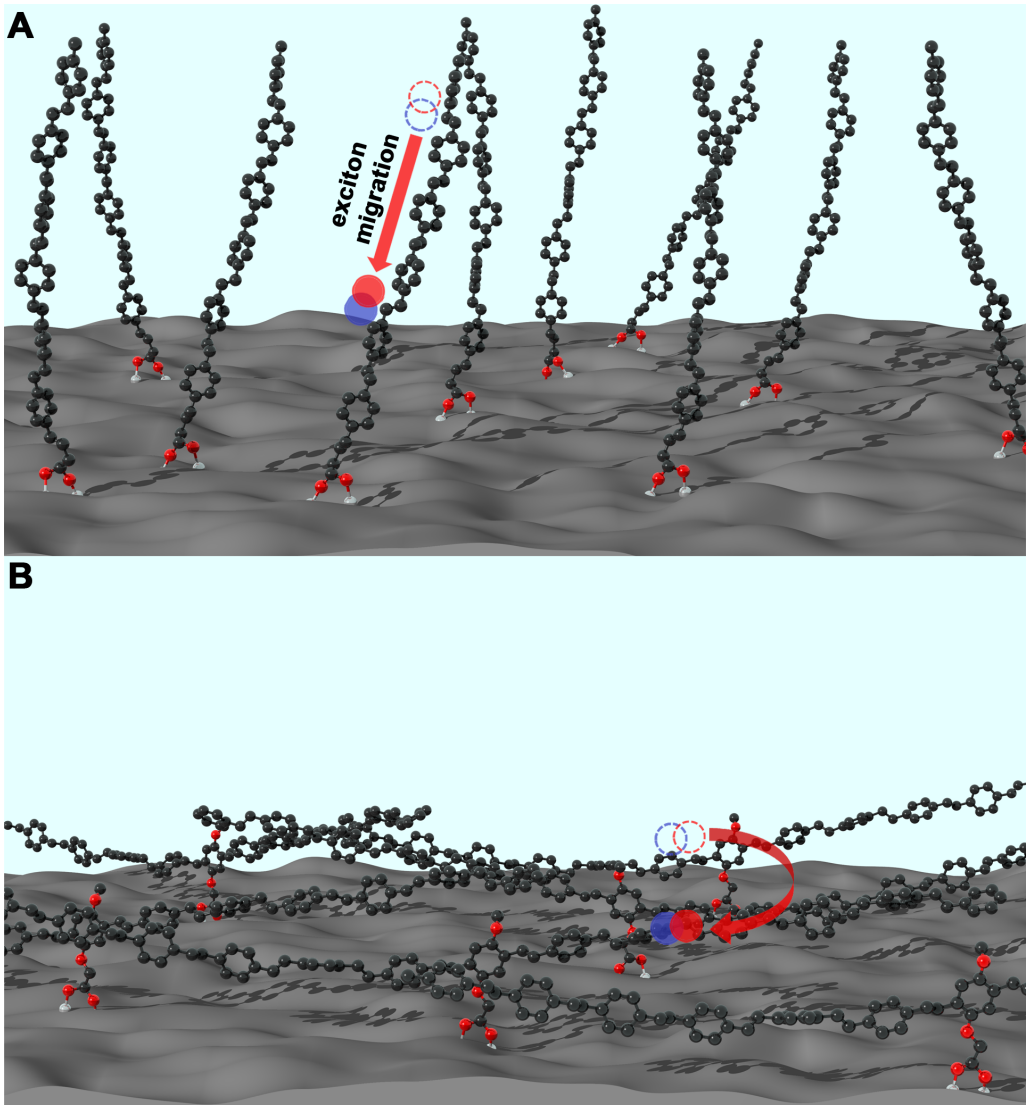

Figure 3.10: Schematic picture of different possible polymer chain orientations depending on the anchor molecule. For clarity only the polymer backbone is shown (without the 2-methoxy- and 5-(2'-ethyl-hexyloxy)- groups and hydrogen atoms): polymer chains (hexamers) anchored via **A** acrylic acid and **B** 'monomer acid'. Color code: Carbon = black spheres, Oxygen = red spheres, Titanium = silver spheres, Excitons = red and blue double circle. **A**, excitons can travel along the conjugated polymer backbone towards the titania surface. **B**, to reach the titania surface excitons must travel by hopping between polymer chains.

Therefore, it is likely that the reduction in series resistance in acrylic acid **3** devices is the result of the grown polymer chains directing photogenerated charges towards the titania surface via the more favorable transport along the conjugated polymer backbone.[149,150] For polymer chains not lying directly on the TiO_2 surface in the case of the 'monomer acid' **4** functionalized devices, photogenerated charges would have to hop across different polymer chains to reach the titania surface, resulting in much slower charge transport and higher recombination rates,[151] and therefore explaining both the higher series resistance and the lower short circuit currents. The surprising results with the different linker molecules show that for an efficient photovoltaic device high light absorbance is not sufficient, and that the titania-polymer interface is crucial for charge separation and transport.

3.5 Conclusion

We have demonstrated the direct synthetic incorporation of MEH-PPV into mesoporous titanium dioxide films with more than a micron thickness. As the synthesis route we chose the Gilch-route because it is an inexpensive, non-toxic polymerization initiated with an alkoxide base and by increasing the temperature.[122] The MEH-PPV polymerization within the titania structure was directed at reactive sites on the titania surface introduced via either acrylic acid or a 'monomer acid' functionalization. The surface functionalization turned out to be essential for the incorporation of a large amount of the MEH-PPV into the titanium dioxide pores; it enhanced the amount of incorporated polymer up to nearly 6 times. Additionally, in case of a smaller pore system (10 nm) the conjugation length - manifested in the E_g values - of the in-situ synthesized MEH-PPV could be enhanced compared to non-functionalized samples. The performance of hybrid systems made with these two different anchor molecules in photovoltaic devices suggests that the orientation of

the polymer chains with respect to the titania surface is essential for efficient power generation. This shows that it is not only important to fill the porous host with a maximum amount of polymer, but that it is also important to tailor the nature of the linkage between the polymer and the titania which has a high impact on the electronic properties. On the one hand, the successful incorporation of a conjugated polymer into a porous metal oxide scaffold is therefore dependent on the functionalization of the surface with active linker molecules. On the other hand this alone is not sufficient to exploit the full electronic potential of the conjugated polymer in the resulting hybrid composite. Apparently, the surface anchoring geometry via the linker molecules is also very important, where a near-perpendicular orientation of the polymer chains with respect to the oxide surface seems to be advantageous. We anticipate that these insights into the electronic interactions between MEH-PPV and titania scaffolds depending on the polymer anchoring will help to develop new synthesis methods for more efficient hybrid materials.

Chapter 4

A Highly-Ordered 3D Covalent Fullerene Framework

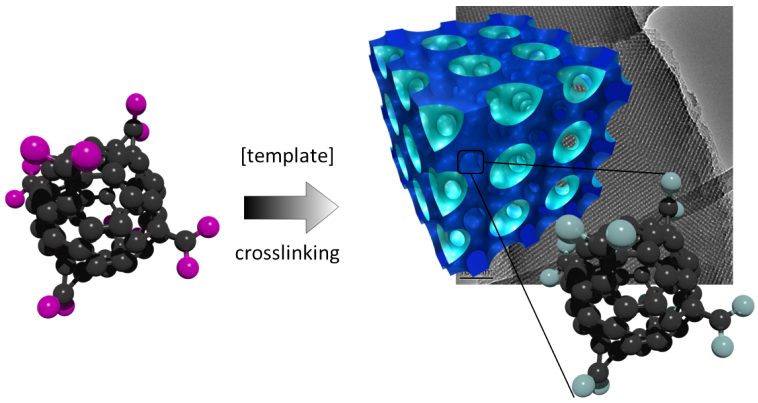

This chapter is based on the following manuscript of the article:

"A Highly-Ordered 3D Covalent Fullerene Framework"

Norma K. Minar, Kun Hou, Christian Westermeier, Markus Döblinger, Jörg Schuster, Fabian Hanusch, Bert Nickel, Geoffrey A. Ozin, Thomas Bein,

submitted to *Angewandte Chemie*, November 2014.

4.1 Abstract

A highly-ordered 3D covalent fullerene framework is presented with a structure based on octahedrally functionalized fullerene building-blocks in which every single fullerene is separated from the next by six functional groups. The fullerene building-blocks co-assemble with a liquid-crystalline block co-polymer to produce a covalent fullerene framework with orthorhombic *Fmmm* symmetry and 7.5 nm pores, confirmed by gas-adsorption, NMR spectroscopy, small-angle X-ray scattering (SAXS) and transmission electron microscopy (TEM).

4.2 Introduction

An entirely new branch of chemistry opened up after the discovery of the fascinating family of fullerenes in 1985 and the access to C_{60} on a preparative scale in 1990.[152,153] The structural uniqueness of the C_{60} molecule sparked the interest of materials scientists to use it as a building block for novel materials with intriguing properties.[154] Versatile two-dimensional and three-dimensional exohedral modification options (i.e. a modification outside the spherical molecule) stem from the multifunctionality of the fullerenes, thus making them attractive precursors for macromolecular and supramolecular chemistry.[154,155] Fullerene polymers are being developed to integrate the intriguing properties of C_{60} molecules with the good processability and excellent mechanical stability of polymers.[156]

The most straight-forward approach to obtain a polymer using solely C_{60} molecules is photopolymerization. The resulting fullerene polymer is non-soluble, stable and highly cross-linked, but it is disordered and no control over the resulting structure is possible.[157] More sophisticated strategies polymerize the C_{60} or functionalized fullerene derivates with the addition of auxiliary monomers to incorporate the

fullerene core into a polymer chain.[158,159] By using this method, however, only a few weight percent of fullerene functionalities can be introduced into the polymer chain.[160] In a different approach a star-block polymer with C_{60} core was designed to self-assemble into different thin film structures ranging from lamellar to gyroidal, but without any intermolecular connection.[161] Other researchers have cross-linked a surfactant-like fullerene derivative that resulted in a 2D structure.[162] An alternative approach with metal-coordinated connections in between the fullerene derivates produced 2D-layered structures with very small pores.[163]

Despite the synthetic effort in the field of fullerene polymers and other fullerene based materials, to our knowledge no examples exist of covalently cross-linked fullerene materials with three-dimensional order and stable high porosity. The introduction of ordered porosity is expected to create additional desirable features such as high surface area and molecular discrimination that would be beneficial for catalytic applications or electronic interactions of the fullerene pore wall material with molecular guests.[164]

Here we demonstrate the first example of a stable covalent fullerene framework exhibiting a highly-periodic 3D pore system with around 7.5 nm pore diameter. This high porosity was achieved by developing an evaporation induced self-assembly strategy of a fullerene precursor templated by a liquid-crystalline block co-polymer inducing high periodicity and porosity. In this context, fullerene molecules can be modified at many points on their surface, potentially resulting in a multitude of adducts with different symmetries and a varying number of functionalities. This would lead to a complicated co-assembly behavior between the precursor and template, and likely to produce limited order in the final product.

Here, we surmised that a C_{60} hexakis-derivative with T_h symmetry would be beneficial for the construction of a well-defined highly-ordered three-dimensional porous

framework. The resulting covalent fullerene framework could show extraordinary thermal stability and interesting electrical properties.

4.3 Experimental

Chemicals

Fullerene (C_{60}) was purchased from BUCKY USA (99.5 % grade). 9,10 - Dimethylanthracene (DMA, >98 %) was obtained from Tokyo Chemical Industry. Platinum-divinyltetramethyldisiloxane complex (Karstedt catalyst, 3-3.5 % Pt in vinyl terminated polydimethylsiloxane) was acquired from ABCR GMBH& CO.KG. All other chemicals and solvents were purchased from SIGMA-ALDRICH and used without further purification.

Methods

Small angle X-ray diffraction measurements were performed on a BRUKER D8 Discover with Ni-filtered CuK_α radiation (0.154 nm) and a position-sensitive detector (LynxEye). TEM images were acquired with a FEI Titan 80–300 microscope equipped with a field emission gun operated at 300 kV. The fullerene framework material was removed from the glass substrate and deposited on a carbon-coated copper grid for imaging. The SEM images were recorded with a JEOL 6500F field emission scanning electron microscope at 3 to 5 kV. Nitrogen sorption isotherms were measured with a QUANTACHROME Nova 4000e instrument at −196 °C. Prior to the measurements, all samples were degassed at 120 °C for 5 h. Brunauer Emmett Teller (BET) surface areas were calculated from the linear section of the BET plot (p/p_0 = 0.05–0.2). The pore-size distribution and pore volume were determined using a quenched solid state density functional theory (QSDFT) method (DFT kernel used:

N_2 at −196 °C on carbon, cylindrical and spherical pores for the adsorption branch). For liquid NMR characterization of the observed signal multiplicities the following abbreviations were used: s (singlet), d (doublet), t (triplet) and m (multiplet). ^{29}Si magic-angle spinning-(MAS) and ^{13}C cross polarization(CP)-MAS-NMR spectra were recorded on a Bruker Avance III 500 spectrometer (11.7 T, at 99.4 MHz for ^{29}Si and 125.8 MHz for ^{13}C), using a sample spinning frequency of 10 kHz. The UV-Vis absorption spectrum of the precursor solution and the fullerene framework film coated on a quartz slide was recorded with a Hitachi U-3501 spectrometer in transmission. The infrared measurements were carried out in transmission with a Bruker-Equinox 55 spectrometer, with the precursor or removed film material pressed into a pellet with potassium bromide. Thermogravimetric (TG) measurements were performed in a stream of synthetic air or nitrogen (25 mL min^{-1}) on a Netzsch STA 440 C TG/DSC. The measurements were carried out with a heating rate of 10 K min^{-1} and a temperature range from 30 °C to 900 °C. The capacitance was measured with a N4L PSM 1700 PsimetriQ frequency response analyzer with an LCR active head. For frequencies above 100 kHz a shunt resistor of 100 Ω was chosen. The data were evaluated with the PSMcomm software, version 1.3.1.211.

Precursor Synthesis and Characterization

Diallyl Malonate 1

The diallyl malonate **1** was synthesized according literature.[165] Malonic acid (1.0 g, 10 mmol), allyl alcohol (3.0 mL, 44 mmol) and p-toluenesulfonic acid (0.11 g, 0.64 mmol) were dissolved in 50 mL benzene. The water resulting from the esterification reaction was removed azeotropically using a Dean-Stark apparatus. After 6 h the apparatus was cooled down to ambient temperature. 50 mL diethyl ether was added to the reaction solution and the organic phase was washed with aqueous satu-

rated $NaHCO_3$ (2×15 mL), brine (1×15 mL) and dried over $NaSO_4$. After removing the solvent under reduced pressure a yellow oil remained. This crude product was purified by flash chromatography on a silica column (60Å, 0.035–0.070 mm) with ethyl acetate/hexane (1:10), to obtain the pure product as light yellow oil (1.7 g, 92% yield).

Diallyl Malonate Siloxane 2

The diallyl malonate siloxane 2 was synthesized according literature.[166] 0.78 g of **1** (4.2 mmol) was dissolved in THF (5 mL) in nitrogen atmosphere. To this solution triethoxysilane (2.3 mL, 12 mmol) and Karstedt catalyst (20 µL, 0.15–0.18 M) was added. The mixture was stirred for 12 h at room temperature and in nitrogen atmosphere. Subsequently the solvent and the excess triethoxysilane were evaporated under vacuum to give compound **2**.

^{1}H NMR (270 MHz, $CDCl_3$, TMS): δ = 4.08 (t, J=8 Hz, 4H), 3.79 (t, J=8 Hz, 12H), 3.32 (s, 2H), 1.72 (m, J=8 Hz, 4H), 1.18 (t, J=5.4 Hz, 18H), 0.59 (t, J=8 Hz, 4H).

^{13}C NMR (270 MHz, $CDCl_3$, TMS): δ = 166.67(C=O), 67.53, 58.46, 41.60, 22.13, 18.30, 7.13.

MS (EI, positive ion, m/z) $[M\text{-}OC_2H_5]^+$ calculated for $C_{19}H_{39}O_9Si_2$, 467.21 , found 467.3.

Hexaadduct $C_{66}(COOC_3H_6SiO_3Et_3)_{12}$ 3

The synthesis of precursor **3** was carried out via a modified route after Camps et al..[167] Fullerene C_{60} (0.20 g, 0.28 mmol) and 9,10 - dimethylanthracene (DMA, 0.572 g, 2.8 mmol) were solved in 120 mL toluene and stirred at room temperature under nitrogen and exclusion of light for 3 h. After the addition of tetrabromomethane (9.2 g, 28 mmol) and compound **2** (1.4 g, 2.8 mmol) the mixture was

stirred for 1 h and then 1,8-Diazabicycloundec-7-ene (DBU, 0.83 mL, 5.5 mmol) was added. The reaction solution was stirred at room temperature and under nitrogen for 4 days. The precipitate of the reaction was separated by centrifugation. The purification of **3** was achieved by flash chromatography on a silica column (60A, 0.035-0.070 mm) using first anhydrous dichloromethane and then dichloromethane/ethanol (20:1) followed by dichloromethane/ethanol (10:1) as the eluent solutions. The C_{60} silane precursor **3** was obtained as a red solid at a yield of 40% (80 mg). Compound **3** was stored in dry dichloromethane solution under argon for further use. The molecular structure of **3** was determined by combining ^{13}C, ^{29}Si NMR and IR data. Unambiguous evidence for the formation of the precursor compound **3** was provided by ^{13}C NMR spectroscopy (figure 4.2). The only two resonances observed for the fullerene core located at 145.84 and 141.12 ppm indicate a T_h-symmetric addition pattern surrounding the fullerene core.[168,169] A signal for the bridgehead C atom (δ =45.3 ppm), a signal for the carbonyl group (δ = 163.7 ppm), and three signals for the $(CH_2)_3$ linker (δ =6.38, 22.06, 68.89 ppm) were also observed (figure 4.2).

^{1}H NMR (270 MHz, $CDCl_3$, TMS): δ = 4.19 (t, COOC**H**$_2$CH$_2$CH$_2$, 24H), 3.77 (m, OC**H**$_2$CH$_3$, 72H), 1.79 (m, CH$_2$C**H**$_2$CH$_2$, 24H), 1.18 (t, OCH$_2$C**H**$_3$, 108H), 0.61(m, CH$_2$CH$_2$C**H**$_2$Si, 24H).

^{13}C NMR (270 MHz, $CDCl_3$, TMS): δ =163.71 (C=O), 145.84, 141.12 (C_{60}, sp^2), 68.89 (C_{60}, sp^3), 68.78 (COOCH$_2$**C**H$_2$CH$_2$,) 58.80 (O**C**H$_2$CH$_3$), 45.27 (O=C**C**C=O), 22.06 (CH$_2$**C**H$_2$CH$_2$Si), 18.43 (OCH$_2$**C**H$_3$), 6.38 (CH$_2$CH$_2$**C**H$_2$Si).

^{29}Si NMR (270 MHz, $CDCl_3$, TMS): δ = -45.77.

IR (KBr): ν(cm^{-1}) = 2975, 2926, 2890 (ν_{C-H}), 1748 ($\nu_{C=O}$), 1444, 1391, 1230 (ν_{C-O-C}), 1103, 1078 (ν_{Si-O-C}), 954 ($\nu_{asym\,Si-O-C}$), 784.

C_{60}-Framework Synthesis

In a typical synthesis, 12 mg of Pluronic® F127 (0.95 μmol) was dissolved in 200 μl of ethanol followed by addition of 6 μL of 0.2 M HCl to form a surfactant solution. To this solution, 18.9 mg of precursor **3** $C_{60}R_6$ (5 μmol) in 200 μl ethanol solution was added and the mixture was stirred at room temperature for 3 h. The aged solution was used to spin-coat glass and ITO substrates at various speeds from 500 to 1000 rpm. This way, brown, homogeneous and smooth films were obtained. Bulk thick films were obtained by casting the coating solution into a petri dish and aging in ambient air for 5 days. To remove the surfactant, the cast films were solvent extracted four times with ethanol at 70°C. For each cycle of extraction, the material was left in EtOH for 10 h. Before solvent extraction, the material was thermally treated at 100 °C in air for 18 h to stabilize the framework before template removal. Bulk material was extracted in the same way, but the material was removed from the glass substrates beforehand.

4.4 Results and Discussion

4.4.1 From Molecular Fullerene to 3D Covalent Fullerene Framework

The building block for the fullerene framework – a hexakis-functionalized fullerene – was synthesized by applying the template-directed activation method developed by Hirsch et al.[167] (see figure 4.1). We successfully synthesized and purified the resulting hexakis-adduct with a T_h - symmetrical octahedral addition pattern. The ^{13}C-NMR spectrum of the product proves this high symmetry and purity of the precursor (see figure 4.2).

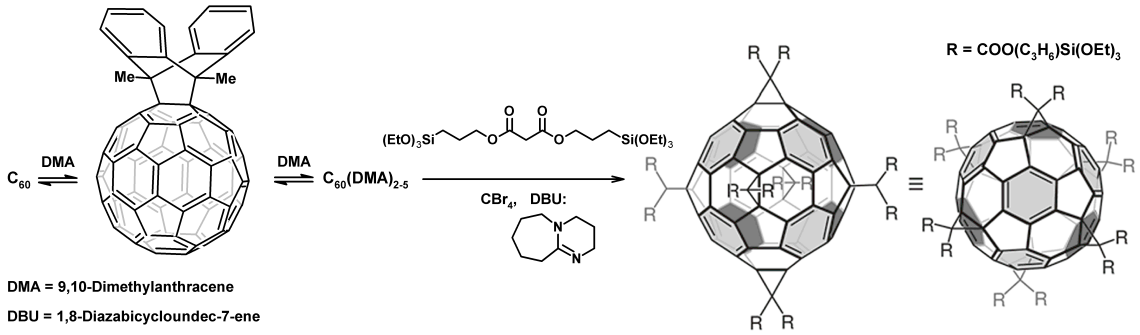

Figure 4.1: Synthesis of the hexakis-functionalized fullerene by DMA-templating and further cyclopropanation with silane malonates.

Thin films of the fullerene framework were produced in an EISA process by spin coating an ethanol solution of the hexakis-functionalized fullerene and a block copolymer as template onto different substrates, such as glass or transparent conductive oxides. The so formed films proved to have a highly ordered mesostructure as demonstrated by means of small angle X-ray diffraction, as shown in figure 4.3.

For the as-synthesized film, a narrow reflection with a full width at half maximum (FWHM) value of 0.05° 2θ was observed at 0.85° 2θ, indicating a highly ordered structure with a *d*-spacing of 10.4 nm along the film normal. After a heat treatment

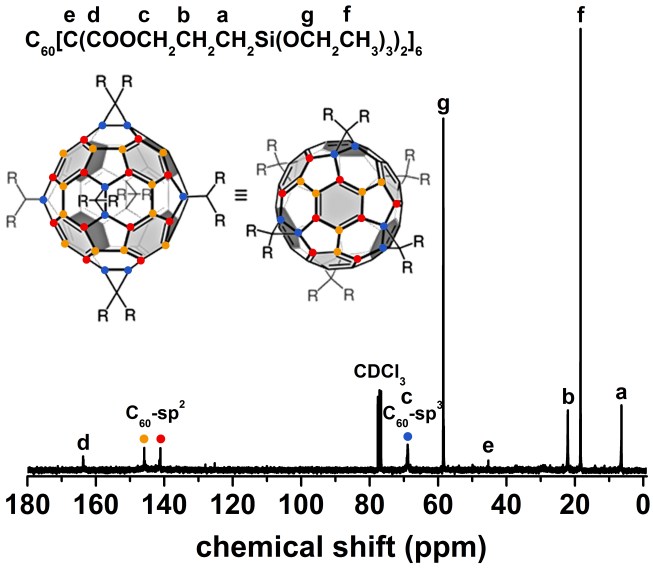

Figure 4.2: ^{13}C-NMR of the isolated hexakis-functionalized fullerene **3**. All signals can be assigned to carbon atoms of **3**. The 3 different chemical environments resulting from a symmetrical octahedral addition pattern at the C_{60} core are marked with a color code in the spectra and on the molecule scheme. R = $COO(C_3H_6)Si(OEt)_3$.

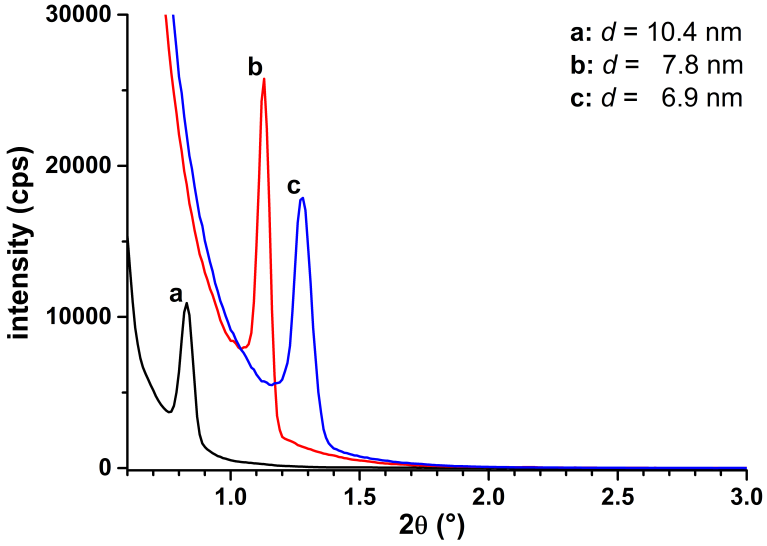

Figure 4.3: SAXS pattern of thin films of a highly ordered fullerene framework. a: as synthesized, b: after 18 h at 100 °C and solvent extraction, c: after 18 h at 100 °C, solvent extraction and 1 h in nitrogen atmosphere at 300 °C.

at 100 °C and template extraction with ethanol, the *d*-spacing decreased to 7.8 nm. Likewise, after a second thermal treatment at 300 °C for 1 h under nitrogen atmosphere, the *d*-value decreased further to 6.9 nm. This is in good agreement with the typically reported uniaxial shrinkage of mesoporous thin films along the substrate normal.[170,171]

Figure 4.4 shows TEM micrographs of fullerene framework films after thermal treatment at 300 °C recorded in cross section and plan view, i.e. along and perpendicular to the substrate normal, respectively. The cross section shows *d*-values of 11.0 nm parallel to the film and 6.8 nm along the film normal, which is in good agreement with the values determined by SAXS. Plan view images show mutually rotated periodic domains extending over large areas in the µm range. The domains show a rectangular lattice with *d*-values of 11.0 nm and 7.9 nm. The ratio of these values (1.39) and the *d*-value along the film normal of 10.4 nm before further treatments indicate an initially cubic structure with space group $Im\bar{3}m$ and [011] orientation along the substrate normal. Assuming a lattice constant of 15.7 nm, the observed *d*-values viewed along [011] of such a structure are $d_{(0-11)}$ = 11.1 nm and $d_{(200)}$ = 7.9 nm, which fits well with our TEM observations. Along the film normal, the slight deviation of the value expected for $d_{(011)}$ (10.4 nm instead of 11.1 nm) observed after film synthesis can be explained by a slight uniaxial shrinkage during drying. As a result of the shrinkage after heat treatment, the structure becomes orthorhombic, with space group *Fmmm* and lattice basis vectors $a_{orh} = a_{cub}$, $b_{orh} = (b_{cub}+c_{cub})*S$, and $c_{orh} = c_{cub}-b_{cub}$, where *S* is the shrinkage factor. In the orthorhombic setting, the indexing of the observed lattice planes changes as follows: $(0\bar{1}1)_{cub}$ becomes $(002)_{orh}$ and $(011)_{cub}$ becomes $(020)_{orh}$. The relationship of the initial cubic structure and the orthorhombic structure is depicted in figure 4.5. Films possessing the same space groups and orientations with respect to the substrate exist for carbon

and metal oxides.[172–174] The symmetry change of cubic films with $Im\bar{3}m$ symmetry in [011] orientation along the film normal to orthorhombic $Fmmm$ in [010] orientation is discussed in detail by Falcaro et al..[170]

The local chemical structure of the fullerene framework was examined by solid-state NMR spectroscopy of ^{13}C and ^{29}Si nuclei, respectively (see figure 4.6). The ^{13}C cross polarization (CP)-magic-angle spinning (MAS) - NMR of the film removed from the substrate corresponds very well with that of the precursor, which confirms the integrity of the molecular structure of the precursor in the fullerene framework (compare figures 4.2 and 4.6 A). The signals at δ = 8.7 and 22.0 ppm can be assigned to the CH_2 groups connected directly to and next to the silicon atom (figure 4.6 A, label a, b). These signals correspond to the ^{13}C signals at δ = 6.38 and 22.1 ppm of the fullerene precursor molecule (see figure 4.2). The slight shift of the signal of the carbon atoms adjacent to the Si atoms is due to the hydrolysis of the ethoxy groups (followed by condensation) which changes the chemical environment of the silicon atom. The signal at 46.1 ppm is assigned to the malonate carbon atoms anchored on the fullerene core (figure 4.6 A, label e), which is in good agreement with the corresponding signal in the precursor. The signal at 69.6 ppm is a result of the overlapping signals of the sp^3 hybridized carbon of the C_{60} and the carbon atoms of the propyl chain connected to the carbonyl via oxygen, and matches also with the corresponding signal in the precursor (figure 4.2, label c, δ = 68.9 ppm). The broad signal centered at around 143 ppm can be unambiguously assigned to the sp^2 fullerene core, while the signal at 162.8 ppm is assigned to the carbonyl (C=O) group of the ester (figure 4.6 A, label d). The ^{13}C-CP-MAS-NMR also proves that the ester group in the precursor is robust enough to survive the synthesis conditions. In the solid state ^{29}Si MAS-NMR spectrum (figure 4.6 B), res-

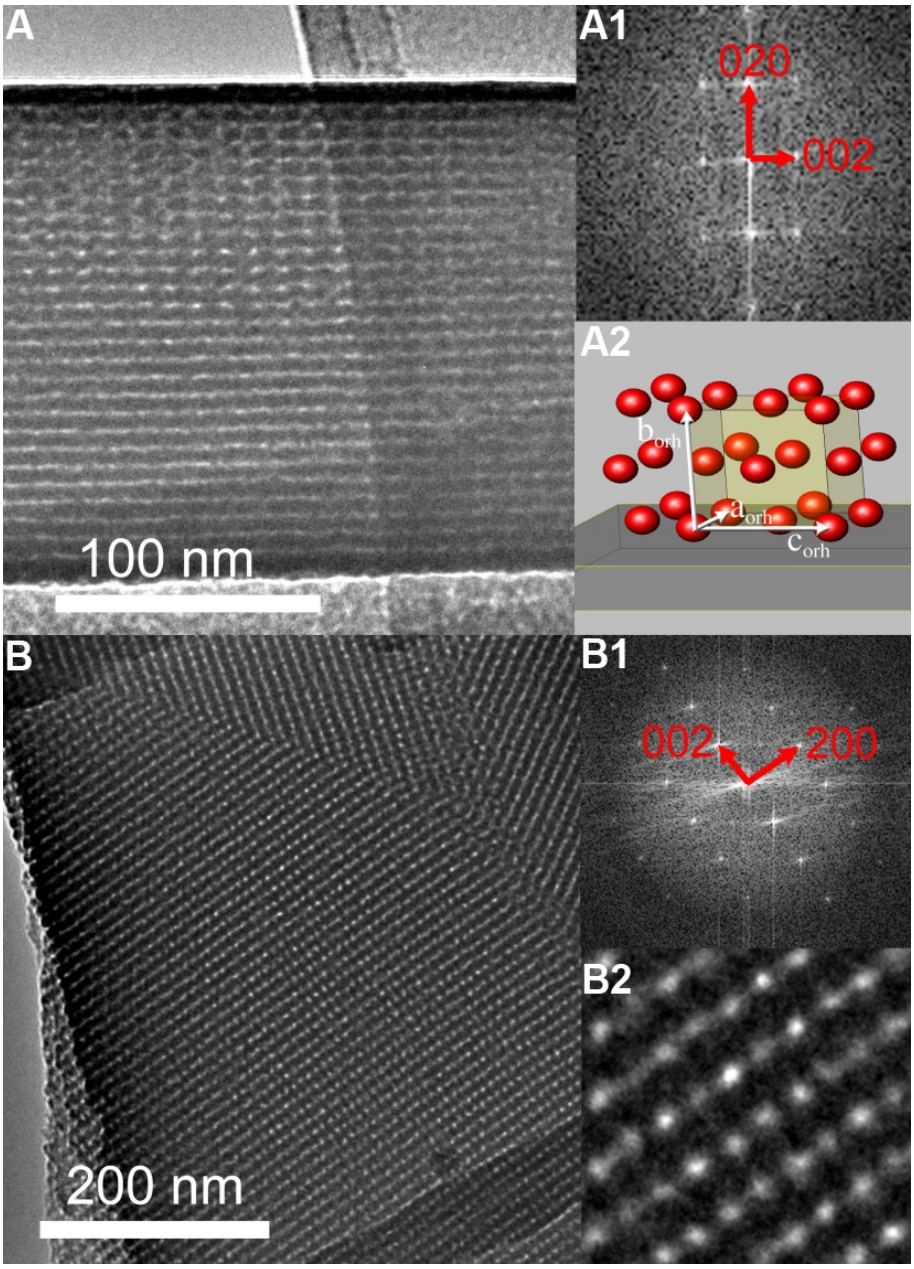

Figure 4.4: TEM images of fullerene framework film (190 nm thick) thermally treated at 300 °C under N_2 for 1 h. **A** Cross section image, viewed along [100] of the orthorhombic structure with *Fmmm* symmetry. The lattice planes parallel and perpendicular to the substrate with measured distances of 6.9 and 11 nm can be indexed as (020) and (002), respectively. **A1**: 2D Fourier transform of the TEM image **A**. **A2**: Scheme of the orientational relationship of the orthorhombic structure and the substrate, also viewed along [100]. **B**: Plan view image in [010] orientation, showing large highly ordered domains. The *d*-values 11 nm and 7.9 nm are in good agreement with the lattice plane distances of (002) and (200), respectively. **B1**: 2D Fourier transform of the largest domain of **B**. **B2**: Blow-up (5×) of the TEM image **B** on the left side.

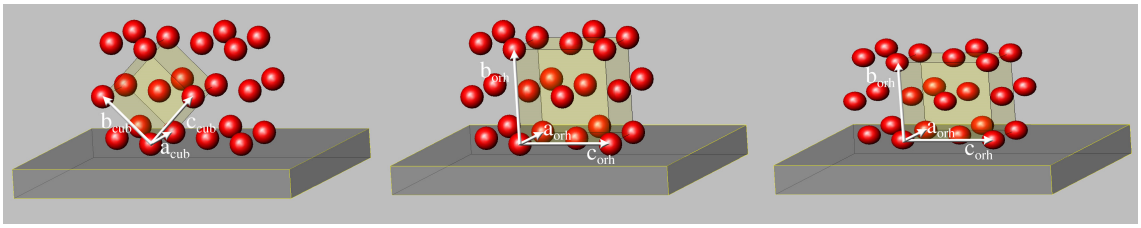

Figure 4.5: Schematic picture of the relationship of the mesoporous structure in the cubic and the orthorhombic setting with respect to the substrate surface. On the left side, the initial cubic $Im\bar{3}m$ structure is depicted, with $[011]_{cub}$ along the substrate normal. The image in the middle shows the initial structure described in an orthorhombic setting with *Fmmm* symmetry and $[010]_{orh}$ along the substrate normal. The lattice basis vectors change as follows: $a_{orh} = a_{cub}$, $b_{orh} = (b_{cub}+c_{cub})$, and $c_{orh} = c_{cub}-b_{cub}$. On the right side the structure is shown after shrinkage: a_{orh} and c_{orh} remain constant, while b_{orh} is decreased.

onances at −49.3, −58.2 and −67.7 ppm are representative of T-type organosilica species [T_n = $RSi(OSi)_n(OH)_{3-n}$], which can be assigned to T_1, T_2, T_3 units of the condensed silsesquioxane moieties, respectively. The clear absence of Q units [Q_n =$Si(OSi)_n(OH)_{4-n}$] at around −100 ppm shows that there is negligible hydrolytic Si-C bond cleavage and that the siloxane-bridged organic linkers are maintained intact in the fullerene framework under the synthetic conditions. Additionally, the siloxane network of the fullerene framework shows a higher degree of condensation upon calcination. The ^{29}Si MAS-NMR spectrum in figure 4.6 C proves that the Si-C bond cleavage is negligible after the 300 °C thermal treatment because very little new intensity is detected in the chemical shift range around −100 ppm for Si-Q-species.

Thermogravimetric measurements give additional evidence that the fullerene network and especially the molecular structure are stable in nitrogen up to 300 °C (see figure 4.7).

The accessible porous structure of the fullerene framework after template removal by solvent extraction was examined by nitrogen sorption of the film material. As shown in figure 4.8, the isotherm shows a typical Type IV shape, commonly observed with mesoporous materials. The hysteresis indicates a structure with large, cage-like

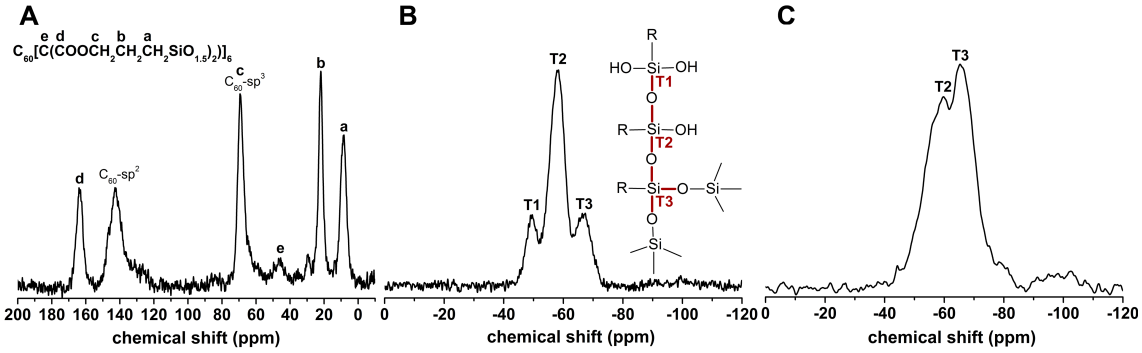

Figure 4.6: ssNMR of the fullerene framework. **A**, ^{13}C CP-MAS-ssNMR of solvent extracted fullerene framework. **B**, ^{29}Si MAS-ssNMR of solvent extracted fullerene framework. **C**, ^{29}Si MAS-ssNMR of solvent extracted fullerene framework heated at 300 °C in N_2.

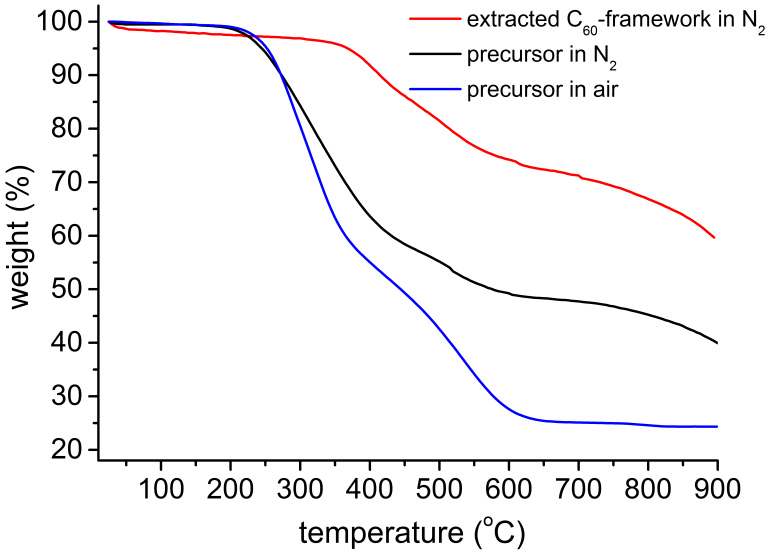

Figure 4.7: Thermogravimetric curves of precursor molecule and solvent extracted fullerene framework film material under nitrogen or air.

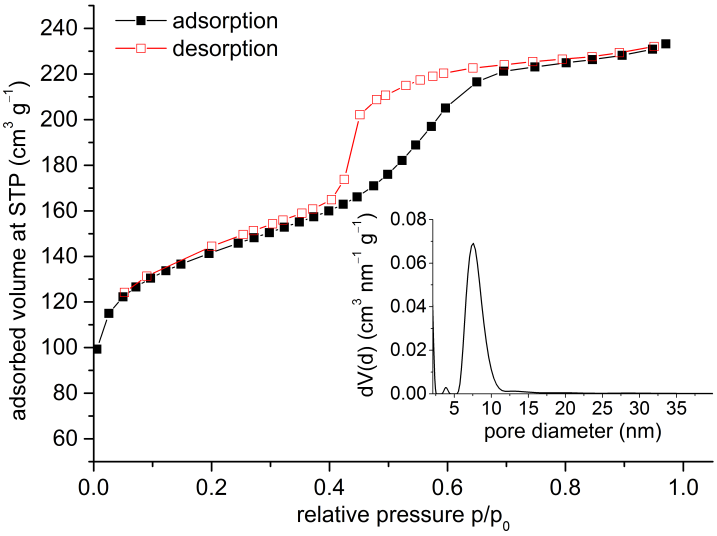

Figure 4.8: Nitrogen physisorption isotherms of the template extracted fullerene framework. The inset shows the fitted pore size distribution.

pores that is typical for cubic mesostructures.[173] The estimated pore-size distribution shows a sharp maximum at 7.5 nm. The material shows a BET (Brunauer-Emmett-Teller) specific surface area of 494 m^2 g^{-1} and a total pore volume of 0.34 m^3 g^{-1} . We note that the internal voids of the fullerene moieties are not detected by the nitrogen adsorption measurements. Moreover, in the high pressure end of the isotherm we observe a complete lack of textural porosity, which speaks well of its highly ordered uniform, almost single crystal quality. Also, in the low pressure end no discontinuity between adsorption and desorption branches is visible, implying quite a rigid open framework with essentially no swelling and shrinking, respectively.

4.4.2 Electronic Properties

In contrast to the unfunctionalized fullerene the hexakis-functionalized fullerene shows nearly no light absorption above 300 nm (figure 4.9).[175] This can be explained

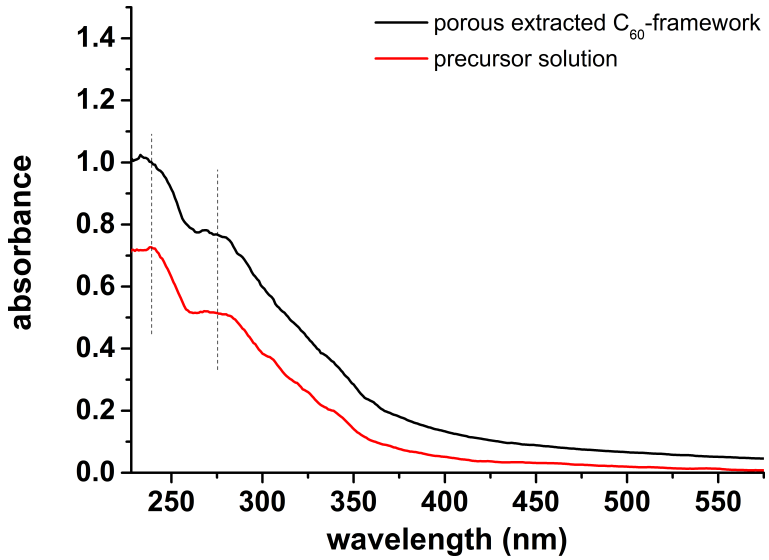

Figure 4.9: UV-Vis spectra of a fullerene framework film on fused silica substrate and the corresponding precursor **3** in acetonitrile solution (10^{-4} M). The absorption maxima of the fullerene framework film show no bathochromic shift compared to the molecule in solution. Therefore no electronic coupling or aggregation occurs in the fullerene network.

by the attenuation of the conjugated fullerene π-electron chromophore by virtue of transforming six double bonds into cyclopropane moieties.[176] The UV-Vis spectrum of the fullerene framework film resembles that of the precursor solution, with maxima at 238 nm and 275 nm (figure 4.9). The absence of any shift for the porous structure indicates that the single fullerene precursor molecules are very well dispersed in the framework without electronic coupling and aggregation, similar to the situation in solution. The absence of aggregation can be explained by the molecular structure of the precursor with T_h symmetry, where the six malonate molecules are added to the fullerene cage in an octahedral pattern. This allows the fullerene molecules to be fully and omni-directionally separated and thus, electronic coupling can be avoided. To probe the influence of the C_{60} side groups on electronic mobility, field-effect transistors with bottom gate and top contact configuration were fabricated. The trans-conductance characteristics of the mono-adduct, the hexakis-adduct without silane groups and the final fullerene framework after template extraction are shown

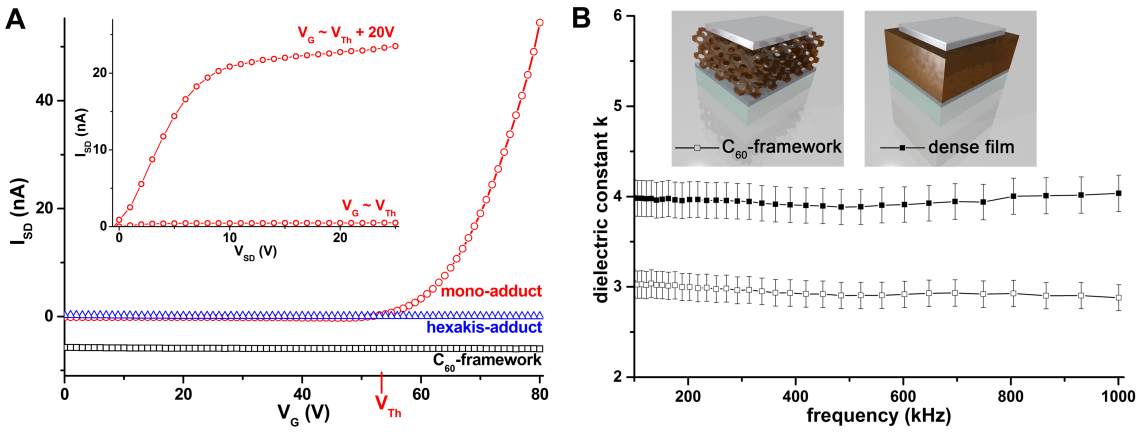

Figure 4.10: Characterization of the electronic properties by field effect mobility and impedance measurements. **A**, field effect measurements of three different samples in thin-film transistor geometry. The main graph shows trans-conductance curves of a mono-adduct (circles), a hexakis-adduct without silane groups (triangles) and an extracted fullerene framework film (squares) at a source-drain voltage of 20 V. Only the mono-adduct shows measurable currents. The threshold voltage V_{Th} refers to the mono-adduct. The data of the fullerene framework are shifted by −6 nA for clarity. The inset shows the conductance curves of the mono-adduct based device. The lower and the upper curves refer to a gate voltage close to V_{Th} and about 20 V above V_{Th}, respectively. **B**, dielectric constant values over a broad frequency range obtained by impedance measurements on sandwich-type devices (cf. inset). By introducing mesoporosity, the dielectric constant for the extracted fullerene framework (empty squares) is lowered by one compared to a dense hexakis-adduct film (filled squares).

in figure 4.10 A. During sweeps of the gate voltage constant source-drain voltage V_{SD} = 20 V, the two hexakis-adduct films do not show any significant current, whereas the mono-adduct device shows the characteristic signature of an n-type semiconductor. An electron mobility of the order of 10^{-4} cm^2 Vs^{-1} was observed for the mono-adduct. The conductance curves (figure 4.10 A, inset) for two constant values of the gate voltage, one close to the threshold voltage (V_{Th}) and the second value 20 V above, show n-type characteristics including saturation of the mono-adduct transistor, while no current was observed for both hexakis-adduct films.

In conclusion, the measurements show that the modification of C_{60} with six side chains causes the electron mobility to decrease drastically. Compared to the electron mobility of C_{60}, which is at the order of 1–2.5 cm^2 Vs^{-1} [177,178], the value for the mono-adduct is already decreased by four orders of magnitude. This observation

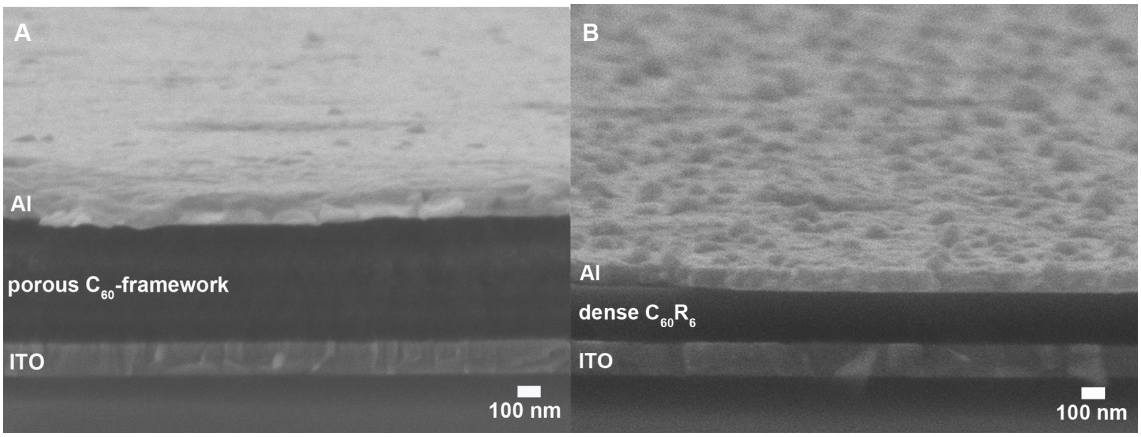

Figure 4.11: SEM cross section images of sandwich-type devices for impedance measurements. **A**, device with porous fullerene framework film. **B**, device with dense film of hydrolyzed precursor. All layers are labeled within the images.

is consistent with previous studies of mobilities in fullerene derivatives, which show that the mobility decreases with increasing distance between the fullerenes.[179,180] The electronic properties of a material are not only defined by its electron mobility, which characterizes the velocity of electrons inside the material in response to an electric field, but also by the dielectric constant k, which relates to the polarizability of the material. The impedance measurements were performed on sandwich-type devices containing dense films of the hydrolyzed precursor and porous films of the extracted fullerene framework, respectively. The film thicknesses were determined from SEM cross section images, which show homogeneous thin films of the respective material (see figure 4.11).

Impedance measurements of dense films of the hydrolyzed precursor give k-values of around 4 (figure 4.10 B). In contrast to this, theoretical studies predict that with a network of fullerene cores connected by various linkers ultra-low k-values, even below 2, can be achieved.[181,182] The structure of the linking side chains used we used is more complex than the ones used for the calculations, which were shorter and sometimes only alkyl chains. We assume that the higher content of C-O and Si-O bonds present in our precursor yields a higher polarizability and therefore a higher

dielectric constant.[183,184] For example, the structure includes twelve siloxane groups per fullerene core, which is two times more than assumed in the study by Hermann et al..[185] By introducing significant porosity by means of structure-directing micellar surfactant aggregates in the EISA method, the dielectric constant can be reduced to a low-k value of around 3 (figure 4.10 B). This is consistent with other studies where the dielectric constant was decreased by introducing or increasing porosity into a film material.[186–188] The capacitance measurements from 100 kHz to 1 MHz show a nearly constant behavior for both dense and porous film samples.

4.5 Conclusion

We have demonstrated the synthesis of a new hexakis C_{60} adduct with octahedral symmetry, which was employed as a building block to create the first example of a highly-ordered three-dimensional covalent fullerene framework. Thin films of this material were synthesized via block co-polymer, template-directed, evaporation-induced self-assembly, resulting in a periodic orthorhombic structure with *Fmmm* symmetry, that, after template removal, revealed a pore size of around 7.5 nm. Due to the functionalization of the fullerene the resulting material has greatly differing electronic properties compared to pristine C_{60}. The dielectric constant of the porous fullerene framework was decreased relative to the dense analogue showing values of around 3 and 4, respectively, over a wide frequency range.

It is envisioned that covalent fullerene frameworks of the type described in this paper will provide access to a wide range of hybrid materials having chemically tailored pore walls and encapsulated guests with tunable chemical and physical properties.

Chapter 5

An Electronically Active PMO with a Donor-Acceptor Unit

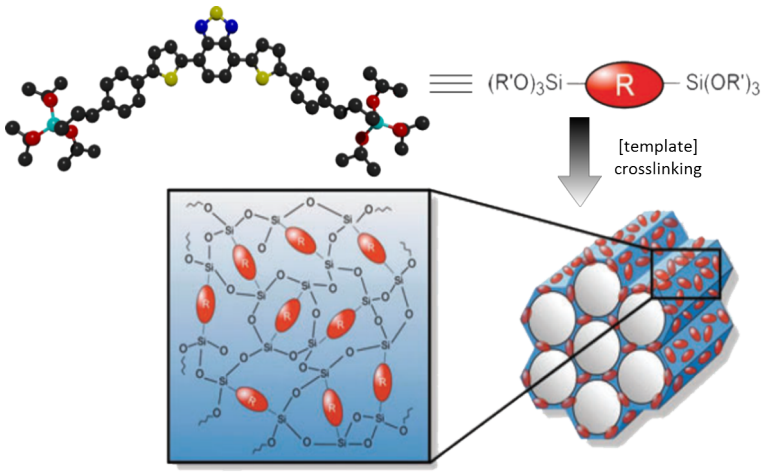

This chapter is based on the manuscript of the article:

"An Electronically Active PMO with a Donor-Acceptor Unit"

Norma K. Minar, Florian Auras, Yan Li, Shinji Inagaki, Thomas Bein,

in preparation.

5.1 Abstract

A novel opto-electronic periodic mesoporous organosilica (PMO) based on a donor-acceptor-donor unit (dithienyl-benzothiadiazole (DTBT)) has been developed. A lamellar structure was build with the DTBT-bridged silsesquioxane precursor using an evaporation-induced self-assembly process with a triblock co-polymer as soft template. An approximately hexagonal arrangement of the pores was achieved by HCl-TEOS vapor infiltration, thus obtaining a stable structure. The resulting mesoporous organosilica shows no shrinkage upon heat treatment and template removal and exhibits a very large d spacing of 14.5 nm demonstrated by small-angle X-ray scattering. N_2 sorption experiments reveal a high porosity with pore sizes ranging from 7 to 11 nm and a total pore volume of 0.16 mL g^{-1}. The π-interactions between the DTBT moieties in the PMO walls were investigated by wide-angle X-ray scattering, UV-Vis and photoluminescene (PL) spectroscopy. The formation of the porous structure and the hydrolysis/condensation of the DTBT precursor disturb the intermolecular interactions as illustrated by the blue-shifted UV-Vis absorbance and a vanished long-lived PL signal compared to pristine films of non-hydrolyzed DTBT precursor. Thin films of the PMO materials were integrated into photovoltaic devices with [6,6]-phenyl C61 butyric acid methyl ester acting as electron acceptor. The photovoltaic performance of dense films of pure hydrolyzed DTBT precursor is higher compared to porous structured DTBT films, which can be explained by the introduction of insulating silica during the structure formation.

5.2 Introduction

In 1999 the new materials class of periodic mesoporous organosilicas (PMOs) was discovered nearly simultaneously by the research groups of Inagaki, Stein and Ozin.[37–39] PMO materials can introduce numerous functionalities at high concentration into porous silica networks through organically bridged silsesquioxane precursors. PMOs combine the high porosity, stability and tuneability of inorganic silica networks with the great diversity of organic functional moieties. In addition to classical applications of porous materials such as catalysis, gas storage or chromatography, new functionalities that can lead to different applications such as photo-activity or new electronic properties were introduced.[34,35]

Only recently some of us developed a new photo-active PMO constructed from a large porphyrin-bridged silsesquioxane.[45]

Moreover, Mizoshita et al. reported a moderate hole conductivity for a new PMO based on phenylene-vinylene precursor molecules.[46]

An organic building block, well-known for its favorable π-stacking tendency is the 4,7-dithienyl-2,1,3-benzothiadiazole unit (DTBT).[189] Due to the inherent donor-acceptor-donor structure the DTBT molecule shows a low band-gap and thus absorbs light throughout the visible range.[190,191] It may be anticipated that a PMO material based on this DTBT moiety could combine good light-harvesting properties with high charge carrier mobility and good conductivity. Earlier in 2014, Inagaki and coworkers could prove this assumption by synthesizing disordered mesoporous thin films based on the same DTBT precursor and applied these as p-type active layer in photovoltaic devices.[47] The porous structure of the only 60 nm thick films features large pores ranging from 15–20 nm and shows no long-range order. Only a modified precursor with additional siloxane groups led to a more defined porous

structure. However, this molecular modification decreased the hole mobility of the resulting porous structure and therefore a lowered photovoltaic performance was observed.[47]

Here we establish the formation of a surfactant-templated periodic mesoporous material using the DTBT-bridged silsesquioxane precursor. To form and stabilize the ordered porous structure, we employed a combined HCl and tetraethyl orthosilicate (TEOS) vapor infusion treatment.[31] We examine the electronic interactions between the DTBT moieties within the PMO walls and reveal the influence of the structural evolution on the opto-electronic properties of this system in photovoltaic devices.

5.3 Experimental

General

The precursor 4,7-Bis(5-(4-(3-(tri-isopropoxysilyl)propyl))phenyl)thiophene-2-yl)-2,1,3-benzothiadiazole ("DTBT precursor") was synthesized by the group of S. Inagaki. The synthesis conditions are detailed elsewhere.[47] A Suzuki-Miyaura cross-coupling between 2-bromo-5-[4-[3-[tris(1-methylethoxy)silyl]propyl]phenyl]-thiophene and 2,1,3-benzothiadiazole-4,7-diboronic acid bis(pinacol) ester followed by purification with silica gel chromatography afforded the DTBT precursor in pure form.[47]

Poly(3,4-ethylenedioxythiophene)-poly(styrenesulfonate) (PEDOT:PSS) was purchased from Sigma-Aldrich as an aqueous solution (3.0–4.0 wt%, high-conductive grade).

Phenyl-C61-butyric acid methyl ester (PCBM, 99.5%)was purchased from Solenne BV.

Poly (9,9-bis(3'-(N,N-dimethylamino)propyl)-2,7-fluorene)-alt-2,7-(9,9-dioctylfluorene) (PFN) was purchased from Solaris Chem Inc..

All other chemicals were purchased from SIGMA-ALDRICH and used without further purification.

Methods

One-dimensional small angle X-ray diffraction measurements were performed on a BRUKER D8 Discover with Ni-filtered CuK_α radiation (0.154 nm) and a position-sensitive detector (LynxEye). UV-Vis spectra were measured with a PERKIN-ELMER Lambda 1050 UV-Vis/NIR spectrometer equipped with a 150 mm integrating sphere. Absorbance spectra were recorded in transmission geometry with the corresponding substrate material (fused silica, glass) as reference. The infra-red (IR) absorption spectra of films were recorded with a Nicolet iN10 from THERMOSCIENTIFIC in reflection mode. An atmospheric correction was performed by the Omnic Picta software (v1 SP4). Nitrogen sorption isotherms were measured with a QUANTACHROME Autosorb-1 instrument at −196 °C. Prior to the measurements, all samples were vacuum-degassed at 120 °C for 5 h. Brunauer Emmett Teller (BET) surface areas were calculated from the linear section of the BET plot ($p/p_0 = 0.05$–0.2). The pore-size distribution and pore volume were determined using a quenched solid-state density functional theory (QSDFT) method (DFT kernel used: N_2 at −196 °C on carbon, cylindrical and spherical pores for the adsorption branch). TEM images were acquired with a FEI Titan 80–300 microscope equipped with a field emission gun operated at 80 kV. The PMO materials were removed from the glass substrate and deposited on a copper grid for imaging. Differential pulsed voltammetry (DPV) was performed in argon atmosphere with a METHROM Autolab PGSTAT30N potentiostat, using platinum wires as the working and counter electrode and a saturated Ag/AgCl reference electrode (SIGMA ALDRICH, 0,197 V vs. SHE). The measurements were performed with a scan rate of 5 $mV\,s^{-1}$, a step size

of 2.5 mV, a modulation amplitude of 5 mV, a modulation time of 50 ms and an interval time of 0.50 s. For the DPV measurements, 0.76 mg DTBT-precursor was dissolved in 5 mL anhydrous toluene. A solution of 310 mg tetrabutylammonium hexafluorophosphate ($TBAPF_6$) and 0.148 mg ferrocene in anhydrous acetonitrile (3 mL) was added and the measurement was carried out immediately immediately after mixing. The concentrations of the components in the final solution result in 0.1 mM for the DTBT-precursor, 0.1 M for $TBAPF_6$ and 0.1 mM for ferrocene. Photoluminescence (PL) measurements of the precursor solutions were carried out using a PHOTON TECHNOLOGY INTERNATIONAL QuantaMaster 40. The PL spectra of the quenching experiments (PCBM blend) were recorded with a home-built setup consisting of a HORIBA iHR320 spectrometer equipped with a photomultiplier tube and a liquid N_2-cooled InGaAs detector. A 455 nm LED modulated at 83 Hz was used as excitation source and the PL signal was detected via a Signal Recovery 7230 lock-in amplifier. The system was calibrated for spectral response with a calibrated light source. Steady-state and time resolved PL measurements of samples before and after the HCl-TEOS vapor treatments were performed with a Fluotime 300 Spectrofluorometer (PICOQUANT GMBH). The excitation wavelength was fixed at 508 nm. The emission in time-resolved measurements was monitored at the maximum intensity of the steady-state photo emission. J-V curves were recorded with a KEITHLEY 2400 sourcemeter under illumination with simulated solar radiation obtained from an AM1.5G solar simulator (SOLAR LIGHT Model 16S) at 100 $mW\,cm^{-2}$. The light intensity was calibrated with a FRAUNHOFER ISE certified silicon reference cell equipped with a KG5 filter.

Film Synthesis

The DTBT precursor (3.75 mg, 3.6 μmol) and the template Pluronic® F127 (3.75 mg, 0.29 μmol) were dissolved in tetrahydrofuran (450 μL) in a 1 mL seal-able glass vessel. After the addition of mesitylene (3.47 μL, 0.025 μmol) the solution was stirred at 4 °C for 2 h. HCl (4 μL, 0.1 M, 0.4 μmol) was added and the solution was stirred for another hour at 4 °C. The aged solution was spin-cast(1000–2000 rpm, 20–40 μL) on different substrates such as glass, fused silica and fluorine-doped tin oxide (FTO) to synthesize thin films. Bulk material for sorption studies was synthesized by drop casting the aged solution onto glass substrates.

The vapor treatment with tetraethyl orthosilicate (TEOS) and HCl (5 M) was conducted in a closed 100 mL glass vessel for 2 h at 60 °C. The amount of TEOS and HCl was kept constant at 0.5 mL each, and placed in two separate containers in the glass vessel together with the vertically positioned dried precursor-template films. After this treatment the films were further stabilized by heating at 120 °C for 2 h. Films stabilized through the vapor and heat treatments were extracted in ethanol under reflux for 40 h. The ethanol was exchanged twice. Supercritical CO_2 extraction was performed in a 100 mL autoclave at 85 bar and 40 °C for 2 h with stabilized (vapor treatment and 120 °C) films.

Photovoltaic Devices

For the preparation of photovoltaic devices thin films of the precursor and the block co-polymer Pluronic® F127 were spin cast (2000 rpm, 28 μL) on fluorine-doped tin oxide coated glass substrates. Beforehand a thin layer of PEDOT:PSS serving as hole-transport material was applied to the FTO substrates by spin coating (3.0–4.0 wt% aqueous solution, 60 μL/2.25 cm^2, 3000 rpm, 20 s) and subsequent heating

to 150 °C for 15 min. After drying at room temperature for 5 days the films were vapor-treated and stabilized by heating as mentioned above and extracted with supercritical CO_2. The extracted PMO films were dried under vacuum (10^{-2} mbar) for 3 h. The electron acceptor PCBM (20 mg mL^{-1} in chlorobenzene) was spin-coated (50 µL/2.25 cm^2, 800 rpm, 45 s) after 20 seconds soaking time and under argon atmosphere. On top of the dried PCBM-coated films, a layer of the electron-blocking material PFN was applied by spin coating (1000 rpm, 50 µL/2.25 cm^2) under ambient conditions. The PFN solution was prepared by dissolving 0.86 mg of PFN in 430 µL dry methanol and 2.2 µL acetic acid. On top of this layer 100 nm of aluminum was applied by thermal evaporation. After the assembly, the samples were stored and measured under argon.

5.4 Results and Discussion

5.4.1 Structure Characterization of the DTBT-PMO

Several attempts with different structure directing agents (e.g. Pluronic® P123, F108) were conducted to produce a mesoporous structure. Selected results will be briefly reported here. The combination of mesitylene as swelling agent[192] with the block co-polymer F127 as template and ageing at low temperatures (4 °C) resulted in structured films exhibiting reflections in small-angle X-ray scattering measurements (SAXS, figure 5.1) at around 0.84 (d = 10.5 nm) and 1.60° 2θ (d = 5.5 nm). The ratio of the d-values amounts to 2 : 1 and can be an indication of a lamellar structure.[193] The reflection at 3.56° 2θ originates from the molecular structure unit of the precursor molecule and is also detected for pure precursor material.[194]

This initial structure was not stable towards solvent extraction and it was not possible to stabilize it with ammonia vapor treatment or heating at elevated temperatures.

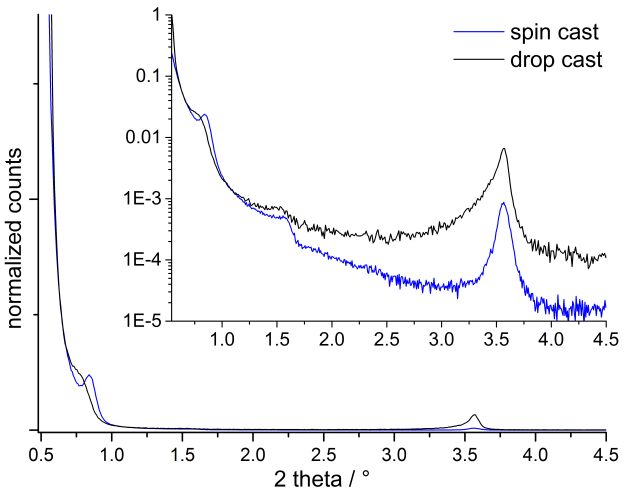

Figure 5.1: SAXS patterns of spin- and drop-cast films with F127 template after synthesis. The inset shows the reflections with logarithmically scaled intensity.

After a vapor treatment with hydrochloric or formic acid the material withstood the solvent extraction with ethanol, but no reflections indicating a periodic order could be observed in the corresponding SAXS patterns. A stable periodic structure, however, was successfully synthesized by applying a vapor treatment with HCl and tetraethyl orthotitanate (TEOS) at 60 °C for 2 h. SAXS measurements after the treatment reveal a periodic structure that is stable towards heating at 120 °C and solvent extraction (see figure 5.2 A) showing a reflection at 0.61° 2θ corresponding to a large *d*-spacing of 14.5 nm. It is remarkable that the structure is not prone to any shrinkage and that it inherits the same *d*-value obtained after synthesis even after solvent extraction. The SAXS pattern of a thin film of this material after template removal reveals several reflections at 0.61°, 1.05° and around 1.75° 2θ (figure 5.2 B). The relative ratios of the corresponding *d*-values account to approximately 1 :$\sqrt{3}$: 3, which is an indication for a hexagonal structure.[17,195] Taking into account earlier studies about the infiltration of TEOS vapor into thin structured template films, the SAXS patterns in figure 5.2 B indicate a transformation from a lamellar to a

hexagonal nanostructure.[31–33] The swelling of the *d*-value from 10.5 to 14.5 nm and of the film thickness from 100 to 200 nm support this hypothesis.[31]

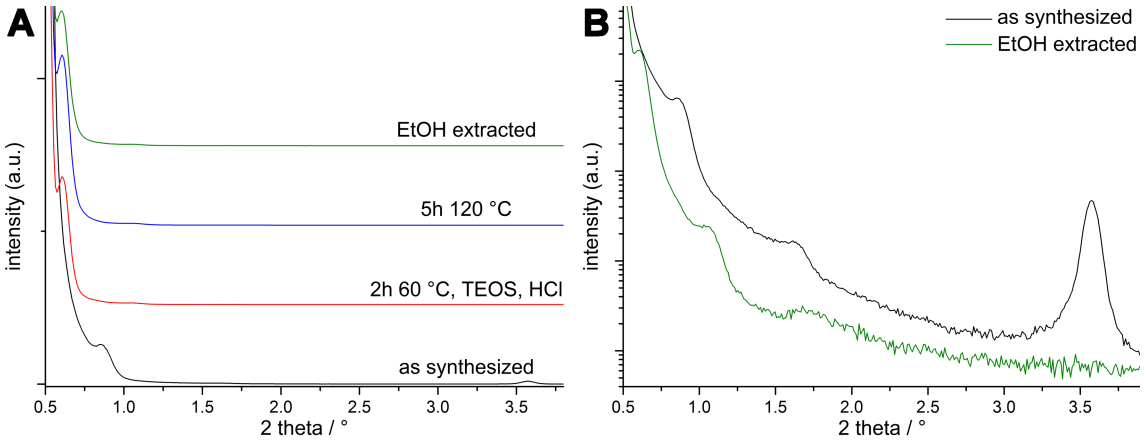

Figure 5.2: A: SAXS patterns of the structured material after different treatments. The structure is stabilized by the HCl-TEOS vapor treatment and no shrinkage can be detected after heating at 120 °C and subsequent solvent extraction. B: Comparison of the SAXS patterns after synthesis and after template removal with a logarithmic scaling of scattering intensity.

Different temperatures, duration times and amounts of HCl and TEOS for the vapor treatment were examined and best results were obtained for 60 °C, 2 h and 0.5 mL of TEOS and HCl (5 M). Another parameter exhibiting a strong influence on the evolution of the periodic structure is the total drying time of the film material after casting onto the substrate. The optimal time was found to be 4 to 5 days after film synthesis on account of the corresponding SAXS pattern in figure 5.3, which shows the highest signal to noise ratio and therefore the best periodicity of the structure.

The template removal from the PMO material was monitored by IR spectroscopy. For comparison a spectrum of the precursor hydrolyzed with HCl without any additives was recorded as well (see figure 5.4).

Signals corresponding to the template F127 can only be found in the spectrum of the non-extracted PMO film after the vapor treatment: A sharp peak at 2972 cm^{-1} for the stretching mode of the methyl groups of the iso-propyl moieties as well as several signals between 1300 and 1200 cm^{-1} are visible and can be attributed to

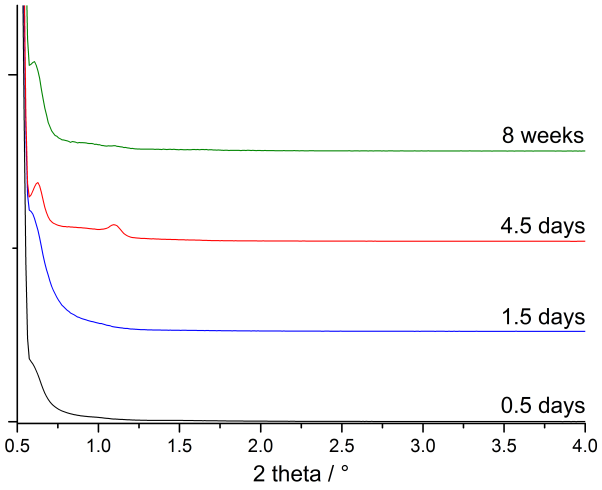

Figure 5.3: SAXS patterns of thin PMO films after identical TEOS-HCl vapor treatments, but different drying times, stacked along the y-axis.

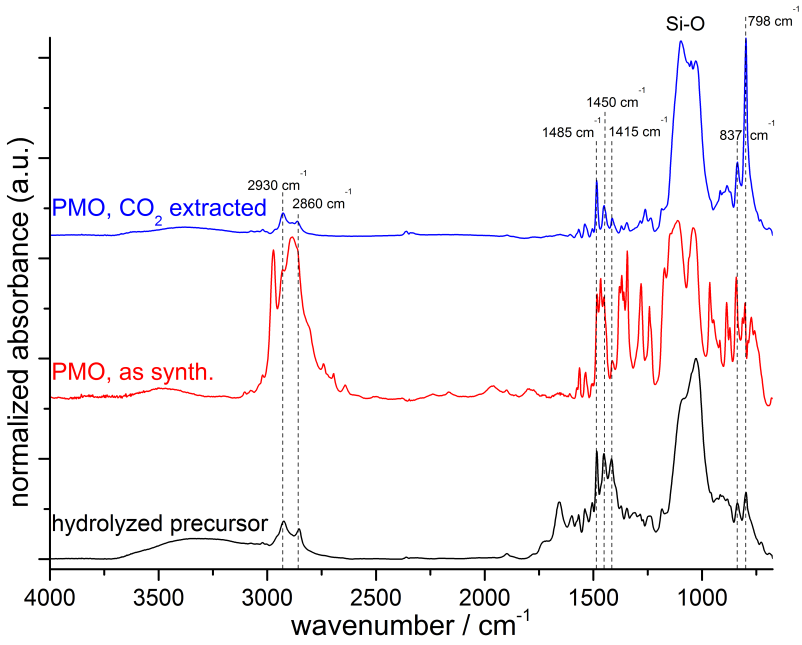

Figure 5.4: IR spectra of the hydrolyzed precursor (black), the structured organosilica with F127 template (red) and the porous structure after CO_2 extraction (blue). Signals assigned to the DTBT precursor are marked with dashed lines.

the block co-polymer F127.[196] Characteristic peaks of the hydrolyzed DTBT precursor at 2930 cm^{-1} and 2860 cm^{-1} originate from the stretching vibration of CH_2 groups.[196] Stretching vibrations of the thiophene rings in the DTBT precursor cause the signals at 1485 cm^{-1} and 1450 cm^{-1}.[197] Moreover, the peak at 1415 cm^{-1} originates from an in-plane vibration of an aromatic carbon double-bond in the DTBT precursor molecule. The strong signals at 837 cm^{-1} and 798 cm^{-1} can be assigned to vibrations of the para-disubstituted phenyl-rings of the DTBT precursor.[196] The broad signals around 1080 cm^{-1} corresponding to the Si-O units are present in all three spectra as expected (see figure 5.4).

After supercritical CO_2 extraction only signals corresponding to the silica groups around 1100 cm^{-1} and from the precursor can be found (c.f. figure 5.4), which implies a complete removal of the template.

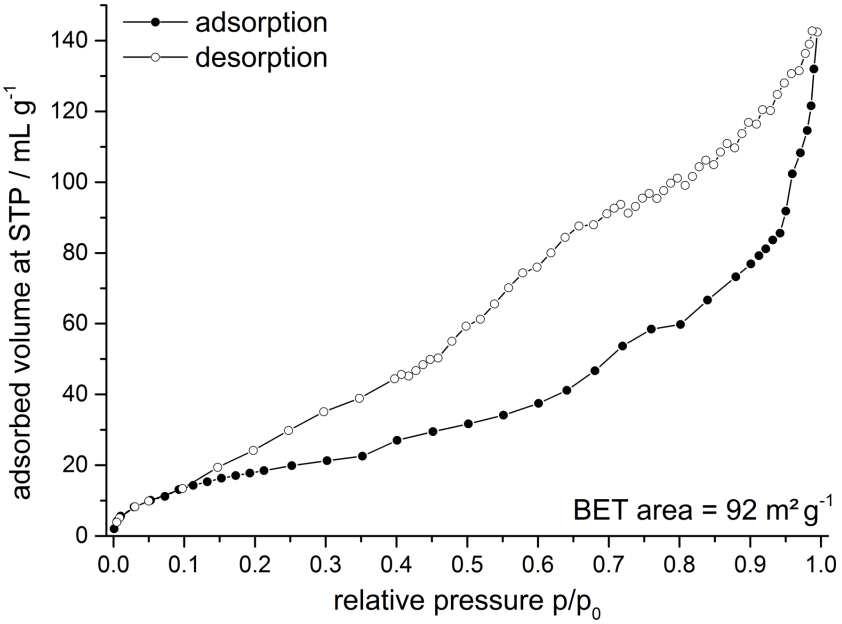

Figure 5.5: N_2 sorption isotherms at −196 °C of PMO material after CO_2 extraction.

Further information about the porous structure was collected through nitrogen sorption experiments. The sorption isotherm in figure 5.5 of the PMO after CO_2 extraction is a mixture of a type II and IV isotherm shape attributed to large mesopores

($\geq$ 10 nm). The pronounced hysteresis loop could be an indication for cage-like pores with small interconnections. The calculated BET surface area corresponds to 92 $m^2\,g^{-1}$. A reliable interpretation of the isotherm is difficult due to the not well defined shape. One reason for this could be an inhomogeneous material resulting from the bulk synthesis, which differs from the thin film synthesis in several points. Firstly, to obtained sufficient material for the physisorption experiment, thin film synthesis yielding only a few nanograms per film is not feasible. Therefore, large glass substrates were drop-coated with the synthesis solution. This way the drying time of the films is increased which is a key factor for the structure formation via the self-assembly of the template micelles and the DTBT precursor. Another parameter influencing the final porous structure is the vapor infiltration of HCl and TEOS. The diffusion path for the vapor species in drop-casted films is by an order of magnitude longer as for thin spin-coated films - several micrometers compared to less than 200 nm. The reduced periodicity in drop-casted films compared to spin-casted films can be seen by comparing the signal intensity in figure 5.1. Spin-coated films show a higher intensity of the structure related reflection (below 2° 2θ) compared to the SAXS reflection of drop-cast material.

Further information about the ordered porous structure of thin PMO films was obtained with transmission electron microscopy (TEM). The TEM micrographs in figure 5.6 A and B reveal a regular porous structure with approximately 10 nm wide channels arranged in small ordered domains with a worm like character. Figures 5.6 C and D show ordered domains of pores of 10 nm diameter that appear to be hexagonally arranged. This matches the conclusions from the ratio of the *d*-values extracted from previous SAXS pattern (figure 5.2). The wall thickness estimated from the TEM micrographs is around 10 nm.

The amount of infiltrated silica introduced through the HCl and TEOS vapor treat-

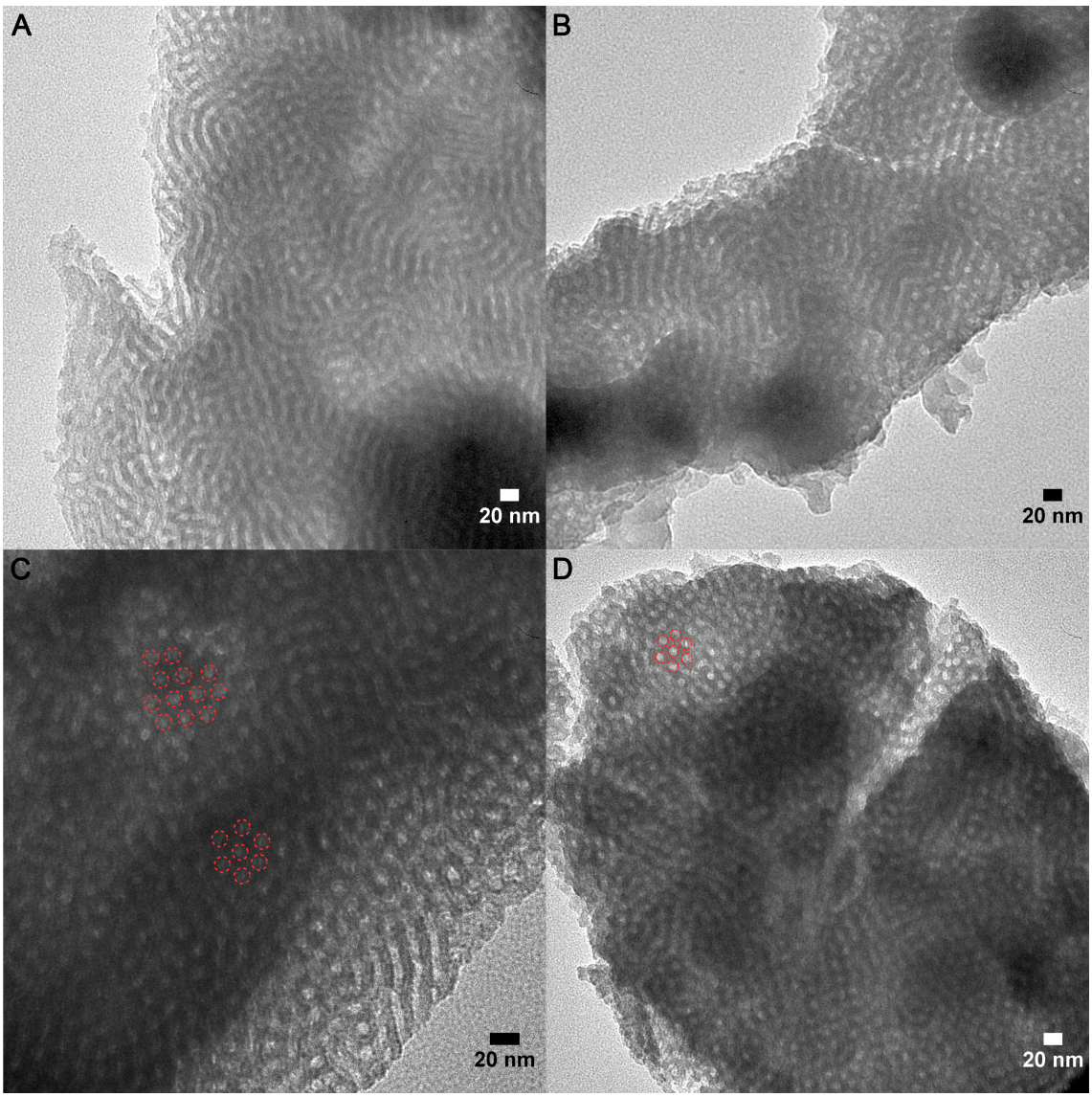

Figure 5.6: TEM micrographs (A-D) of removed film material after the HCl-TEOS treatment and supercritical CO_2 extraction. In figures C and D the outlines of some pores were marked to highlight the indication of a hexagonal structure.

ment was estimated from a thermogravimetric analysis of the porous bulk material after template removal (see figure 5.7). The organic DTBT unit decomposes in a broad range between 150 and 700 °C, associated with the weight loss $w_{organic}$ (equation 5.1). The calcined (char) yield ch_y of 45.3 wt% consists of SiO_2 from the infiltrated TEOS vapor and the silica moieties of DTBT precursor molecule (equation 5.2). Under the assumption that all silica groups from the DTBT precursor

and TEOS are fully hydrolyzed and condensed, the amount of infiltrated TEOS can be calculated via the combination of equation 5.1 and 5.2.

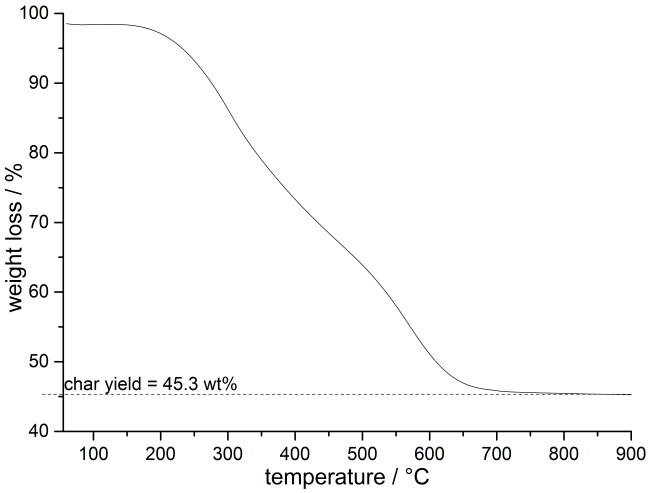

Figure 5.7: Thermogravimetric analysis of the CO_2 extracted PMO bulk material.

The variables x and y correspond to the molar fraction of the DTBT precursor and the infiltrated TEOS, respectively. The molar mass of the organic moiety amounts to $M(,C_{32}H_{26}N_2S_3,) = 534$ g mol^{-1}. The resulting calculated molar ratio of DTBT precursor to additionally introduced silica is 5.5 to 1. This corresponds to a total of 50 weight percent of the DTBT precursor in the final PMO material.

$$w_{organic} = M(\text{hydrolyzed precursor without } Si_2O_3) \cdot x \quad (5.1)$$

$$ch_y = M(SiO_2) \cdot (y + 2\,x) \quad (5.2)$$

5.4.2 Optoelectronic Properties

The molecular precursor for the DTBT-PMO was designed with a dithienyl benzothiadiazole (DTBT) unit accompanied by a phenyl moiety terminated with an isopropyl siloxane at each side. The combination of a benzothiadiazole unit with a

thiophene moiety on each side results in a donor-acceptor-donor structure.[189] The planarity of the DTBT precursor unit promotes the π-stacking[190] of the molecules and also their crystallization. Needle-shaped crystallites form readily from a drop-cast solution of the precursor in THF (see figure 5.8). So far it has not been possible to obtain high quality single crystals suitable for structure analysis. Nevertheless, the Bravais lattice could be determined as monoclinic P with the approximate elemental unit cell parameters $a = 1.79$ nm, $b = 0.94$ nm, $c = 3.14$ nm and $\beta = 94.7°$. The dimensions of the unit cell might suggest that one molecule of the precursor, which has a length of approximately 3.4 nm from silicon to silicon atom, is positioned along a spatial diagonal. The XRD pattern of a spin-coated film of the DTBT precursor shows a preferred orientation of the molecules because some signals disappeared compared to the pattern of the powder. We surmised that the electronic properties, for example the conductivity, of a PMO material built from this precursor could benefit from the stacking tendency through favorable intermolecular interactions.

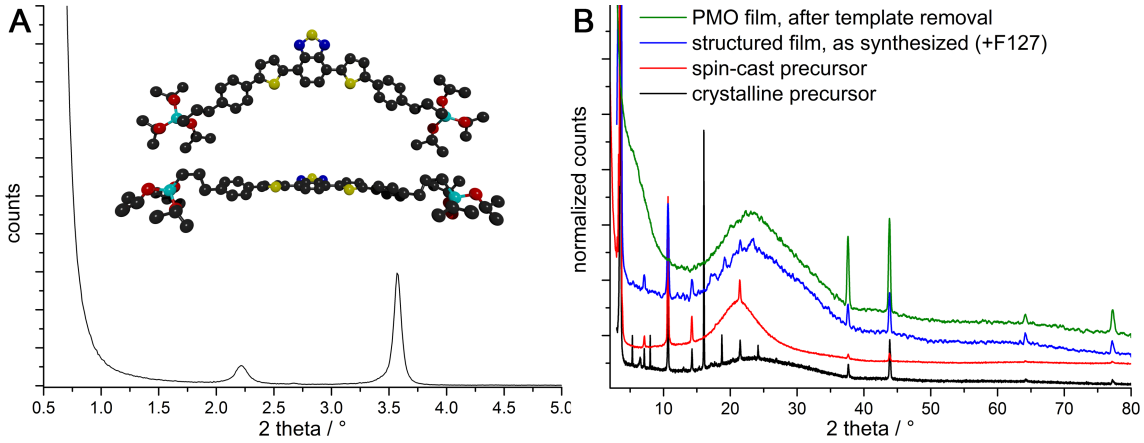

Figure 5.8: **A**: SAXS pattern of crystalline precursor. Inset: 3D model of the DTBT precursor molecule. Color code: Carbon = black, sulfur = yellow, nitrogen = royal blue, silicon = cyan, oxygen = red. Hydrogen atoms are not depicted for clarity. **B**: WAXS pattern of crystalline precursor (black), spin cast film of precursor in THF solution (red), structured film of precursor with template F127 (blue) and structured film of precursor and template after HCl-TEOS vapor treatment (green). The broad background between 15 and 45° 2θ originates from the amorphous glass substrate.

The crystalline precursor shows two reflections at very low angles (see figure 5.8 A). The signal at 2.24° 2θ is only present for the crystalline precursor. The corresponding *d*-value of 3.25 nm is close to the dimension of the molecule from silicon to silicon atom. The other small-angle reflection at 3.56° 2θ remains present until the hydrolysis of the film by the acidic vapor (compare figure 5.9).

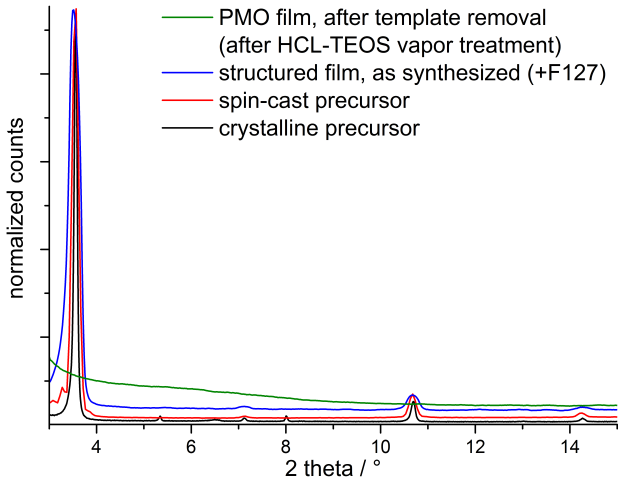

Figure 5.9: XRD patterns of the DTBT precursor material (black, red), DTBT/template films (blue) and the final PMO material (green) after template removal from 3 to 15° 2θ.

Taking into account the estimated dimensions of the precursor molecule and the XRD data (figure 5.9), we may speculate that the non-hydrolyzed molecules appear to build up an interdigitated molecular arrangement with strong π-π interaction of the planar D-A-D cores.[189] Interconnecting and condensing the network by the HCl-TEOS vapor treatment appears to compromise the high degree of crystallinity as there are no more reflections below 10° 2θ. The comparison of the WAXS patterns of the precursor and the final PMO film show a decreased crystallinity with a few reflections remaining above 35° 2θ in the final structured film.

The decrease in crystallinity and associated intermolecular π-π-interactions is also

confirmed by the UV-Vis spectra of structured films after synthesis and after the vapor treatment and template removal in figure 5.10 A. The optical absorption of only dried precursor-template films is strongly red-shifted compared to the precursor solution. The maxima in the visible light range ($\geq$ 400 nm) can be fitted to several peaks corresponding to different molecular aggregate or interaction species (see figure 5.10 B). The structured films before the vapor treatment inherit two main absorption maxima at 538 and 574 nm and one additional peak at 496 nm. After the HCl-TEOS vapor treatment the absorbance is decreased about one third and blue-shifted by about 50 nm. An analog blue-shift of the absorption maxima by 50 nm can be observed for non-structured DTBT precursor films which were only exposed to acidic vapor (HCl or formic acid). The main absorbance peak at 485 nm is even 15 nm blue-shifted compared to the absorbance maximum of the non-hydrolyzed precursor in solution (c.f. figure 5.11 B). This implies that the individual molecules interact less with each other in the structured solid PMO films as in the liquid solution. The vapor-infiltrated TEOS molecules and the silica-condensation might separate single DTBT units in a way that removes electronic interactions.

In a next step, the question of an interaction of the DTBT-PMO with possible electron donor materials was investigated. To address this point, the energy levels of the molecular DTBT precursor were estimated via differential pulsed voltammetry (DPV) and Tauc plot analysis of the precursor in solution. The first oxidation level of ferrocene at 4.8 eV below vacuum was used as an internal reference point. The shift of the first oxidation level of the precursor of around 0.6 V results in an estimated HOMO energy level of -5.43 eV (see figure 5.11 A).[198] The optical band gap was calculated from the linear onset in the Tauc plot in figure 5.11 B. With a band gap of 2.23 eV, the LUMO level energy is located around -3.20 eV. Comparing these values with literature values of the energy levels of PCBM of -5.63 and -3.75 eV[198]

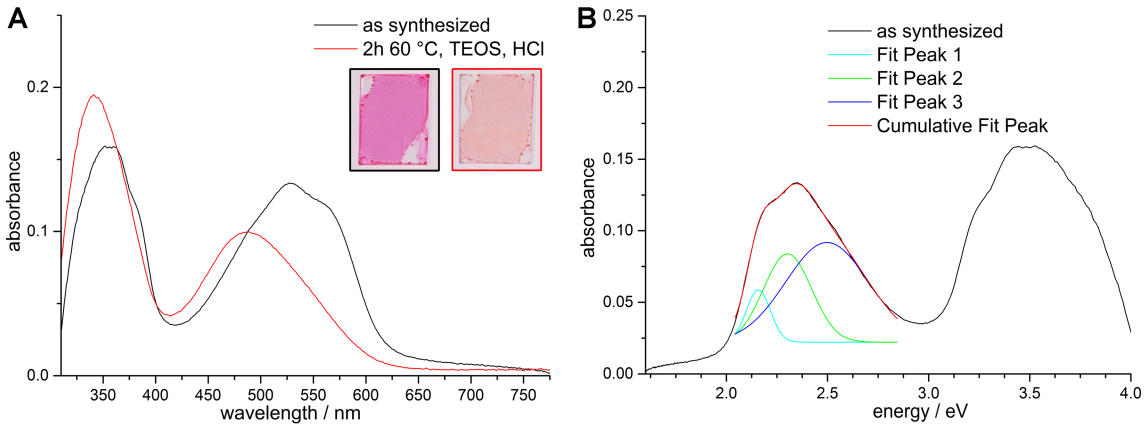

Figure 5.10: **A**, UV-Vis spectra of a DTBT/template dried film after spin coating (as synthesized, black) and after the HCl-TEOS vapor treatment (2 h, 60 °C, HCl, TEOS, red) and template removal. The insets show pictures of the corresponding films with colored frame according to the graphs. **B**, absorbance of a dried film after spin coating (before the HCl-TEOS treatment) plotted against the light energy and fitted with a Gauss function to reveal the peak positions of the absorption species.

suggests that efficient electron injection from the DTBT precursor toward PCBM could be established (compare figure 5.12).

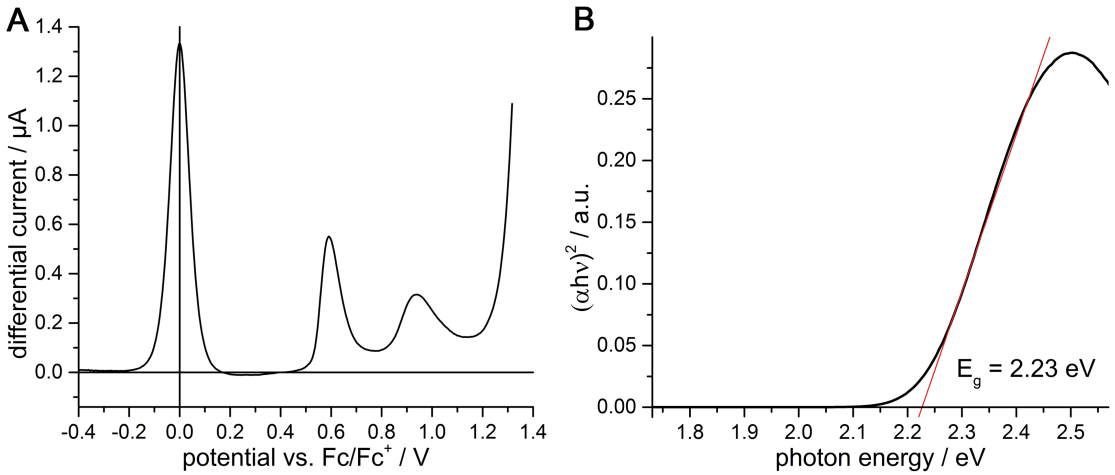

Figure 5.11: A: Differential pulsed voltammetry of the DTBT precursor molecule in solution. The reduction potential of the internal standard ferrocene is used as a reference signal (at 0 V). The first oxidation level, which corresponds to the HOMO level energy, of the DTBT precursor is shifted relative to ferrocene by about 0.6 V. B: Tauc plot of the DTBT precursor molecule in THF solution.

To test this hypothesis, the photoluminescence (PL) quenching in PCBM-DTBT-precursor blend films was investigated (see figure 5.13 A). Pure non-hydrolyzed

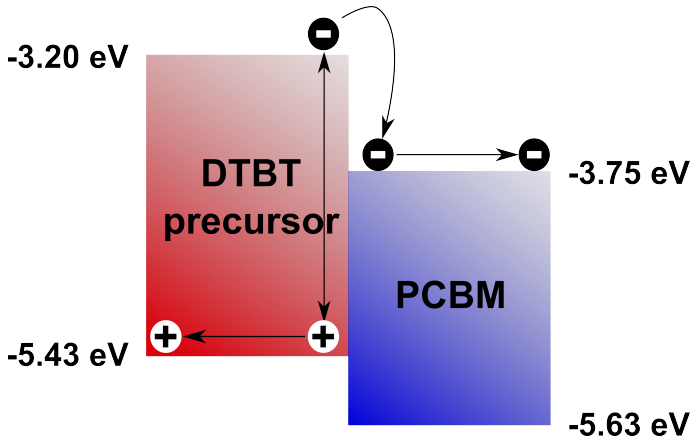

Figure 5.12: Schematic diagram of the position of the energy levels of the DTBT precursor in relation to the energy levels of PCBM. A possible electron transfer from DTBT to PCBM is shown.

precursor films excited at 530 nm show a broad luminescence ranging from about 625–700 nm. Contrary to this, pure PCBM films show nearly no photoluminescence at this excitation wavelength. The PL intensity of a blend of PCBM and DTBT precursor is decreased by about a factor of 3 (figure 5.13 A), suggesting an energy transfer from the DTBT precursor to the PCBM, as already expected from the HOMO-LUMO energy levels. The corresponding UV-Vis spectra of the same films imply that the blend films contain approximately the same amount of PCBM and DTBT precursor as the pure films, because the absorbance values at the excitation wavelength of 530 nm add up to the absorbance of the blend films. Therefore the reduced photoluminescence has to be the result of an active quenching by the presence of the electron acceptor PCBM and not of a simple reduction of the amount of the luminescent DTBT material.

Based on the promising results of the PL quenching experiments, the performance of the DTBT-based organosilica films were examined in photovoltaic devices with PCBM as acceptor material. In addition to PMO films, dense layers consisting of cross-linked hydrolyzed DTBT precursor molecules were also investigated. Different blocking layers were tested including molybdenum oxide, nickel oxide and

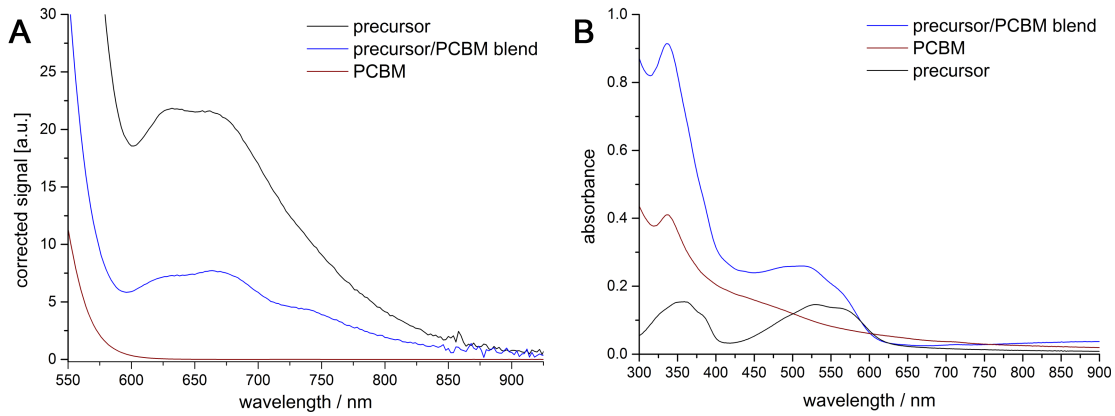

Figure 5.13: A: Photoluminescence spectra of films of PCBM, DTBT-precursor and a DTBT-precursor/PCBM blend on fused silica substrates. The excitation wavelength was 530 nm. B: UV-Vis spectra of the exact same films of the photoluminescence measurements.

PEDOT:PSS as electron blocking layers and amorphous titanium dioxide and PFN as hole blocking layers.[99] Notably, working devices could only be produced with the combination of a PEDOT:PSS layer underneath the PMO film and a PFN layer on top of the PCBM layer.

Although we anticipated the PMO films to exhibit a higher performance due to the larger interface area between the donor and acceptor phase[199], the bilayer devices based on dense films showed a higher, but still very moderate photovoltaic performance (compare table 5.1).

Table 5.1: Solar cell performance under 1.5 AM illumination of devices with 100 nm thick organosilica films and PCBM as electron acceptor phase.

sample	V_{OC} [mV]	J_{SC} [mA cm^{-2}]	FF [%]	η [%]
dense organosilica	379	0.042	28	0.0044
porous organosilica	932	0.015	18	0.0025

The reduced J_{SC} and simultaneously enhanced V_{OC} of the PMO-device compared to the bilayer device can be an indication that silica, being introduced during the vapor treatment, reduces the charge carrier mobility and conductivity of the film.[200] This would lead to more pronounced recombination losses due to slower sweep-out of

photogenerated charge carriers and thus a lower overall performance of the device. To examine the influence of the HCl-TEOS vapor treatment in more detail, PL decay measurements from identically synthesized dense films (without template) before and after the HCl-TEOS vapor treatment were carried out.

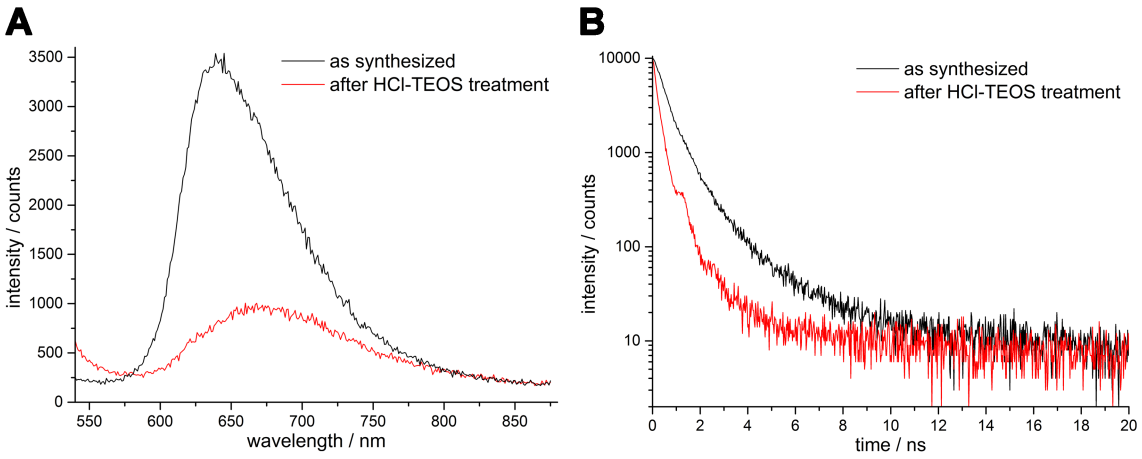

Figure 5.14: Photoluminescence spectra (A) and photoluminescence decay measurements (B) of identically synthesized dense organosilica films before and after the HCl-TEOS vapor treatment. The small shoulder at 1.2 ns in the fluorescence decay of the HCl-TEOS treated film is an artifact of the excitation light due to back scattering effects.

First of all, the PL intensity of a film after the vapor treatment decreased more than 4 times and was shifted to longer wavelength compared to an only dried film (see figure 5.14 A). Complementary to the UV-Vis absorbance data (c.f. figure 5.10) the PL spectrum of the dense film after synthesis appears to have an asymmetric shape, which could be an indication of several luminescent species present. This impression is confirmed by the PL decay measurements, which reveal two lifetimes τ for the trace of the as-synthesized film. The deconvoluted fit of the PL decay trace reveals a short lifetime of 0.68 ns and a longer lifetime component of 2.38 ns. The fit of the PL decay trace of a film after the HCl-TEOS vapor treatment exhibits only one PL lifetime of 0.61 ns. After the vapor treatment and the associated cross-linking of the DTBT precursor, the long-lived PL component vanished and only a short

component below 1 ns remained. This could be the reason that the photovoltaic devices with the hydrolyzed precursor showed only very low performances (see table 5.1). The photovoltaic performance of the PMO material is further diminished by the introduction of more than five times more insulating silica in relation to the semiconducting DTBT precursor and this leads to a dilution of the semiconducting moiety.

5.5 Conclusion

We successfully synthesized a new PMO material comprising a donor-acceptor-donor building block. A stable porous structure that did not exhibit any observable shrinkage after template removal was obtained through vapor infiltration with HCl and TEOS. SAXS and TEM results support the formation of a hexagonal structure with 10 nm pores and approximately 10 nm thick walls. Nitrogen sorption measurements show type IV related isotherm which are not well defined and therefore indicate possible homogeneity issues at the up-scaled bulk synthesis. We could gain insights into the correlation of the π-stacking behavior of the DTBT precursor molecules with the resulting optoelectronic properties in films via UV-Vis and photoluminescence measurements. Due to the planarity of the DTBT unit, the precursor molecules tend to π-stack, which is indicated by a strong red-shift of the UV-Vis absorbance of films compared to the molecules in solution. Interestingly, this red-shift of the UV-Vis absorbance is reduced during the structure-building HCl-TEOS vapor treatment of the corresponding PMO material and even reversed into a slight blue shift. The infiltration of the HCl and TEOS vapor appears to strongly decrease the electronic interactions between the individual DTBT units. This is further supported by PL measurements, which reveal a highly decreased photoluminescence intensity after the vapor treatment. PL decay measurements showed that a second, longer-lived

PL species disappeared after the vapor treatment. The loss of the molecular interactions (*via* stacking) and the fact that 50 wt% insulating silica is introduced into the structure through the HCl-TEOS vapor treatment can explain the moderate performance of the PMO films in photovoltaic devices. We surmise that a PMO-material based on a modified DTBT precursor could show increased performance if the π-stacking interactions could be retained in the final porous structure.

Chapter 6

Nanostructured Fullerenol-Based Organosilica

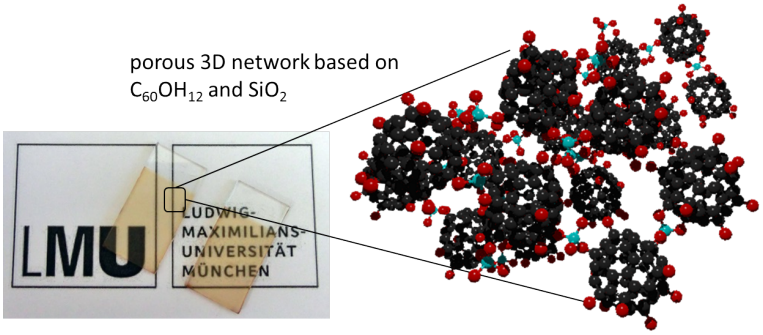

This chapter is based on the manuscript of the article:

"Nanostructured Fullerenol-based Organosilica"

Norma K. Minar, Thomas Bein

in preparation

6.1 Abstract

Novel nanostructured composites consisting mainly of fullerenol molecules interconnected via silica species were synthesized and characterized. The structure formation was based on the co-condensation of a hydroxylated fullerene (fullerenol) and tetraethyl orthosilicate in the presence of non-ionic block co-polymers (Pluronic® P123 and F127), which were subjected to an evaporation-induced self-assembly process. The resulting mesophases inherited over 80 wt% fullerenol in the organosilica and were characterized by 1D small-angle X-ray scattering (SAXS), 2D grazing-incidence small-angle X-ray scattering (GISAXS) and transmission electron microscopy (TEM). The fullerenol-organosilica showed a lamellar structure with the template P123 and a more disordered structure of possibly non-oriented lamellar domains with the template F127, respectively. Remarkably, both structures are stable towards heat treatment at 335 °C in nitrogen. Due to pyrolysis of the structure-directing agent P123, a type IV nitrogen sorption isotherm and a BET surface area of 180 $m^2\ g^{-1}$ were obtained for the corresponding fullerenol-organosilica materials.

6.2 Introduction

The access to C_{60} fullerene at preparative scales beginning in 1990[153], initiated a new area of organic chemistry based on reactions and functionalization of the C_{60} molecule. The number of publications with a focus on fullerene C_{60} rose from only 16 in 1990 to over 1200 in the year 2012.

The high interest in fullerene C_{60} originates from its remarkable mechanical[201], chemical[202], electrochemical[203] and photophysical[204] properties. To employ such properties for applications in materials science or nanotechnology, it is desirable to develop synthetic strategies for the incorporation of fullerene molecules into stable

matrices for the design of solid state devices.

One approach towards this end is the post-synthetic functionalization of a porous matrix, for example porous silica columns.[205,206] The loading of the matrix with fullerene moieties via the surface grafting approach is limited by the surface area of the material, the accessibility of the pores and also the solubility of the C_{60} precursor molecule. Similar factors also restrict an alternative approach, i.e. the physical adsorption of C_{60} into a porous host such as mesoporous silica (MCM-41).[207] To achieve a loading of only 12 wt% in the latter example, the infiltration procedure had to be repeated seven times.

In principle, silica sol-gel methods are promising for the incorporation of fullerenes into a solid-state material, thus enhancing its thermal and mechanical stability.[208] Sol-gel chemistry offers the ease of producing thin homogeneous films with low-temperature treatments in a one-step synthesis procedure. Additionally, the structure and porosity of the resulting material can be tuned and controlled.

In spite of these advantages of the sol-gel method, doping dense silica with pure C_{60} could only be achieved at a level below 1 wt%.[209] An elegant and efficient solution to the solubility issue[210,211] of pure C_{60} is the use of functionalized C_{60} derivates.[212] Polyhydroxylated fullerene - also called fullerenol - combines the intriguing properties of the fullerene core with the polarity and possible anchor points introduced by the hydroxyl groups. Various applications for fullerenols were found, for example in fuel cells[213], macromolecular materials[154] and in the bio-medical and life sciences[214]. A few groups have developed approaches to synthesize dense silica-fullerenol hybrid materials, but only rather modest fullerenol contents as low as 0.6 wt% could be achieved.[208]

Here, we describe the synthesis of a new fullerenol-silica hybrid material with an outstanding high weight ratio of fullerenol to silica in the final composites of over

80 wt%. Fullerenol with approximately 12 hydroxyl groups was selected to obtain a high solubility in polar solvents and additionally maintain a major part of the π-conjugated fullerene core. The issue of fullerene phase separation or aggregation was solved through the hydroxylation and nanostructuring was achieved through an evaporation-induced self-assembly approach with block co-polymers as structure directing agents. The synthesized composites showed a high periodicity and thermal stability up to 335 °C. Bulk material could be synthesized by simple drop casting, and homogeneous thin films could be made by spin coating. The periodic structure of the hybrid material was characterized by small-angle X-ray scattering (SAXS), grazing-incidence small-angle X-ray scattering (GISAXS) and transmission electron microscopy (TEM). The composition was investigated by infra-red absorption spectroscopy and magic-angle spinning nuclear magnetic resonance (MAS-NMR).

6.3 Experimental

General

$H_2SO_4{\cdot}SO_3$ was purchased from ACROS. Fullerene (C_{60}) was purchased from BUCKYUSA (99.5 % grade). All other chemicals and solvents were purchased from SIGMA-ALDRICH and used without further purification.

Methods

The infra-red (IR) absorption spectra of films were recorded with a Nicolet iN10 from THERMOSCIENTIFIC in reflection mode. An atmospheric correction was performed with the Omnic Picta software (v1 SP4). Samples prepared in form of KBr pellets were measured in transmission mode with a BRUKER Model IFS66v/s instrument. Thermogravimetric (TG) measurements were performed in a stream of

synthetic air or nitrogen (25 mL min^{-1}) on a NETZSCH STA 440 C TG/DSC. The measurements were carried out with a heating rate of 10 K min^{-1} in a temperature range from 30 °C to 900 °C. One-dimensional small angle X-ray diffraction measurements were performed on a BRUKER D8 Discover with Ni-filtered CuK_α radiation (0.154 nm) and a position-sensitive detector (LynxEye). TEM images were acquired with a FEI Titan 80-300 microscope equipped with a field emission gun operated at 80 kV. The film material was removed from the glass substrate and deposited on a carbon-coated copper grid for imaging. 2D-grazing incidence small-angle X-ray scattering (GISAXS) was measured with a SAXSess system by ANTON PAAR (CuK_α radiation, sample-detector distance 306.7 mm) with a CCD detector (PI-SCX: 4300, Roper Scientific). The samples were measured for 5–10 min with a tilt angle of 1.2–1.8°with respect to the primary beam. ^{29}Si magic-angle spinning-(MAS) and ^{13}C cross polarization(CP)-MAS-NMR spectra were recorded on a BRUKER Avance III 500 spectrometer (11.7 T, at 99.4 MHz for ^{29}Si and 125.8 MHz for ^{13}C), using a sample spinning frequency of 10 kHz. Nitrogen sorption isotherms were measured with a QUANTACHROME Autosorb-1 instrument at −196 °C. Prior to the measurements, all samples were degassed at 120 °C for 5 h. Brunauer Emmett Teller (BET) surface areas were calculated from the linear section of the BET plot ($\frac{p}{p_0}$ = 0.05–0.2). The pore-size distribution and pore volume were determined using a quenched solid-state density functional theory (QSDFT) method (DFT kernel used: N_2 at −196 °C on carbon, cylindrical and slit-like pores for the adsorption branch).

Synthesis of Hydroxylated Fullerene

The synthesis of the fullerenol precursor was performed according to a procedure developed by Chiang et al..[215] 12 mL of Oleum, $H_2SO_4{\cdot}SO_3$ (65 % SO_3, 100 mmol) was added to 0.80 g (1.1 mmol) C_{60} in a baked-out 250 mL round-bottomed flask

under nitrogen atmosphere and continuous stirring. After a few seconds the solution turned dark green, indicating the formation of organic radicals. Several minutes later poly-cyclosulfated C_{60} precipitated as an orange powder. The reaction mixture was stirred for 15 h at room temperature and afterwards added drop wise to 200 mL diethyl ether under vigorous stirring in an ice bath. The orange-red precipitate was separated by centrifugation at 50 000 rcf for 8 min. Afterwards the precipitate was washed once with diethylether and twice with a 2:1 mixture of diethyl ether and acetonitrile. The product was dried under reduced pressure and 1.19 g (0.92 mmol, 83.4 %) of polycyclosulfated C_{60} was obtained as orange-red powder.

10 mL of degassed H_2O was added to 0.50 g (0.39 mmol) of the poly-cyclosulfated C_{60} under nitrogen atmosphere. The suspension was stirred at 85 °C for 12 h and within this time the color changed from orange-red to dark brown-red. The precipitate was separated from the aqueous solution by centrifugation (50 000 rcf, 15 min). The crude product was washed with water and centrifuged twice (50 000 rcf, 15 min). The product (0.37 g, 0.40 mmol, 97.5 %) was obtained as brown-red powder with an overall yield of 81.3 %.

IR (KBr): $\nu(cm^{-1})$ = 3267 (ν_{O-H}), 1623 ($\nu_{C=C}$), 1362 ($\delta_{2\,(C-O-H)}$), 1049 (ν_{C-O}), 775.

Raman (1064 nm, 15 mW, 1024 Scans, 25 °C, cm^{-1}): 1565 (C=C), 1454 (C=C), 1228, 1053, 782, 711, 559, 399, 336, 232, 120.

Elemental analysis $C_{60}(OH)_{12}{\cdot}6H_2$ O; Calculated: C, 69.77 %; H, 2.34 %; N, 0.00 %. Found: C, 70.04 %; H, 2.39 %; N, 0.00 % (instrument precision ± 0.30 %).

Film Synthesis

$C_{60}(OH)_{12}$ (150 mg, 0.16 mmol) was dissolved in 8.4 mL THF/EtOH (volume ratio 1:1) and diluted HCl (1 M, 150 µL, 0.15 mmol) to give a clear brown solution. The

block co-polymers Pluronic® P123 or F127 were added as structure-directing agents (for exact amounts see table 6.2). After stirring the fullerenol solution for at least 1 h at room temperature, tetraethyl orthosilicate (TEOS, 200 mg, 0.96 mmol) was added to give a molar ratio of fullerenol to silica precursor of 1 to 6.

The resulting sol-gel solution was aged at room temperature for 1 h. Bulk material was synthesized by drop casting the aged sol-gel solution on glass substrates and drying at ambient conditions. Thin films were synthesized by adding 8.4 mL THF/EtOH (volume ratio 1:1) to the sol-gel solution and spin-coating the solution onto glass substrates at 6000 rpm.

After synthesis, spin- and drop-cast films were dried at 120 °C for 1 h. Dried films were extracted in ethanol and THF under reflux for 20 h. A heat treatment at 335 °C was performed in a tube furnace under nitrogen for 10 h with a heating ramp of 1 °C min^{-1}. Supercritical CO_2 extraction was performed in a 100 mL autoclave at 85 bar and 40 °C for 2 h.

6.4 Results and Discussion

Synthesis and Characterization of Fullerenol

The fullerenol synthesis via cyclosulfation in neat fuming sulfuric acid is an elegant way to avoid the formation of hemiketals and sodium impurities.[215] In a second step the poly-cyclosulfated product is hydrolyzed in water to yield a fullerenol with approximately 12 hydroxyl groups. We anticipated that the, according to calculations[216], most stable addition pattern of $C_{60}(OH)_{12}$ fullerenol with a S_6 symmetry could be beneficial for building a periodic network. The IR spectra of the poly-cyclosulfated intermediate product and the hydrolysis product of the same are shown in figure 6.1.

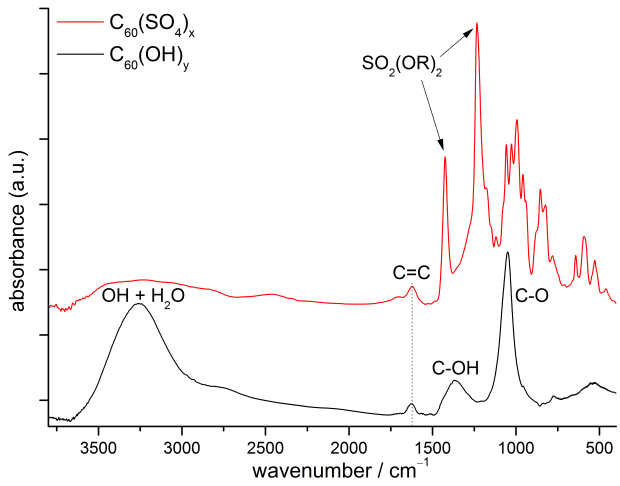

Figure 6.1: IR spectra of cyclosulfated fullerene and the resulting fullerenol of the hydrolysis of the same. The spectra are shifted along the y-axis for clarity.

Both spectra feature a signal around 1622 cm^{-1} corresponding to the $\nu_{C=C}$ vibration of the aromatic fullerene core. The asymmetric and symmetric stretch vibration of the RO-SO_2-OR groups, σ_{as} and σ_s cause peaks at 1425 and 1235 cm^{-1}, respectively. The IR spectrum of the fullerenol $C_{60}(OH)_y$ shows characteristic absorption at 1355 and 1050 cm^{-1} corresponding to σ_2(C-O-H) and ν(C-O). The broad signal located around 3300 cm^{-1} can be assigned to vibrations of the O-H groups and adsorbed water.

The number of functional groups attached to the fullerene core can be estimated *via* thermogravimetric analysis (TGA).[217] Therefore the weight loss of both the cyclosulfated fullerene and the hydroxylated fullerenol was determined by TGA up to 900 °C under nitrogen atmosphere (c.f. figure 6.2). Below 150 °C, strongly adsorbed water molecules are removed. In the temperature range from 150 °C to 570 °C, the moieties attached to the C_{60}-core decompose: for example for fullerenol dehydroxylation, hemiketal formation and pinacol type rearrangements and their

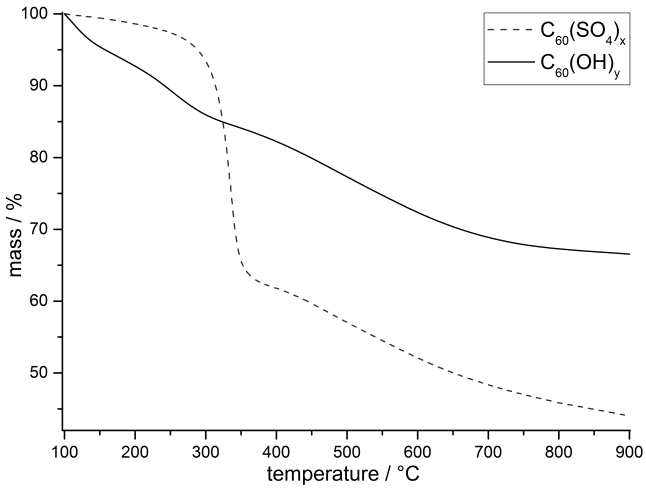

Figure 6.2: TGA thermogramms of cyclosulfated fullerene and the corresponding fullerenol.

degradation take place. The weight loss above 570 °C is attributed to the structural decomposition of the fullerene core.[217] The calculation of the number of attached groups can be carried out via the equation 6.1 according to Goswami et. al..[217] The variable m represents the molecular weight of the attached group, herein 96 g mol^{-1} for a SO_4 and 17 g mol^{-1} for a hydroxy group. The weight loss between 150 and 570 °C corresponds to variable a and the char yield added to the weight loss above 570 °C is described by the variable b.

$$n(\text{attached groups}) = \frac{720 \text{ g mol}^{-1}}{b} \cdot \frac{a}{m} \tag{6.1}$$

The particular weight loss values and corresponding calculated number of adducts are summarized in table 6.1.

Table 6.1: Calculation of number of attached functional groups

Sample	m [g mol^{-1}]	a [%]	b [%]	n(attached groups)
$C_{60}(SO_4)_x$	96	45.5	53.1	6.42
$C_{60}(OH)_y$	17	20.9	71.2	12.4

The resulting values are in good agreement with literature reports.[217] The determined numbers of hydroxyl and cyclosulfate moieties show a 2:1 ratio, which is consistent with the proposed hydrolysis mechanism shown in figure 6.3.[215]

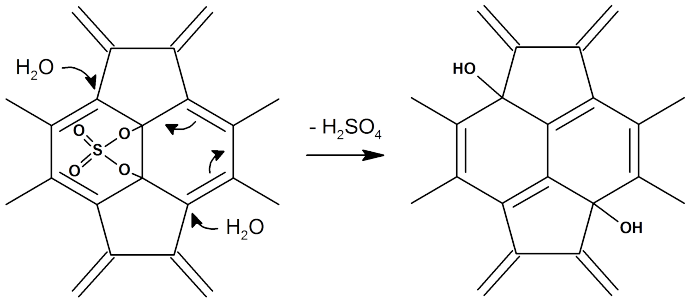

Figure 6.3: Schematic mechanism of the hydrolysis of the cyclosulfate groups at the fullerene core. Due to the proposed mechanism exactly two hydroxyl groups result from each cyclosulfate group.

The molecular formula of $C_{60}(OH)_{12}$ was further confirmed by elemental analysis (see experimental part 6.3). The solubility of the fullerenol implies also a number of hydroxyl groups smaller than 16, because it is soluble in THF and ethanol but not in water.[218] In contrast, pure unfunctionalized C_{60} is only soluble in nonpolar solvents such as benzene or toluene. Due to the shrinkage of the conjugated fullerene π-electron chromophore by virtue of transforming six double bonds into single bonds the absorbance is subject to a hypsochromic shift (see figure 6.4).[176]

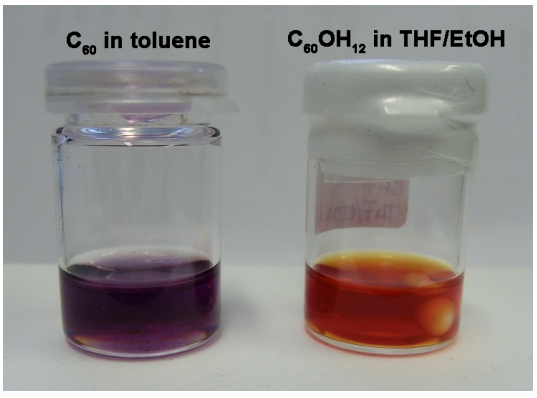

Figure 6.4: Picture of solutions of pure C_{60} in toluene and fullerenol $C_{60}(OH)_{12}$ in THF/ethanol (volume ratio 1:1) displaying the hypsochromic shift of the absorbance.

Synthesis and Characterization of Fullerenol-Organosilica

The good solubility of the synthesized fullerenol in a mixture of ethanol and THF opens up the possibility to apply the evaporation-induced self-assembly (EISA) method with structure-directing micellar surfactant aggregates. For this a polyethyleneoxide (PEO) - polypropyleneoxide (PPO) block co-polymer ($EO_{20}PO_{70}EO_{20}$, Pluronic® P123) was used as structure directing agent. Six molar equivalents of the silica precursor tetraethyl orthosilicate (TEOS) were added to react with the fullerenol to build up a hybrid sol-gel consisting of fullerenol bridged by silica moieties. Initial film samples of sample 6L were synthesized by direct drop casting, revealing a highly periodic structure with reflections up to the 4^{th} order in small-angle X-ray scattering (SAXS). The most intensive reflection at 0.85° 2θ corresponds to a d-spacing of 10.3 nm (c.f. figure 6.5 A). The ratios of the corresponding d-values of the reflections correspond to 1:2:3:4 which can indicate a lamellar structure.[193] The periodic structure is stable towards a heat treatment at 100 °C for 3 h in air and only prone to a slight shrinkage (towards 0.88° 2θ, d = 10.0 nm). Attempts at solvent extraction of the template Pluronic® P123 partially dissolved the fullerenol, destabilized the structure and only a broad reflection around 1.2° 2θ could be detected with a full-width-at-half-maximum (FWHM) value of over 0.5° 2θ (see figure 6.5 B). After an elevated temperature treatment at 200 °C, the structure is stable towards ethanol and a sharp reflection around 0.94° 2θ (d = 9.4 nm) persists. Even a second order reflection can be distinguished at 1.84° 2θ.

The reaction of the silica precursor with the fullerenol and the extraction efficiency were monitored via IR spectroscopy. In figure 6.6 the spectrum of the employed fullerenol is compared to the spectra of $C_{60}(OH)_{12}$-silica composite directly after film synthesis and after the 200 °C heat treatment and solvent treatment with ethanol. The vibrations of the hydrolyzed silica precursor correspond to the intense peak at

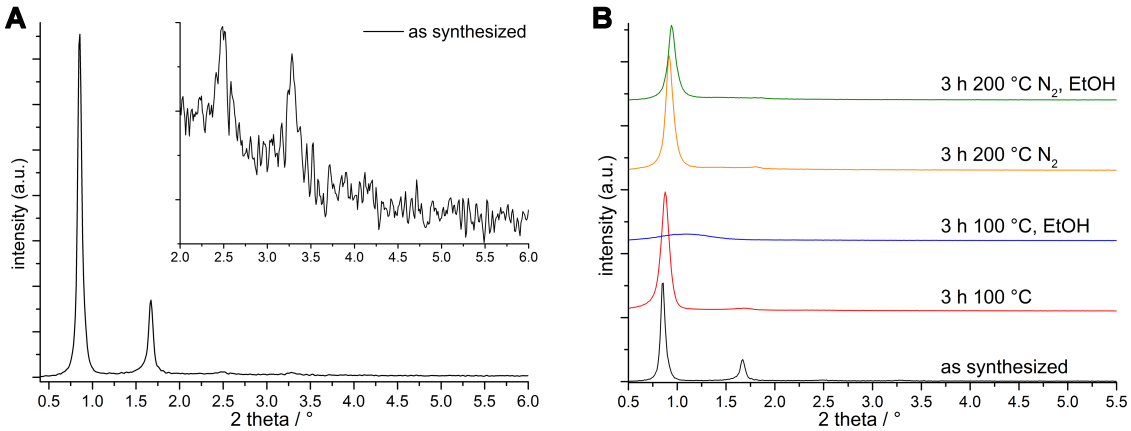

Figure 6.5: SAXS patterns of sample 6L with template Pluronic® P123, 1 equivalent fullerenol and 6 equivalents TEOS. **A**, SAXS pattern of dried material after synthesis. The inset shows the zoomed in pattern, revealing the third and fourth order of the reflection. **B**, SAXS patterns after different temperature and solvent treatments. The patterns are stacked along the y-axis.

1108 cm^{-1} and the signal around 830 cm^{-1}. Signals corresponding to P123 (assigned with a star symbol in figure 6.6) include the characteristic symmetric and asymmetric stretching modes of the CH_2 and CH_3 groups (2868 cm^{-1}–2970 cm^{-1}). Other vibrational modes of P123 are for example the symmetric deformation vibration of the CH_3 groups (1374 cm^{-1}), a wagging mode of the CH_2 groups (1300 cm^{-1}), a C-O-C stretching mode (1250 cm^{-1}) and the rocking mode of CH_3 (934 cm^{-1}).[196] The absence of the C-O-H vibration of the fullerenol in the composite material suggests that the fullerenol hydroxy moieties reacted with the silica precursor to form a silica bridged fullerenol network. The signal of the aromatic fullerene core at around 1647 cm^{-1} is still present in the composite before and after EtOH treatment. The shift by around 20 cm^{-1} can be explained with the changed environment inside the silica network. The slight shoulder at around 1050 cm^{-1} can be assigned to the C-O vibration of the fullerenol moieties. The shift of the signal from the aromatic fullerene core and the absence of the C-O-H vibration are strong indications that a C_{60}-O-Si connection has been established.[219] The IR spectrum after the ethanol extraction resembles the spectrum of the $C_{60}(OH)_{12}$-silica composite directly after

synthesis. Thus the solvent extraction with ethanol was obviously not suitable to remove the template.

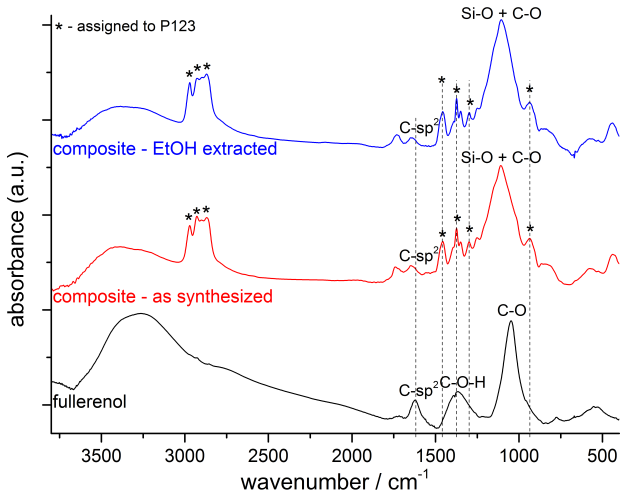

Figure 6.6: IR absorbance spectra of fullerenol and of fullerenol-silica-template composite as synthesized and after 200 °C heat treatment and ethanol extraction. The spectra are shifted along the y-axis for clarity.

The feasibility of decomposing the block co-polymers at higher temperatures was investigated as alternative approach towards the solvent extraction of the template. The thermogravimetric analysis of Pluronic® P123 and F127 under nitrogen reveal that the templates can be completely decomposed in the temperature range from around 320 to 375 °C (figure 6.7). The template removal in inert atmosphere at temperatures below 350 °C has already been successfully applied to other mesoporous organosilica systems.[183,220] A temperature as high as 335 °C was chosen as a good trade-off between removing the template and maintaining the stability of the fullerenol moiety.

However, after heating the composite material to 335 °C for 10 h under nitrogen, the highly periodic structure was destroyed. Only a very broad reflection located around 2.2° 2θ remained in the SAXS pattern shown in figure 6.8. This behavior is char-

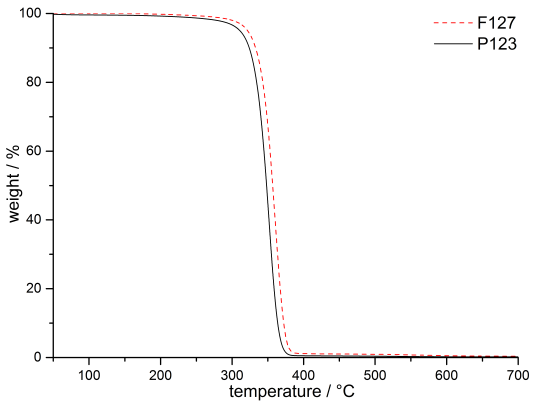

Figure 6.7: Thermogravimetric analysis of the block co-polymers Pluronic® P123 and F127 in nitrogen atmosphere. Total decomposition at about 350 °C was achieved by pyrolysis of the polymers.

acteristic for a lamellar structure oriented parallel to the substrate surface because voids resulting from the pyrolysis of the template layers collapse and the dense layers of fullerenol-silica composite lay loosely stacked parallel to the substrate.[221,222]

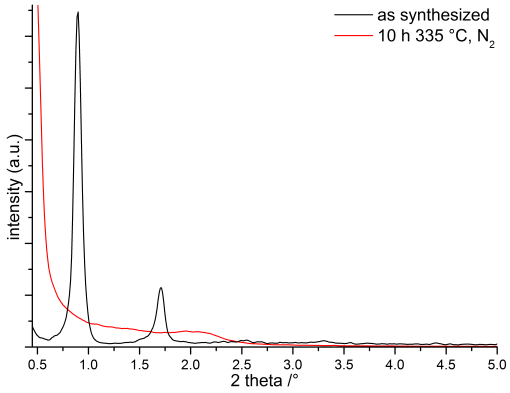

Figure 6.8: SAXS pattern of sample 6L after synthesis and after heat treatment at 335 °C in nitrogen atmosphere.

Different ratios of template to silica and fullerenol precursors were tested to identify a composition with a stable periodic structure. In particular the relative amount of template to TEOS was reduced as it is known that unstable lamellar phases occur preferably at high amounts of template.[223] In addition to Pluronic® P123,

the block co-polymer Pluronic® F127 with a higher PEO content and molecular weight was also used. The molar ratio of fullerenol to silica precursor was fixed at 1 to 6 equivalents (see table 6.2). For a few experiments small amounts of LiCl were added to further enhance the hydrophilic-hydrophobic contrast. However, all films prepared with LiCl delaminated from the substrate after the heat treatment at 335 °C and for this reason experiments with these compositions were not pursued further.

Table 6.2: Composition and SAXS reflections for all fullerenol-silica composite samples. The abbreviation 'br.' in the last two columns stands for 'broad'. A broad signal in SAXS usually implies a collapse of the structure.

		weight ratio						reflection in SAXS [° 2θ]	
sample		$C_{60}(OH)_{12}$ (1 eq.)	TEOS (6 eq.)	template	THF / EtOH	LiCl	HCl (1M)	as synth.	after 335 °C
P123	6L	10.0	13.5	26.5	1000	0.00	10.0	0.89	2.0 br.
	6Li	10.0	13.5	26.5	1000	2.60	10.0	0.89	2.2 br.
	6La	10.0	13.5	20.0	450	0.00	10.0	0.91	2.1 br.
	6Lai	10.0	13.5	20.0	450	2.00	10.0	0.89	1.1 br.
	6Lb	10.0	13.5	13.9	450	0.00	10.0	0.94	1.04
	6Lc	10.0	13.5	11.0	450	0.00	10.0	0.96 br.	1.75 br.
	6Ld	10.0	13.5	26.7	1000	0.00	10.0	0.98	n.a.
F127	6Fa	10.0	13.5	9.30	450	0.00	10.0	0.76	0.83
	6Fai	10.0	13.5	9.35	450	1.40	10.0	0.72	0.79
	6Fb	10.0	13.5	20.9	830	0.00	10.0	0.75	0.80
	6Fc	10.0	13.5	5.34	450	0.00	10.0	n.a.	-
	6Fd	10.0	13.5	4.00	450	0.00	10.0	n.a.	-

The samples 6Lb and 6Fa were chosen for further examination because they exhibited the best periodic order after the elevated heating procedure at 335 °C according to the SAXS measurements (see figure 6.9). Both compositions show sharp reflections and are only prone to a small shrinkage of the structure below 11 %. Upon heat treatment, the *d*-values change from 9.4 to 8.5 nm for sample 6Lb and from 11.6 to 10.6 nm for sample 6Fa, respectively.

IR measurements revealed that the elevated heat treatment was not sufficient to remove the template completely as there are signals originating from the template in the spectra of both composites at 2700–3000 cm^{-1} (see figure 6.10). The aromatic

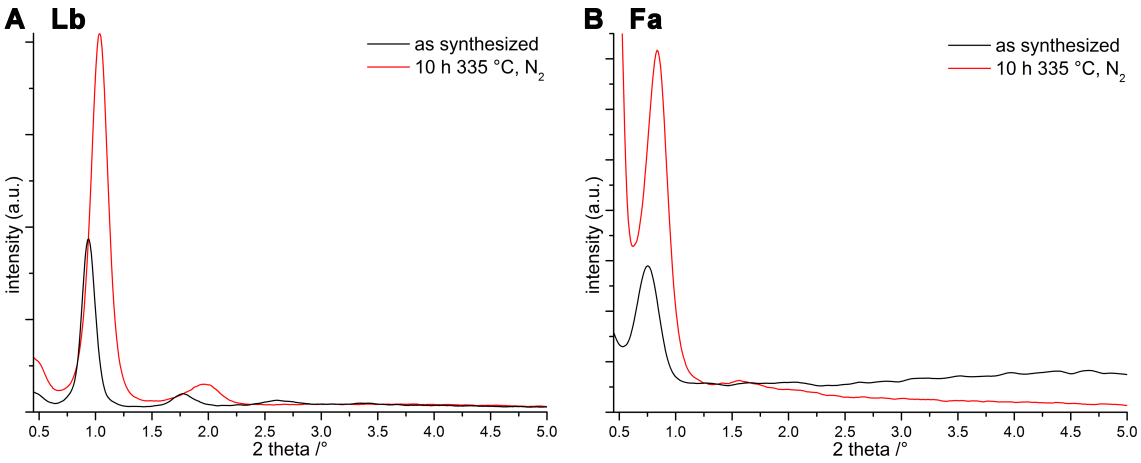

Figure 6.9: SAXS patterns of samples 6Lb (**A**) and 6Fa (**B**) after synthesis and after heat treatment at 335 °C in nitrogen atmosphere.

fullerene core was sustained which is proven by the signal at 1650 cm^{-1} from the $\nu_{C=C}$ vibration. This vibration is still present in the IR spectra after the heat treatment (figure 6.10).

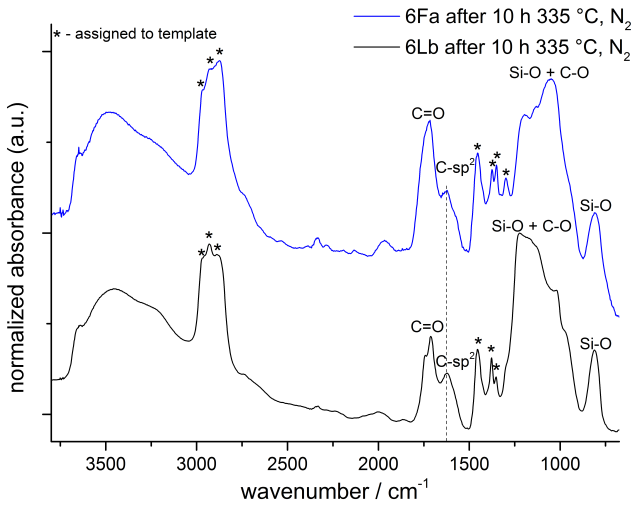

Figure 6.10: IR spectra of composite 6Lb and 6Fa after 10 h at 335 °C in nitrogen atmosphere.

The molecular integrity of the fullerenol-silica nanocomposites, particularly of the fullerene core, was further examined with solid-state magic-angle spinning nuclear magnetic resonance measurements (MAS-NMR). ^{13}C and ^{29}Si MAS-NMR spectra

were recorded from samples 6Lb and 6Fa after synthesis and after 10 h at 335 °C in nitrogen (see figure 6.11). Signals originating from the aromatic sp^2-hybridized carbon atoms of the fullerene core are present for both composites before and after the heat treatment, from 140–155 ppm in the ^{13}C MAS-NMR spectra(figure 6.11 A and C). This supports the assumption that the fullerenol core is stable at this temperature in an inert nitrogen atmosphere. Furthermore, the ethylene and propylene units of the templates P123 and F127 give rise to signals at around 75 and 73 ppm caused by PPO - CH_2 and - CH units, at 70 ppm by PEO - CH_2 units and at 17 ppm by PPO - CH_3 groups.

The ^{29}Si MAS-NMR spectra of both composites show very similar signals (c.f. figure 6.11 B and D). After drying at 120 °C the most dominant species in the silica network is a Q^3 (explained in figure 6.12) species with a signal at −101 ppm. According to the literature[224,225] the ^{29}Si NMR resonance of a Si(O-Aryl)$_4$ species (Q^{4*}) causes a shift at the same position at −101 ppm. The Q^{4*} species would result from a linkage of the fullerenol molecules to the silica precursor at the hydrolysis/condensation reaction. Next to the intense signal from the Q^3 and possibly Q^{4*} species only weak intensities from small amounts of Q^4 (−110 ppm) and Q^2 (−92 ppm) species can be detected (see figure 6.11 B and D).[226] After heating the material to 335 °C under nitrogen, the degree of condensation of the network rises as expected and the signal in the ^{29}Si NMR spectra shifts to lower fields for both composites. Silanol groups on the surface and inside the silica network are still present in samples calcined below 400 °C (2-3 OH groups per nm).[227] Consequently, Q^3 species with one hydroxy group are likely to be present in the heat-treated composites as well. Therefore, the broad signal in the ^{29}Si NMR spectra (figure 6.11 B and D) ranging from −100–110 ppm of the samples after the heat treatment at 335 °C under nitrogen arises from an overlap of the resonances from Q^3, Q^{4*} and

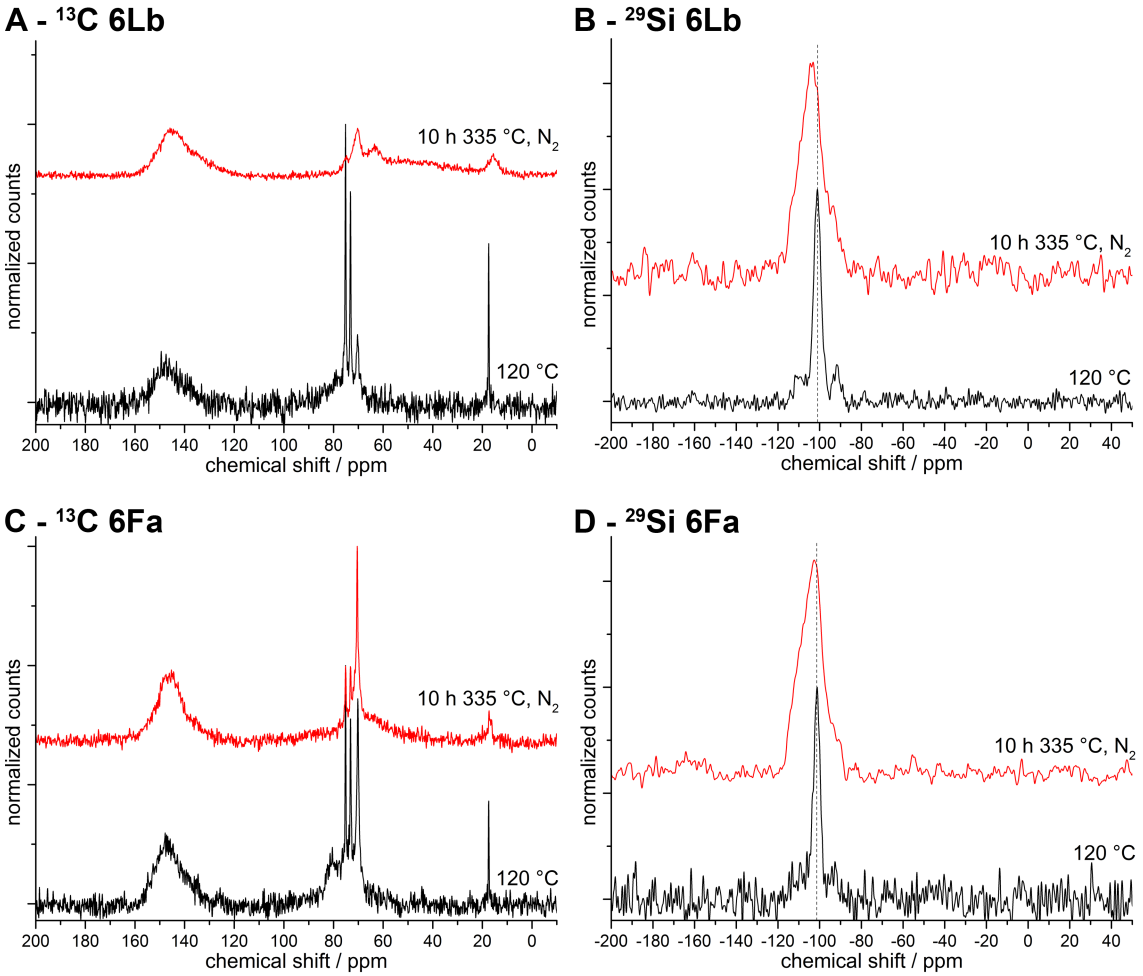

Figure 6.11: ^{13}C and ^{29}Si MAS-NMR spectra of composites 6Lb (A and B) and 6Fa (C and D). The ^{13}C spectra were normalized to the fullerene core signal (around 145 ppm).

Q^4 species.

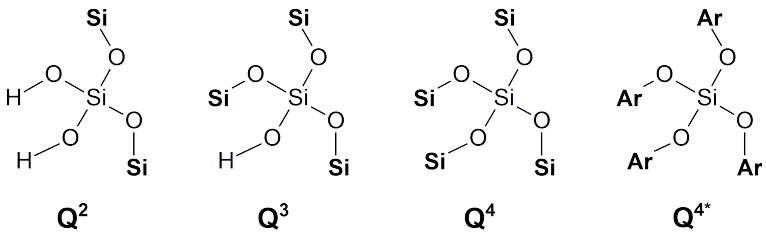

Figure 6.12: Q-species of condensed silica.

Both composites were investigated by nitrogen physisorption to collect more information about the partial removal of the block co-polymers. The composite 6Lb with

the oxygen-richer template P123 shows a type IV isotherm (see figure 6.13) typical for mesoporous materials. The adsorption isotherm shows capillary condensation at high $\frac{p}{p_0}$ values over 0.5 and the very prominent hysteresis indicates slit-like pores with small connection windows. Despite the only partial removal of the template P123 the composite 6Lb shows a BET surface area of over 180 $m^2\,g^{-1}$. The pore size distribution of 6Lb yields a total pore volume of 0.2 $mL\,g^{-1}$ and displays a peak at 2.5 nm and a rather broad distribution of pore diameters from 3 to 10 nm.

Contrary to composite 6Lb, the material 6Fa achieves nearly no accessible porosity after the temperature treatment at 335 °C (compare figure 6.13). The BET surface area of composite 6Fa reaches only 7 $m^2\,g^{-1}$ which implies that the major part of the template F127 remained in the composite. One explanation for this could be that the combustion of Pluronic® P123 proceeds further due to the higher oxygen to carbon ratio compared to Pluronic® F127. An alternative reason could be that the kinetics of the combustion in P123 and F127 are different depending on the interaction with the network material, which could be caused by the different sizes of the hydrophilic and hydrophobic parts.[228].

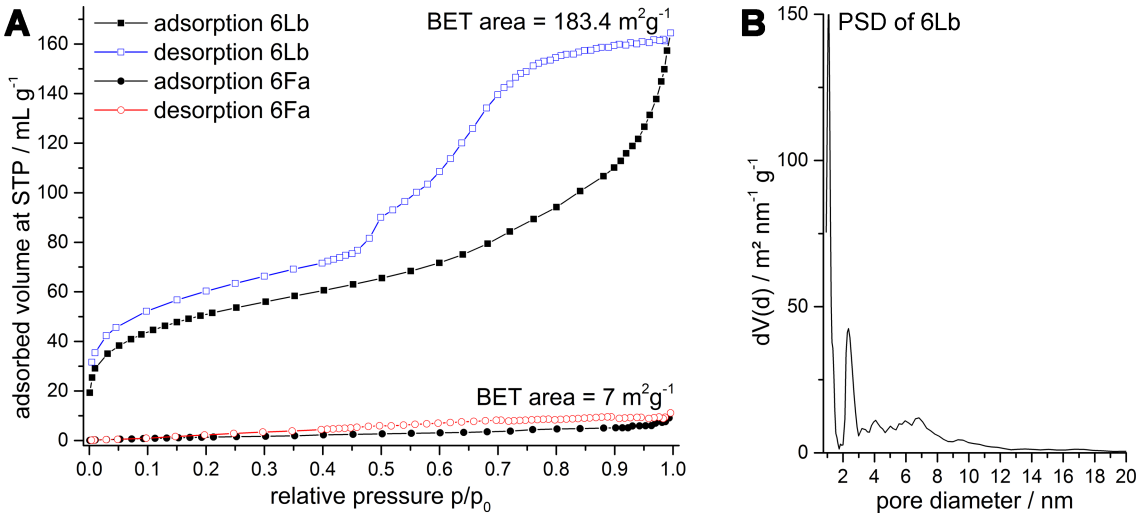

Figure 6.13: A: Nitrogen sorption isotherms at −196 °C of the fullerenol-silica composites 6Lb and 6Fa after the heat treatment at 335 °C in nitrogen. B: Pore size distribution of 6Lb estimated from the adsorption branch.

In view of the above results, different strategies for the removal of the templates were tested and investigated via IR measurements. In these experiments, the fullerenol-silica network was condensed and fixed at 160 °C, and afterwards different extraction methods were applied.

Comparing the IR spectra in figure 6.14 of different samples extracted with THF and ethanol or supercritical CO_2 with the spectrum of the composite after synthesis suggests that the amount of template - regardless if P123 or F127 - is not reduced to any extent. The characteristic vibrational modes of the CH_3 and CH_2 groups of the PEO and PPO blocks can still be detected after the different treatments between 2700–3000 cm^{-1}.

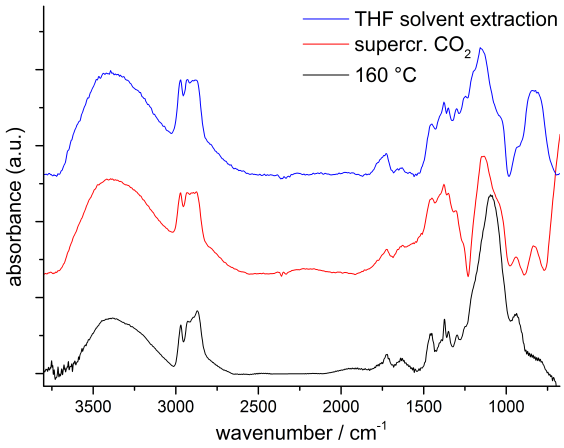

Figure 6.14: IR spectra of composite 6Lb after different extraction treatments. It was not possible to remove the template with any of the applied methods. The spectra were shifted along the y-axis for clarity.

It appears that the Pluronic templates are trapped in closed pores or somehow strongly incorporated into the fullerenol-silica network such that liquid extraction methods cannot remove the block co-polymers.

The structure of both organosilicas, 6Lb and 6Fa, was further investigated by transmission electron microscopy (TEM) and grazing incidence small-angle X-ray scat-

tering (GISAXS). A sample of the thermally unstable compound 6L was also investigated to reveal differences in the nanoscopic structure that could be responsible for the difference in thermal stability.

The TEM micrographs of the sample 6L further confirm the lamellar structure of these materials (c.f. figure 6.15 A1 and A2). Parallel layers with a distance of approximately 5–6 nm can be detected. The lower distance measured in the TEM pictures compared to the *d*-spacing of 10 nm obtained by SAXS can be a result of strong shrinkage of the structure induced by the high vacuum of the electron microscope sample chamber. The GISAXS pattern of sample 6L in figure 6.16 A reveals only one strong in-plane reflection, which supports the assumption of a lamellar phase being oriented parallel to the substrate.

Surprisingly, it was not possible to gather any structural information about the 6Lb sample from TEM measurements (figure 6.15 B1 and B2), even though it shows signals due to periodic structuring in 1-D SAXS (see figure 6.9 A) and also in GISAXS measurements before and after the 335 °C heat treatment (figure 6.16 B). The absence of out-of-plane reflections in the GISAXS pattern also indicate a lamellar phase similar to 6L. We note that the TEM sample preparation of lamellar phases can be very delicate due to the insufficient mechanical stability.[29] The nanostructure of the sample could be destroyed in the process of removing the film material from the substrate prior to the TEM investigation.

The TEM micrographs of the 6Fa composite show clearly nanostructured features. The layer distances are in accordance with the SAXS reflection pattern of around 10 nm. The GISAXS measurements before and after the 335 °C heat treatment provide more information about the structure (see figure 6.17). The as-synthesized 6Fa composite (figure 6.17 A) shows also a strong in-plane signal suggesting a lamellar structure with layers parallel to the substrate. In contrast to the composites with

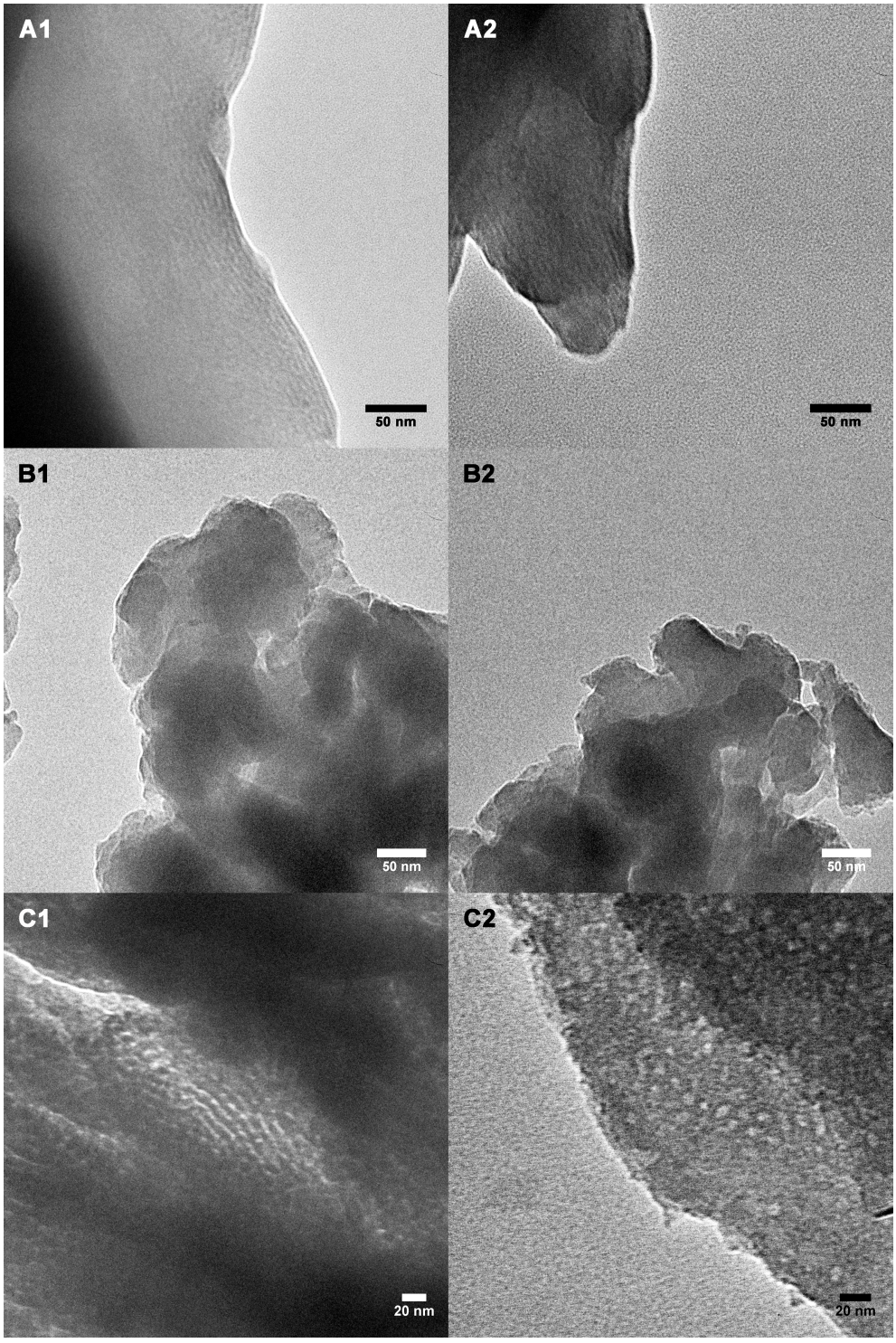

Figure 6.15: TEM micrographs of removed spin-coated thin films of different fullerenol-silica-template composites: **A**, sample 6L as synthesized, **B**, sample 6Lb after 10 h at 335 °C in N_2, **C**, sample 6Fa after 10 h at 335 °C in N_2.

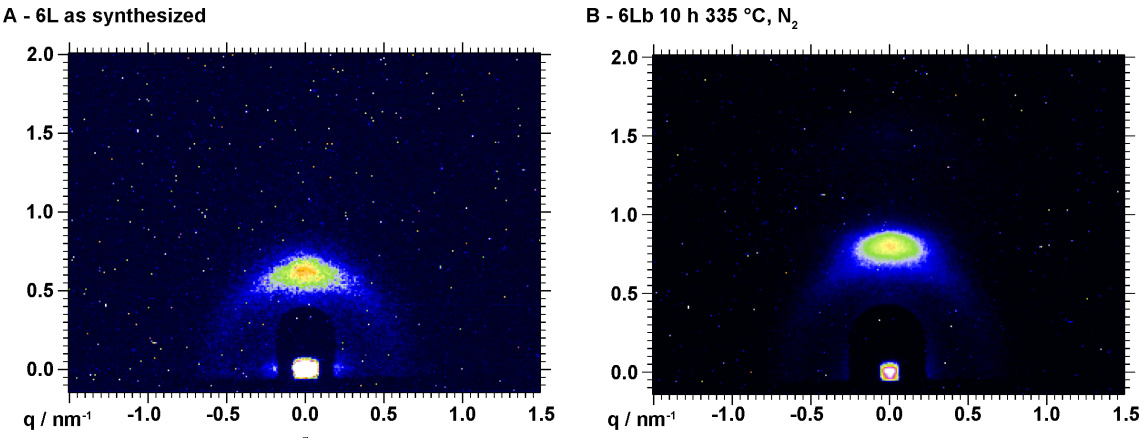

Figure 6.16: 2D-GISAXS pattern of as synthesized 6L composite (**A**) and composite 6Lb (**B**) after 10 h at 335 °C under nitrogen.

Pluronic® P123, there is also an arc with about the same q_z value as the in-plane reflection. The prominent in-plane reflection vanishes after the 335 °C heat treatment and the arc-shaped reflection builds nearly a closed Debye-Scherrer ring around the origin (c.f. figure 6.17 B).

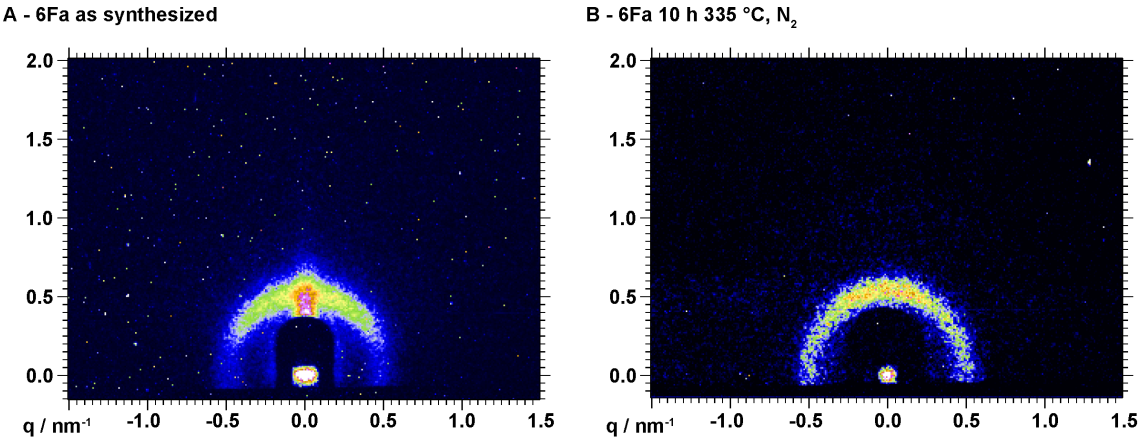

Figure 6.17: 2D-GISAXS pattern of composite 6Fa as synthesized (**A**) and after 10 h at 335 °C under nitrogen (**B**).

On the one hand, this arc can indicate the presence of smaller domains of a lamellar phase that do not show a preferential orientation towards the substrate.[229] On the other hand, this arc can also originate from a worm-like or correlated micellar structure corresponding to disordered pores.[25,230] These pores seem to be inaccessible such that none of the applied extraction methods was capable of removing the tem-

plate. This phenomenon of inaccessible mesopores has been occasionally observed for thin silica films structured with CTAB and also for Pluronic templates.[223,230]

6.5 Conclusion

We were able to successfully synthesize a new nanostructured organosilica material mainly based on fullerenol (around 80 wt%). By adjusting the amount of structure-directing block co-polymer P123 or F127, respectively, we could synthesize periodically structured and thermally stable fullerenol-silica-block-co-polymer composites. As demonstrated with X-ray scattering data, the lamellar mesostructures of the new composites are stable up to 335 °C in nitrogen and towards polar solvents such as ethanol, THF and also supercritical CO_2. The integrity of the fullerene core after these treatments confirmed by MAS-NMR and IR spectroscopy. IR and ^{29}Si MAS-NMR measurements of the composites imply a covalent linkage between the fullerenol and the interconnecting silica. The organosilica templated with P123 shows accessible porosity revealed by nitrogen sorption experiments. The corresponding BET surface area reaches over 180 $m^2\,g^{-1}$ and the total pore volume accounts for 0.2 $mL\,g^{-1}$.

By building a stable matrix with fullerenol molecules, the advantageous properties of the same can be applied in solid-state devices. This opens up the possibility to exploit the full potential of fullerenol in various applications such as catalysis[231], sorption[206] or optoelectronics[232]. We suggest that our results offer a starting point to further develop differently structured fullerenol-organosilica materials with enhanced porosity, which will be attractive in view of the above applications.

Chapter 7

Conclusion and Outlook

In this work, the nanostructure and the properties of novel inorganic-organic hybrid materials were investigated. In chapter 3 the in-situ polymerization of a conducting polymer into a preformed functionalized mesoporous titania network was explored. Novel hybrid materials based on sol-gel synthesis routes are the focus of chapters 4, 5 and 6. Structuring on the nanoscale was achieved through soft-templating methods, using an evaporation-induced self-assembly approach.

In chapter 3 the synthetic incorporation of the conducting polymer MEH-PPV into mesoporous titanium dioxide films is demonstrated. The inexpensive, non-toxic Gilch polymerization allowed for the straightforward synthesis of the conjugated MEH-PPV polymer inside the mesoporous titania network. We investigated the influence of molecular surface functionalization preceding the in-situ polymerization. These studies revealed that the molecular nature of the anchor molecule is essential to yield a high amount of in-situ synthesized MEH-PPV. Surface functionalization with chemically active molecules, which can be incorporated into the MEH-PPV, were found to enhance the amount of the in-situ synthesized MEH-PPV up to a factor of 6 compared to non-functionalized samples, and thus enhanced the resulting

absorbance which is essential for a good performance of solar cells. The evaluation of the corresponding UV-Vis spectra revealed a higher conjugation length, as determined from the optical band gap, for in-situ polymerized MEH-PPV with reactive functionalized titania compared to non-reactive functionalized or untreated titania. While we observed a decrease in the effective conjugation length of the in-situ synthesized MEH-PPV in non-treated titania films with smaller pores, this undesired effect was avoided through the application of an active surface functionalization.
The two reactive anchor molecules acrylic acid and a molecule mimicking the monomer structure were investigated in photovoltaic devices. The drastically different performance of the two anchor molecules suggests that the orientation of the grown polymer chains with respect to the titania surface is an essential factor for efficient power generation.
In this study we showed that the successful in-situ growth of a conjugated polymer in a porous metal oxide scaffold is on the one hand dependent on the functionalization of the surface with active anchor sites. Conversely, this alone is not sufficient and the geometry of the anchoring via the reactive linker molecules seems to be advantageous for a perpendicular orientation of the polymer chains with respect to the oxide surface.
These results could give an impetus for additional studies regarding the further optimization of the anchor molecules and the resulting orientation of the in-situ synthesized polymer chains, to exploit the full potential of the conjugated polymer-metal oxide hybrid material. This way, new synthesis methods for more efficient hybrid materials for photovoltaic devices can be developed.

Chapters 4 and 5 focus on the synthesis of novel PMO materials from silsesquioxane precursor molecules using a soft-templating EISA approach.
In chapter 4 a symmetrically functionalized fullerene C_{60} precursor was developed

as building block for the formation of a fullerene-based covalent framework. We surmised that the high three-dimensional symmetry of the fullerene precursor facilitates the self-assembly process of the highly periodic orthorhombic structure with *Fmmm* symmetry and a pore size of around 7.5 nm. Measurements of the dielectric constant of the fullerene PMO revealed a relatively low value around 3.0.

We suggest that integrating symmetrically functionalized fullerene cores having tunable optoelectronic properties into PMO materials will provide access to a whole new family of hybrid fullerene materials with intriguing optical and electronic properties.

Following a different approach, in chapter 5 a silsesquioxane with a π-conjugated donor-acceptor-donor unit (dithienyl benzothiadiazole = DTBT) was employed with the goal to introduce intriguing photosensitive and conductive properties into the resulting PMO. Contrary to the 3D-symmetric fullerene precursor, the bulky and not completely rigid structure of the DTBT silsesquioxane molecule apparently does not create sufficient linkages in the network, such that so far we could not obtain a stable periodic structure with the DTBT precursor alone using the EISA process. Notably, a phase transformation from the unstable lamellar pure DTBT precursor phase to a stable PMO with hexagonally arranged pores could be performed through a vapor infiltration of HCl and TEOS.

We gained insights regarding the molecular interactions between the DTBT moieties in the network walls by optical and crystallographic measurements. All methods provide a strong indication that the DTBT units π stack in the first place and show strong electronic interactions. However, the stabilization of the network through the vapor treatment causes the DTBT units to loose some contact and therefore they seem to be even more isolated than in solution: 1. the maximum of the UV-Vis absorbance is blue-shifted compared to a THF solution and 2. PL decay measurements reveal the disappearance of a longer-lived light emitting species. The moderate per-

formance of the DTBT PMO in photovoltaic devices is attributed to the partial loss of π-stacking and the associated decrease in transport properties. In addition to the loss of the π-π interactions, 50 wt% silica is introduced by the HCl-TEOS vapor treatment, which has insulating properties and diminishes the conductivity of the final PMO even further.

We believe that a PMO material based on DTBT or related precursors can show highly increased photosensitive and electronic properties if the interactions in form of the π-stacking are maintained in the final porous structure. In future experiments, synthetic pathways with alternative silsesquioxane building blocks and different soft templates should be explored to achieve this goal.

In the last part, in chapter 6, hydroxylated fullerenol was incorporated into a nanostructured silica network. We successfully synthesized lamellar mesostructures of fullerenol-silica-block-co-polymer composites with two different triblock copolymers, P123 and F127. Remarkably, both lamellar structures show a good thermal stability, up to 335 °C in nitrogen, and are stable towards polar solvents such as ethanol, THF and also supercritical CO_2, which was confirmed by X-ray scattering. MAS-NMR and IR spectroscopic measurements displayed the integrity of the fullerene core after the synthetic steps. Additionally, the results of the IR measurements of the composites imply a covalent interconnection of the fullerenol and the silica moieties. After removal of the template P123, the corresponding composites show a relatively high porosity with a pore volume of 0.2 $mL\,g^{-1}$ and a BET surface of over 180 $m^2\,g^{-1}$. Creating a stable matrix with a high fullerenol content (around 80 wt%) opens up the possibility to apply this new material in solid-state devices. This way the full potential of fullerenol in various applications such as catalysis or sorption can be made accessible. These results offer a starting point to optimize the nanostructure in future experiments, for example by applying other structure

directing agents. Enhanced access to the pores will lead to a significantly increased active surface area and the intriguing properties introduced by the fullerenol moieties can be investigated.

In summary, hybrid inorganic-organic materials are of great interest for a large variety of applications. Nearly unlimited combinations of organic with inorganic building blocks offer new and exciting perspectives through customizing the properties of the resulting material. Understanding the relationship between the properties and the structure on the molecular- and the nano-scale is essential for the successful design of new versatile materials for future applications, ranging from photovoltaic devices to dielectric interlayers in microelectronics.

Abbreviation list

AFM ..... atomic force microscopy

BET ..... Brunauer-Emmett-Teller

BJH ..... Barret-Joyner-Halenda

CCD ..... charge-coupled device

cmc ..... critical micelle concentration

CP ..... cross-polarization

CSA ..... cooperative self-assembly

DFT ..... density functional theory

DMA 9,10-dimethylanthracene

DPV ..... differential pulsed voltammetry

DSC ..... differential scanning calorimetry

DTBT ..... dithienyl-benzo-thiadiazole

EISA ..... evaporation-induced self-assembly

EQE ..... external quantum efficiency

FWHM ..... full-width-at-half-maximum

GISAXS	2D grazing-incidence small-angle X-ray scattering
HOMO	highest occupied molecular orbital
IR	infrared
ITO	indium tin oxide
LCT	liquid-crystal templating
LUMO	lowest unoccupied molecular orbital
MALS	multi-angle laser scattering
MAS	magic-angle spinning
MAS-NMR	magic-angle spinning nuclear magnetic resonance
MEH-PPV	poly[2-methoxy-5-(2'-ethyl-hexyloxy)-1,4-phenylene vinylene]
NMR	nuclear magnetic resonance
PCBM	phenyl-C61-butyric acid methyl ester
PEDOT:PSS	poly(3,4-ethylenedioxythiophene)-poly(styrenesulfonate)
PEO	poly(ethylene oxide)
PFN	poly (9,9-bis(3'-(N,N-dimethylamino)propyl)-2,7-fluorene)-alt-2,7-(9,9-dioctylfluorene)
PL	photoluminescence
PMMA	poly(methyl methacrylate)
PMO	periodic mesoporous organosilica
PPO	poly(propylene oxide)

PPV ..... poly(p-phenylene vinylene)

PSD ..... pore size distribution

QSDFT ..... quenched solid state density functional theory

SAXS ..... small-angle X-ray scattering

SEC ..... size exclusion chromatography

SEM ..... scanning electron microscopy

$TBAPF_6$ ..... tetrabutylammonium hexafluorophosphate

TEM ..... transmission electron microscopy

TEOS ..... tetraethyl orthosilicate

TGA ..... thermogravimetric analysis

UV-Vis ..... ultra violet-visible

WAXS ..... wide-angle X-ray scattering

XRD ..... X-ray diffraction

Bibliography

[1] Feynman, R. P. *Engineering and Science* **1960**, *4*, 23–36.

[2] Johnson-McDaniel, D.; Barrett, C. A.; Sharafi, A.; Salguero, T. T. *Journal of the American Chemical Society* **2012**, *135*, 1677–1679.

[3] Sanchez, C.; Julian, B.; Belleville, P.; Popall, M. *Journal of Materials Chemistry* **2005**, *15*, 3559–3592.

[4] Roduner, E. *Chemical Society Reviews* **2006**, *35*, 583–592.

[5] Cao, G. *Nanostructures and Nanomaterials - Synthesis, Properties, and Applications*; Imperial College Press: London, 2004; p 81ff.

[6] Gomez-Romero, P. *Advanced Materials* **2001**, *13*, 163–174.

[7] Kickelbick, G. *Hybrid Materials. Synthesis, Characterization, and Applications.*; Wiley-VCH: Weinheim, 2007.

[8] Mammeri, F.; Bourhis, E. L.; Rozes, L.; Sanchez, C. *Journal of Materials Chemistry* **2005**, *15*, 3787–3811.

[9] Boucle, J.; Ravirajan, P.; Nelson, J. *J. Mater. Chem.* **2007**, *17*, 3141–3153.

[10] Ebelmen, J.-J. *Ann. de Chim. et de Phys.* **1846**, *XXII*, 211.

[11] Geffcken, W.; Berger, E. Verfahren zur Aenderung des Reflexionsvermoegens optischer Glaeser. 1943; `http://www.google.com/patents/DE736411C?cl=de`.

[12] Niederberger, M.; Pinna, N. *Metal Oxide Nanoparticles in Organic Solvents:*

Synthesis, Formation, Assembly and Application; Engineering Materials and Processes; Springer: London, 2009.

[13] Cushing, B. L.; Kolesnichenko, V. L.; O'Connor, C. J. *Chemical Reviews* **2004**, *104*, 3893–3946.

[14] McCusker, L. B.; Liebau, F.; Engelhardt, G. *Pure Appl. Chem.* **2001**, *73*, 381–394.

[15] Barrer, R. M.; Denny, P. J. *Journal of the Chemical Society (Resumed)* **1961**, 971–982.

[16] Kresge, C. T.; Leonowicz, M. E.; Roth, W. J.; Vartuli, J. C.; Beck, J. S. *Nature* **1992**, *359*, 710–712.

[17] Zhao, D.; Feng, J.; Huo, Q.; Melosh, N.; Fredrickson, G. H.; Chmelka, B. F.; Stucky, G. D. *Science* **1998**, *279*, 548–552.

[18] Yang, H.; Kuperman, A.; Coombs, N.; Mamiche-Afara, S.; Ozin, G. A. *Nature* **1996**, *379*, 703–705.

[19] Ogawa, M. *Langmuir* **1997**, *13*, 1853–1855.

[20] Israelachvili, J. N.; Mitchell, D. J.; Ninham, B. W. *Journal of the Chemical Society, Faraday Transactions 2: Molecular and Chemical Physics* **1976**, *72*, 1525–1568.

[21] Balazs, D. A.; Godbey, W. *Journal of Drug Delivery* **2011**, *2011*, 326497.

[22] Brinker, C. J.; Lu, Y.; Sellinger, A.; Fan, H. *Adv. Mater.* **1999**, *11*, 579–585.

[23] Wan, Y.; Zhao, *Chemical Reviews* **2007**, *107*, 2821–2860.

[24] Doshi, D. A.; Gibaud, A.; Goletto, V.; Lu, M.; Gerung, H.; Ocko, B.; Han, S. M.; Brinker, C. J. *Journal of the American Chemical Society* **2003**, *125*, 11646–11655.

[25] Gibaud, A.; Grosso, D.; Smarsly, B.; Baptiste, A.; Bardeau, J. F.; Babonneau, F.; Doshi, D. A.; Chen, Z.; Brinker, C. J.; Sanchez, C. *The Journal of*

Physical Chemistry B **2003**, *107*, 6114–6118.

[26] Schuster, J.; Kohn, R.; Doblinger, M.; Keilbach, A.; Amenitsch, H.; Bein, T. *Journal of the American Chemical Society* **2012**, *134*, 11136–11145.

[27] Grosso, D.; Cagnol, F.; Soler-Illia, G. J. D. A. A.; Crepaldi, E. L.; Amenitsch, H.; Brunet-Bruneau, A.; Bourgeois, A.; Sanchez, C. *Advanced Functional Materials* **2004**, *14*, 309–322.

[28] Sanchez, C.; Boissiere, C.; Grosso, D.; Laberty, C.; Nicole, L. *Chemistry of Materials* **2008**, *20*, 682–737.

[29] Alberius, P. C. A.; Frindell, K. L.; Hayward, R. C.; Kramer, E. J.; Stucky, G. D.; Chmelka, B. F. *Chemistry of Materials* **2002**, *14*, 3284–3294.

[30] Monnier, A.; Schueth, F.; Huo, Q.; Kumar, D.; Margolese, D.; Maxwell, R. S.; Stucky, G. D.; Krishnamurty, M.; Petroff, P.; Firouzi, A.; Janicke, M.; Chmelka, B. F. *Science* **1993**, *261*, 1299–1303.

[31] Nishiyama, N.; Tanaka, S.; Egashira, Y.; Oku, Y.; Ueyama, K. *Chemistry of Materials* **2003**, *15*, 1006–1011.

[32] Tanaka, S.; Nishiyama, N.; Oku, Y.; Egashira, Y.; Ueyama, K. *Journal of the American Chemical Society* **2004**, *126*, 4854–4858.

[33] Gupta, G.; Iyer, S.; Leasure, K.; Virdone, N.; Dattelbaum, A. M.; Atanassov, P. B.; Lopez, G. P. *ACS Nano* **2013**, *7*, 5300–5307.

[34] Mizoshita, N.; Tani, T.; Inagaki, S. *Chemical Society Reviews* **2011**, *40*, 789–800.

[35] Hoffmann, F.; Cornelius, M.; Morell, J.; Froeba, M. *Angewandte Chemie International Edition* **2006**, *45*, 3216–3251.

[36] Hoffmann, F.; Froeba, M. *Chemical Society Reviews* **2011**, *40*, 608–620.

[37] Inagaki, S.; Guan, S.; Fukushima, Y.; Ohsuna, T.; Terasaki, O. *Journal of the American Chemical Society* **1999**, *121*, 9611–9614.

[38] Asefa, T.; MacLachlan, M. J.; Coombs, N.; Ozin, G. A. *Nature* **1999**, *402*, 867–871, 10.1038/47229.

[39] Melde, B. J.; Holland, B. T.; Blanford, C. F.; Stein, A. *Chemistry of Materials* **1999**, *11*, 3302–3308.

[40] Van Der Voort, P.; Esquivel, D.; De Canck, E.; Goethals, F.; Van Driessche, I.; Romero-Salguero, F. J. *Chemical Society Reviews* **2013**, *42*, 3913–3955.

[41] Hatton, B.; Landskron, K.; Whitnall, W.; Perovic, D.; Ozin, G. A. *Accounts of Chemical Research* **2005**, *38*, 305–312.

[42] Inagaki, S.; Guan, S.; Ohsuna, T.; Terasaki, O. *Nature* **2002**, *416*, 304–307, 10.1038/416304a.

[43] Kapoor, M. P.; Yang, Q.; Inagaki, S. *Journal of the American Chemical Society* **2002**, *124*, 15176–15177.

[44] Takeda, H.; Ohashi, M.; Tani, T.; Ishitani, O.; Inagaki, S. *Inorganic Chemistry* **2010**, *49*, 4554–4559.

[45] Li, Y.; Auras, F.; Loebermann, F.; Doeblinger, M.; Schuster, J.; Peter, L.; Trauner, D.; Bein, T. *Journal of the American Chemical Society* **2013**, *135*, 18513–18519.

[46] Mizoshita, N.; Ikai, M.; Tani, T.; Inagaki, S. *Journal of the American Chemical Society* **2009**, *131*, 14225–14227.

[47] Ikai, M.; Maegawa, Y.; Goto, Y.; Tani, T.; Inagaki, S. *Journal of Materials Chemistry A* **2014**, 11857–11865.

[48] Nudelman, F.; Gotliv, B. A.; Addadi, L.; Weiner, S. *Journal of Structural Biology* **2006**, *153*, 176–187.

[49] Heinemann, F.; Launspach, M.; Gries, K.; Fritz, M. *Biophysical Chemistry* **2011**, *153*, 126–153.

[50] Wei, L.; Hu, N.; Zhang, Y. *Materials* **2010**, *3*, 4066–4079.

[51] Coakley, K. M.; Srinivasan, B. S.; Ziebarth, J. M.; Goh, C.; Liu, Y.; McGehee, M. D. *Adv. Funct. Mater.* **2005**, *15*, 1927–1932.

[52] Posudievsky, O. Y.; Telbiz, G. M.; Rossokhaty, V. K. *Journal of Materials Chemistry* **2006**, *16*, 2485–2489.

[53] Molenkamp, W. C.; Watanabe, M.; Miyata, H.; Tolbert, S. H. *Journal of the American Chemical Society* **2004**, *126*, 4476–4477.

[54] Kandada, A. R. S.; Guarnera, S.; Tassone, F.; Lanzani, G.; Petrozza, A. *Advanced Functional Materials* **2014**, *24*, 3094–3099.

[55] Novak, B. M. *Advanced Materials* **1993**, *5*, 422–433.

[56] Alvaro, M.; Corma, A.; Ferrer, B.; Galletero, M. S.; GarcÃa, H.; Peris, E. *Chemistry of Materials* **2004**, *16*, 2142–2147.

[57] Atienzar, P.; Ishwara, T.; Horie, M.; Durrant, J. R.; Nelson, J. *J. Mater. Chem.* **2009**, *19*, 5377–5380.

[58] Moller, K.; Bein, T. *Chemistry of Materials* **1998**, *10*, 2950–2963.

[59] Azzaroni, O. *Journal of Polymer Science Part A: Polymer Chemistry* **2012**, *50*, 3225–3258.

[60] Strandwitz, N. C.; Nonoguchi, Y.; Boettcher, S. W.; Stucky, G. D. *Langmuir* **2010**, *26*, 5319–5322.

[61] Jain, S. M.; Biedrzycki, J. J.; Maurino, V.; Zecchina, A.; Mino, L.; Spoto, G. *Journal of Materials Chemistry A* **2014**, *2*, 12247–12254.

[62] Gorman, C. B.; Petrie, R. J.; Genzer, J. *Macromolecules* **2008**, *41*, 4856–4865.

[63] Uemura, T.; Ono, Y.; Kitagawa, K.; Kitagawa, S. *Macromolecules* **2007**, *41*, 87–94.

[64] Pasetto, P.; Blas, H.; Audouin, F.; Boissiere, C.; Sanchez, C.; Save, M.; Charleux, B. *Macromolecules* **2009**, *42*, 5983–5995.

[65] Toney, M. F. In *Encyclopedia of Materials Characterization*; Brundle, C. R.,

Evans, C. A. J., Wilson, S., Eds.; Manning Publications Co.: Greenwich, 1992; Vol. 1; Chapter 4.1, pp 198–213.

[66] Bragg, W. *Proceedings of the Cambridge Philosophical Society* **1913**, *17*, 43–57.

[67] Durose, K.; Asher, S. E.; Jaegermann, W.; Levi, D.; McCandless, B. E.; Metzger, W.; Moutinho, H.; Paulson, P. D.; Perkins, C. L.; Sites, J. R.; Teeter, G.; Terheggen, M. *Progress in Photovoltaics* **2004**, *12*, 177–217.

[68] Patterson, A. L. *Physical Review* **1939**, *56*, 978–82.

[69] Mueller-Buschbaum, P. In *Applications of Synchrotron Light to Scattering and Diffraction in Materials and Life Sciences*; Gomez, M., Nogales, A., Garcia-Gutierrez, M. C., Ezquerra, T. A., Eds.; Lecture Notes in Physics; Springer Berlin Heidelberg, 2009; Vol. 776; Chapter 3, pp 61–89.

[70] Abbe, E. *Proceedings of the Bristol Naturalists' Society* **1874**, *1*, 200–261.

[71] Williams, D. B.; Carter, C. B. *Transmission Electron Microscopy - A Textbook for Materials Science*; Springer: New York, 2009; Vol. 2.

[72] Binnig, G.; Quate, C. F.; Gerber, C. *Physical Review Letters* **1986**, *56*, 930–933.

[73] Zhong, Q.; Inniss, D.; Kjoller, K.; Elings, V. B. *Surface Science Letters* **1993**, *290*, L688–L692.

[74] Skoog, D. A.; West, D. M.; Holler, F. J.; Crouch, S. R. *Fundamentals of Analytical Chemistry*, 8th ed.; Brooks Cole Pub Co: Philadelphia, 2003.

[75] Wedler, G. *Lehrbuch der Physikalischen Chemie*, 6th ed.; Wiley-VCH: Weinheim, 2012.

[76] Tauc, J.; Grigorovici, R.; Vancu, A. *physica status solidi (b)* **1966**, *15*, 627–637.

[77] Buchholz, D. B.; Liu, J.; Marks, T. J.; Zhang, M.; Chang, R. P. H. *ACS*

Applied Materials & Interfaces **2009**, *1*, 2147–2153.

[78] Hesse, M.; Meier, H.; Zeeh, B. *Spektroskopische Methoden in der organischen Chemie*, 7th ed.; Thieme Verlag: Stuttgart, 2005.

[79] Eckert, H. In *Encyclopedia of Materials Characterization*; Brundle, C. R., Evans, C. A. J., Wilson, S., Eds.; Manning Publications Co.: Greenwich, 1992; Vol. 1; Chapter 8.4, pp 460–472.

[80] Hahn, E. L. *Physical Review* **1950**, *80*, 580–594, PR.

[81] Sing, K. *Phys. Appl. Chem.* **1985**, *57*, 603–619.

[82] Rouquerol, J.; Avnir, D.; Fairbridge, C. W.; Everett, D. H.; Haynes, J. M.; Pernicone, N.; Ramsay, J. D. F.; Sing, K. S. W.; Unger, K. K. *Pure and Applied Chemistry* **1994**, *66*, 1739.

[83] Langmuir, I. *Physical Review* **1916**, *8*, 149–176, PR.

[84] Rouquerol, F.; Rouquerol, J.; Sing, K. S. W. *Adsorption by Powders and Porous Solids - Principles, Methodology and Application*; Academic Press: San Diego, 1999.

[85] Condon, J. *Surface Area and Porosity Determinatons by Physisorption - Measurements and Theory*; Elsevier: Amsterdam, 2006.

[86] Cychosz, K. A.; Guo, X.; Fan, W.; Cimino, R.; Gor, G. Y.; Tsapatsis, M.; Neimark, A. V.; Thommes, M. *Langmuir* **2012**, *28*, 12647–12654.

[87] Thommes, M.; Morell, J.; Cychosz, K. A.; Froeba, M. *Langmuir* **2013**, *29*, 14893–14902.

[88] Schmidt, W. *Optische Spektroskopie*, 2nd ed.; Wiley-VCH: Weinheim, 2000; pp 296 – 300.

[89] Gallagher, P. K. In *Characterization of Materials, Part I, Materials Science and Technology*; Cahn, R., Haasen, P., Kramer, E., Eds.; VCH: Weinheim, 1992; Vol. 2A; Chapter 7, p 491.

[90] Lathe, G. H.; Ruthven, C. R. *Biochem J* **1955**, *60*, xxxiv.

[91] Lathe, G. H.; Ruthven, J., C. R. J. *Biochem. J.* **1956**, *62*, 665–74.

[92] Porath, J.; Flodin, P. E. R. *Nature* **1959**, *183*, 1657–1659.

[93] Moore, J. C. *Journal of Polymer Science Part A: General Papers* **1964**, *2*, 835–843.

[94] Grubisic, Z.; Rempp, P.; Benoit, H. *Journal of Polymer Science, Part B: Polymer Physics* **1996**, *34*, 1707–1714.

[95] Wyatt, P. J. *Analytica Chimica Acta* **1993**, *272*, 1–40.

[96] Dkhissi, A. *Synthetic Metals* **2011**, *161*, 1441–1443.

[97] Xu, T.; Qiao, Q. *Energy & Environmental Science* **2011**, *4*, 2700–2720.

[98] Coakley, K. M.; McGehee, M. D. *Chemistry of Materials* **2004**, 4533–4542.

[99] Steim, R.; Kogler, F. R.; Brabec, C. J. *Journal of Materials Chemistry* **2010**, *20*, 2499–2512.

[100] Heeger, A. J. *Reviews of Modern Physics* **2001**, *73*, 681–700.

[101] Burroughes, J. H.; Bradley, D. D. C.; Brown, A. R.; Marks, R. N.; Mackay, K.; Friend, R. H.; Burns, P. L.; Holmes, A. B. *Nature* **1990**, *347*, 539–541.

[102] Bruetting, W.; Buchwald, E.; Egerer, G.; Meier, M.; Zuleeg, K.; Schwoerer, M. *Synthetic Metals* **1997**, *84*, 677–678.

[103] Benten, H.; Ogawa, M.; Ohkita, H.; Ito, S. *Advanced Functional Materials* **2008**, *18*, 1563–1572.

[104] Lipomi, D. J.; Chiechi, R. C.; Reus, W. F.; Whitesides, G. M. *Advanced Functional Materials* **2008**, *18*, 3469–3477.

[105] Chen, Z.; Ma, K.; Wang, G.; Zhao, X.; Tang, A. *Journal of Molecular Structure: THEOCHEM* **2000**, *498*, 227–232.

[106] Kirchmeyer, S.; Starck, H. C. *Nachrichten aus der Chemie* **2006**, *54*, 971–977.

[107] Stuart, M. A. C.; Huck, W. T. S.; Genzer, J.; Muller, M.; Ober, C.; Stamm, M.;

Sukhorukov, G. B.; Szleifer, I.; Tsukruk, V. V.; Urban, M.; Winnik, F.; Zauscher, S.; Luzinov, I.; Minko, S. *Nature Materials* **2010**, *9*, 101–113.

[108] Kiriy, A.; Senkovskyy, V.; Sommer, M. *Macromolecular Rapid Communications* **2011**, *32*, 1503–1517.

[109] Huddleston, N. E.; Sontag, S. K.; Bilbrey, J. A.; Sheppard, G. R.; Locklin, J. *Macromolecular Rapid Communications* **2012**, *33*, 2115–2120.

[110] Kang, S.; Ono, R. J.; Bielawski, C. W. *Journal of the American Chemical Society* **2013**, *135*, 4984–4987.

[111] Hains, A. W.; Ramanan, C.; Irwin, M. D.; Liu, J.; Wasielewski, M. R.; Marks, T. J. *ACS Applied Materials & Interfaces* **2009**, *2*, 175–185.

[112] Zhitenev, N. B.; SidorenkoA,; Tennant, D. M.; Cirelli, R. A. *Nature Nanotechnology* **2007**, *2*, 237–242.

[113] Alexandre, M.; Dubois, P. *Materials Science and Engineering: R: Reports* **2000**, *28*, 1–63.

[114] Laine, R. M.; Choi, J.; Lee, I. *Advanced Materials* **2001**, *13*, 800–803.

[115] Liang,; Liu, J.; Gong, X. *Langmuir* **2000**, *16*, 9895–9899.

[116] Pyun, J.; Matyjaszewski, K. *Chemistry of Materials* **2001**, *13*, 3436–3448.

[117] Jing, C.; Chen, L.; Shi, Y.; Jin, X. *European Polymer Journal* **2005**, *41*, 2388–2394.

[118] Wu, C. G.; Bein, T. *Science* **1994**, *264*, 1757–9.

[119] Tepavcevic, S.; Darling, S. B.; Dimitrijevic, N. M.; Rajh, T.; Sibener, S. J. *small* **2009**, *5*, 1776–1783.

[120] Kim, S. W.; Cho, H. G.; Park, C. R. *Langmuir* **2009**, *25*, 9030–9036.

[121] Zhang, Y.; Wang, C.; Rothberg, L.; Ng, M.-K. *Journal of Materials Chemistry* **2006**, *16*, 3721–3725.

[122] Schwalm, T.; Rehahn, M. *Macromolecules* **2007**, *40*, 3921–3928.

[123] O'Regan, B.; Gratzel, M. *Nature* **1991**, *353*, 737–740.

[124] Ito, S.; Murakami, T. N.; Comte, P.; Liska, P.; Graetzel, C.; Nazeeruddin, M. K.; Graetzel, M. *Thin Solid Films* **2008**, *516*, 4613–4619.

[125] Szeifert, J. M.; Fattakhova-Rohlfing, D.; Georgiadou, D.; Kalousek, V.; Rathousky, J.; Kuang, D.; Wenger, S.; Zakeeruddin, S. M.; Gratzel, M.; Bein, T. *Chemistry of Materials* **2009**, *21*, 1260–1265.

[126] Anderson, N.; Bagge, W.; Webber, C.; Zarras, P.; Davis, M. C. *Synthetic Communications* **2008**, *38*, 3903–3908.

[127] Neef, C. J.; Ferraris, J. P. *Macromolecules* **2000**, *33*, 2311–2314.

[128] Deffieux, D.; Fabre, I.; Courseille, C.; Quideau, S. *The Journal of Organic Chemistry* **2002**, *67*, 4458–4465.

[129] Benjamin, I.; Hong, H.; Avny, Y.; Davidov, D.; Neumann, R. *Journal of Materials Chemistry* **1998**, *8*, 919–924.

[130] Szeifert, J. M.; Fattakhova-Rohlfing, D.; Rathousky, J.; Bein, T. *Chemistry of Materials* **2012**, *24*, 659–663.

[131] Niederberger, M.; Bartl, M. H.; Stucky, G. D. *Chemistry of Materials* **2002**, 4364–4370.

[132] Lu, S.; Sun, S.-S.; Jiang, X.; Mao, J.; Li, T.; Wan, K. *Journal of Materials Science: Materials in Electronics* **2010**, *21*, 682–686.

[133] Gilch, H. G.; Wheelwright, W. L. *Journal of Polymer Science Part A-1: Polymer Chemistry* **1966**, *4*, 1337–1349.

[134] Hontis, L.; Vrindts, V.; Vanderzande, D.; Lutsen, L. *Macromolecules* **2003**, *36*, 3035–3044.

[135] Schwalm, T.; Wiesecke, J.; Immel, S.; Rehahn, M. *Macromolecular Rapid Communications* **2009**, *30*, 1295–1322.

[136] Meier, H.; Stalmach, U.; Kolshorn, H. *Acta Polymerica* **1997**, *48*, 379–384.

[137] Bredas, J. L.; Silbey, R.; Boudreaux, D. S.; Chance, R. R. *Journal of the American Chemical Society* **1983**, *105*, 6555–6559.

[138] Rissler, J. *Chemical Physics Letters* **2004**, *395*, 92–96.

[139] Scelta, D.; Ceppatelli, M.; Santoro, M.; Bini, R.; Gorelli, F. A.; Perucchi, A.; Mezouar, M.; van der Lee, A.; Haines, J. *Chemistry of Materials* **2014**, *26*, 2249–2255.

[140] Wu, C.-G.; Bein, T. *Science* **1994**, *266*, 1013–1015.

[141] Coakley, K. M.; Liu, Y.; McGehee, M. D.; Frindell, K. L.; Stucky, G. D. *Advanced Functional Materials* **2003**, *13*, 301–306.

[142] Markov, D. E.; Tanase, C.; Blom, P. W. M.; Wildeman, J. *Physical Review B* **2005**, *72*, 045217.

[143] Abrusci, A.; Ding, I. K.; Al-Hashimi, M.; Segal-Peretz, T.; McGehee, M. D.; Heeney, M.; Frey, G. L.; Snaith, H. J. *Energy & Environmental Science* **2011**, *4*, 3051–3058.

[144] Gaudin, O. P. M.; Samuel, I. D. W.; Amriou, S.; Burn, P. L. *Applied Physics Letters* **2010**, *96*, 053305.

[145] Docampo, P.; Hey, A.; Guldin, S.; Gunning, R.; Steiner, U.; Snaith, H. J. *Advanced Functional Materials* **2012**, *22*, 5010–5019.

[146] Nguyen, T.-Q.; Martini, I. B.; Liu, J.; Schwartz, B. J. *The Journal of Physical Chemistry B* **1999**, *104*, 237–255.

[147] Docampo, P.; Snaith, H. J. *Nanotechnology* **2011**, *22*, 225403/1–225403/8.

[148] Garnett, E. C.; Yang, P. *Journal of the American Chemical Society* **2008**, *130*, 9224–9225.

[149] Noriega, R.; Rivnay, J.; Vandewal, K.; Koch, F. P. V.; Stingelin, N.; Smith, P.; Toney, M. F.; Salleo, A. *Nat Mater* **2013**, *12*, 1038–1044.

[150] Prins, P.; Grozema, F. C.; Schins, J. M.; Savenije, T. J.; Patil, S.; Scherf, U.;

Siebbeles, L. D. A. *Physical Review B* **2006**, *73*, 045204.

[151] Hertel, D.; Baessler, H. *ChemPhysChem* **2008**, *9*, 666–688.

[152] Kroto, H. W.; Heath, J. R.; O'Brien, S. C.; Curl, R. F.; Smalley, R. E. *Nature* **1985**, *318*, 162–163.

[153] Kratschmer, W.; Lamb, L. D.; Fostiropoulos, K.; Huffman, D. R. *Nature* **1990**, *347*, 354–358.

[154] Giacalone, F.; Martin, N. *Advanced Materials* **2010**, *22*, 4220–4248.

[155] Giacalone, F.; Martin, N. *Chemical Reviews* **2006**, *106*, 5136–5190.

[156] Geckeler, K. E.; Samal, S. *Journal of Macromolecular Science, Part C* **2000**, *40*, 193–205.

[157] Rao, A. M.; Zhou, P.; Wang, K.-A.; Hager, G. T.; Holden, J. M.; Wang, Y.; Lee, W. T.; Bi, X.-X.; Eklund, P. C.; Cornett, D. S.; Duncan, M. A.; Amster, I. J. *Science* **1993**, *259*, 955–957.

[158] Chiang, L. Y.; Wang, L. Y.; Kuo, C.-S. *Macromolecules* **1995**, *28*, 7574–7576.

[159] Cao, T.; Webber, S. E. *Macromolecules* **1996**, *29*, 3826–3830.

[160] Nayak, P. L.; Yang, K.; Dhal, P. K.; Alva, S.; Kumar, J.; Tripathy, S. K. *Chemistry of Materials* **1998**, *10*, 2058–2066.

[161] Schmaltz, B.; Mathis, C.; Brinkmann, M. *Polymer* **2009**, *50*, 966–972.

[162] Wang, J.; Shen, Y.; Kessel, S.; Fernandes, P.; Yoshida, K.; Yagai, S.; Kurth, D.; Moehwald, H.; Nakanishi, T. *Angewandte Chemie International Edition* **2009**, *48*, 2166–2170.

[163] Peng, P.; Li, F.-F.; Neti, V. S. P. K.; Metta-Magana, A. J.; Echegoyen, L. *Angewandte Chemie International Edition* **2014**, *53*, 160–163.

[164] Stein, A. *Advanced Materials* **2003**, *15*, 763–775.

[165] Jana, R.; Trivedi, R.; Tunge, J. A. *Organic Letters* **2009**, *11*, 3434–3436.

[166] Willing, D. N. Platinum-siloxane complexes as hydrosilation catalysts. 1968.

[167] Camps, X.; Hirsch, A. *Journal of the Chemical Society, Perkin Transactions 1* **1997**, 1595–1596.

[168] Witte, P.; Hoermann, F.; Hirsch, A. *Chem.–Eur. J.* **2009**, *15*, 7423–7433.

[169] Hirsch, A.; Lamparth, I.; Groesser, T.; Karfunkel, H. R. *Journal of the American Chemical Society* **1994**, *116*, 9385–6.

[170] Falcaro, P.; Grosso, D.; Amenitsch, H.; Innocenzi, P. *The Journal of Physical Chemistry B* **2004**, *108*, 10942–10948.

[171] Besson, S.; Ricolleau, C.; Gacoin, T.; Jacquiod, C.; Boilot, J.-P. *Microporous and Mesoporous Materials* **2003**, *60*, 43–49.

[172] Tate, M. P.; Urade, V. N.; Kowalski, J. D.; Wei, T.-c.; Hamilton, B. D.; Eggiman, B. W.; Hillhouse, H. W. *The Journal of Physical Chemistry B* **2006**, *110*, 9882–9892.

[173] Tanaka, S.; Katayama, Y.; Tate, M. P.; Hillhouse, H. W.; Miyake, Y. *Journal of Materials Chemistry* **2007**, *17*, 3639–3645.

[174] Song, L.; Feng, D.; Campbell, C. G.; Gu, D.; Forster, A. M.; Yager, K. G.; Fredin, N.; Lee, H.-J.; Jones, R. L.; Zhao, D.; Vogt, B. D. *Journal of Materials Chemistry* **2010**, *20*, 1691–1701.

[175] Hare, J. P.; Kroto, H. W.; Taylor, R. *Chemical Physics Letters* **1991**, *177*, 394–398.

[176] Cardullo, F.; Seiler, P.; Isaacs, L.; Nierengarten, J. F.; Haldimann, R. F.; Diederich, F.; Mordasini-Denti, T.; Thiel, W.; Boudon, C.; Gisselbrecht, J. P.; Gross, M. *Helv. Chim. Acta* **1997**, *80*, 343–371.

[177] Haddon, R. C.; Perel, A. S.; Morris, R. C.; Palstra, T. T. M.; Hebard, A. F.; Fleming, R. M. *Applied Physics Letters* **1995**, *67*, 121–123.

[178] Singh, S.; Mohapatra, S. K.; Sharma, A.; Fuentes-Hernandez, C.; Barlow, S.; Marder, S. R.; Kippelen, B. *Applied Physics Letters* **2013**, *102*, 153303.

[179] Chen, S.; Ye, G.; Xiao, Z.; Ding, L. *Journal of Materials Chemistry A* **2013**, *1*, 5562–5566.

[180] MacKenzie, R. C. I.; Frost, J. M.; Nelson, J. *The Journal of Chemical Physics* **2010**, *132*, 064904.

[181] Wang, Y.; Seifert, G.; Hermann, H. *physica status solidi (a)* **2006**, *203*, 3868–3872.

[182] Zagorodniy, K.; Hermann, H.; Taut, M.; Seifert, G.; Zschech, E. *Microelectronic Engineering* **2008**, *85*, 2118–2122.

[183] Lu, Y.; Fan, H.; Doke, N.; Loy, D. A.; Assink, R. A.; LaVan, D. A.; Brinker, C. J. *Journal of the American Chemical Society* **2000**, *122*, 5258–5261.

[184] Breselge, M.; Van Severen, I.; Lutsen, L.; Adriaensens, P.; Manca, J.; Vanderzande, D.; Cleij, T. *Thin Solid Films* **2006**, *511-512*, 328–332.

[185] Hermann, H.; Zagorodniy, K.; Touzik, A.; Taut, M.; Seifert, G. *Microelectronic Engineering* **2005**, *82*, 387–392.

[186] Lee, H.-J.; Soles, C. L.; Liu, D.-W.; Bauer, B. J.; Lin, E. K.; Wu, W.-L.; Gallagher, M. *Journal of Applied Physics* **2006**, *100*, 064104.

[187] Jousseaume, V.; Rolland, G.; Babonneau, D.; Simon, J. P. *Thin Solid Films* **2009**, *517*, 4413–4418.

[188] Lee, B.; Park, Y.-H.; Hwang, Y.-T.; Oh, W.; Yoon, J.; Ree, M. *Nature Materials* **2005**, *4*, 147–150.

[189] Sonar, P.; Singh, S. P.; Sudhakar, S.; Dodabalapur, A.; Sellinger, A. *Chemistry of Materials* **2008**, *20*, 3184–3190.

[190] Zhou, H.; Yang, L.; Xiao, S.; Liu, S.; You, W. *Macromolecules* **2010**, *43*, 811–820.

[191] Patil, A. V.; Lee, W.-H.; Kim, K.; Lee, Y.-S.; Kang, I.-N.; Lee, S.-H. *Synthetic*

Metals **2011**, *161*, 1838–1844.

[192] Bambrough, C. M.; Slade, R. C. T.; Williams, R. T. *Journal of Materials Chemistry* **1998**, *8*, 569–571.

[193] Liu, Y. *Journal of Porous Materials* **2011**, *18*, 597–605.

[194] Sonar, P.; Singh, S. P.; Leclere, P.; Surin, M.; Lazzaroni, R.; Lin, T. T.; Dodabalapur, A.; Sellinger, A. *Journal of Materials Chemistry* **2009**, *19*, 3228–3237.

[195] Holmqvist, P.; Alexandridis, P.; Lindman, B. *The Journal of Physical Chemistry B* **1998**, *102*, 1149–1158.

[196] Socrates, G. *Infrared and Raman Characteristic Group Frequencies: Tables and Charts*, 3rd ed.; Wiley-VCH: Weinheim, 2004.

[197] Ng, S.-C.; Xu, J.-M.; S. O. Chan, H.; Fujii, A.; Yoshino, K. *Journal of Materials Chemistry* **1999**, *9*, 381–385.

[198] Frost, J. M.; Faist, M. A.; Nelson, J. *Advanced Materials* **2010**, *22*, 4881–4884.

[199] Kim, S.-S.; Jo, J.; Chun, C.; Hong, J.-C.; Kim, D.-Y. *Journal of Photochemistry and Photobiology, A: Chemistry* **2007**, *188*, 364–370.

[200] Vandewal, K.; Gadisa, A.; Oosterbaan, W. D.; Bertho, S.; Banishoeib, F.; Van Severen, I.; Lutsen, L.; Cleij, T. J.; Vanderzande, D.; Manca, J. V. *Advanced Functional Materials* **2008**, *18*, 2064–2070.

[201] Hebard, A. F. *Annual Review of Materials Science* **1993**, *23*, 159–191.

[202] Hirsch, A.; Brettreich, M. *Fullerenes - Chemistry and Reactions*; Wiley-VCH Verlag: Weinheim, 2005; p 423.

[203] Echegoyen, L.; Echegoyen, L. E. *Accounts of Chemical Research* **1998**, *31*, 593–601.

[204] Guldi, D. M.; Prato, M. *Accounts of Chemical Research* **2000**, *33*, 695–703.

[205] Tran, T. A.; Gibbs-Hall, I.; Young, P. J.; Thompson, J. D.; Stoll, D. R. *Ana-*

lytical Chemistry **2013**, *85*, 11817–11825.

[206] Nasonova, K. V.; Melenevskaya, E. Y.; Shamanin, V. V.; Podosenova, N. G. *Fullerenes, Nanotubes and Carbon Nanostructures* **2012**, *20*, 367–370.

[207] Kyriakopoulos, J.; Tzirakis, M. D.; Panagiotou, G. D.; Alberti, M. N.; Triantafyllidis, K. S.; Giannakaki, S.; Bourikas, K.; Kordulis, C.; Orfanopoulos, M.; Lycourghiotis, A. *Applied Catalysis B: Environmental* **2012**, *117-118*, 36–48.

[208] Xia, H.; Jiang, Z.; Zhang, J.; Wang, J.; Zhang, Y.; Nie, Q. *Journal of Materials Science & Technology* **2004**, *20*, 555–557.

[209] Brusatin, G.; Innocenzi, P. *Journal of Sol-Gel Science and Technology* **2001**, *22*, 189–204.

[210] Martin, T. P.; Naeher, U.; Schaber, H.; Zimmermann, U. *Physical Review Letters* **1993**, *70*, 3079–3082.

[211] Kato, H.; Nakamura, A.; Takahashi, K.; Kinugasa, S. *Physical Chemistry Chemical Physics* **2009**, *11*, 4946–4948.

[212] Maggini, M.; Scorrano, G.; Prato, M.; Brusatin, G.; Innocenzi, P.; Guglielmi, M.; Renier, A.; Signorini, R.; Meneghetti, M.; Bozio, R. *Advanced Materials* **1995**, *7*, 404–406.

[213] Hinokuma, K.; Ata, M. *Chemical Physics Letters* **2001**, *341*, 442–446.

[214] Chaudhuri, P.; Paraskar, A.; Soni, S.; Mashelkar, R. A.; Sengupta, S. *ACS Nano* **2009**, *3*, 2505–2514.

[215] Chiang, L. Y.; Wang, L.-Y.; Swirczewski, J. W.; Soled, S.; Cameron, S. *The Journal of Organic Chemistry* **1994**, *59*, 3960–3968.

[216] Wang, B.-C.; Cheng, C.-Y. *Journal of Molecular Structure: THEOCHEM* **1997**, *391*, 179–187.

[217] Goswami, T. H.; Singh, R.; Alam, S.; Mathur, G. N. *Thermochimica Acta*

2004, *419*, 97–104.

[218] Kokubo, K.; Matsubayashi, K.; Tategaki, H.; Takada, H.; Oshima, T. *ACS Nano* **2008**, *2*, 327–333.

[219] Singh, R.; Goswami, T. *Journal of Organometallic Chemistry* **2008**, *693*, 2021–2032.

[220] Matos, J. R.; Kruk, M.; Mercuri, L. P.; Jaroniec, M.; Asefa, T.; Coombs, N.; Ozin, G. A.; Kamiyama, T.; Terasaki, O. *Chemistry of Materials* **2002**, *14*, 1903–1905.

[221] Meng, Y.; Gu, D.; Zhang, F.; Shi, Y.; Cheng, L.; Feng, D.; Wu, Z.; Chen, Z.; Wan, Y.; Stein, A.; Zhao, D. *Chemistry of Materials* **2006**, *18*, 4447–4464.

[222] Park, J.-G.; Lee, K.-R.; Lee, U. H.; Lee, H.-J.; Kwon, Y.-U. *Journal of Materials Chemistry* **2011**, *21*, 3903–3909.

[223] Lu, Y.; Ganguli, R.; Drewien, C. A.; Anderson, M. T.; Brinker, C. J.; Gong, W.; Guo, Y.; Soyez, H.; Dunn, B.; Huang, M. H.; Zink, J. I. *Nature* **1997**, *389*, 364–368.

[224] Schraml, J.; Chvalovsky, V.; Magi, M.; Lippmaa, E. *Collect. Czech. Chem. Commun.* **1981**, *46*, 377–90.

[225] Pikies, J.; Wojnowski, W. *Zeitschrift fuer anorganische und allgemeine Chemie* **1984**, *511*, 219–224.

[226] Ide, M.; El-Roz, M.; De Canck, E.; Vicente, A.; Planckaert, T.; Bogaerts, T.; Van Driessche, I.; Lynen, F.; Van Speybroeck, V.; Thybault-Starzyk, F.; Van Der Voort, P. *Physical Chemistry Chemical Physics* **2013**, *15*, 642–650.

[227] Zhuravlev, L. T. *Colloids Surf., A* **2000**, *173*, 1–38.

[228] Kleitz, F.; Schmidt, W.; Schueth, F. *Microporous and Mesoporous Materials* **2003**, *65*, 1–29.

[229] Di, Z.; Posselt, D.; Smilgies, D.-M.; Papadakis, C. M. *Macromolecules* **2010**,

43, 418–427.

[230] Tate, M. P.; Eggiman, B. W.; Kowalski, J. D.; Hillhouse, H. W. *Langmuir* **2005**, *21*, 10112–10118.

[231] Sun, Y.-B.; Cao, C.-Y.; Yang, S.-L.; Huang, P.-P.; Wang, C.-R.; Song, W.-G. *Chemical Communications* **2014**, *50*, 10307–10310.

[232] Rincon, M. E.; Hu, H.; Campos, J.; Ruiz-Garcia, J. *The Journal of Physical Chemistry B* **2003**, *107*, 4111–4117.

Work Experience

Jun 2009 - present	research and teaching assistant
	Ludwig-Maximilians-Universität München
	research and supervision of lab courses, tutorials, and internships
	in the group of Prof. T. Bein, Physical Chemistry
Apr 2007 - Aug 2008	teaching assistant
	tutorial to lectures physical chemistry I
	(Prof. Dr. Wintterlin, LMU Munich)
Dec 2006 - Mar 2007	temporary student employee
	Max-Planck-Institute for physics, Munich
	group for experimental physics of Prof. Dr. Kiesling
	data analysis from H1 experiment
	at 'Deutsches Elektronen-Synchrotron', Hamburg
Oct 2006 - Dec 2008	service employee
	Mise en Place Germany GmbH (gastronomy employment-agency)
Jul 2005 - Sept 2005	laboratory assistant
	Roche Diagnostics GmbH, Penzberg
	analytical test with real-time pcr
Jul 2003 - Sept 2003	laboratory assistant
	Roche Diagnostics GmbH, Penzberg

Skills and Competences

Languages	German (native speaker), English (fluent)
IT knowledge	Good knowledge: Microsoft Windows, Microsoft Office
	Basic knowledge: Origin, LateX
Image Processing	Basic knowledge : Adobe Photoshop, Adobe Illustrator
	Inkscape, Gimp, ImageJ, POVray
Characterization techniques	Responsible Person for: HPLC and Thermal Evaporator,
	AFM, Contact-Angle Measurements,
	Impedance Spectroscopy (Capacitance Measurement), Spin Coater

Further Education	Project Management workshop (Dr. Lukas von Hippel)
	workshop "Presentation Skills"
	(LMU Graduate Center, Ms. Sabine Lerch)
	workshop "Communication and Teams"
	(LMU Graduate Center, Ms. Sabine Lerch)

Appendix B

Publications and Presentations

Publications

Mandlmeier, B.; Minar N. K.; Feckl, J. M.; Fattakhova-Rohlfing, D.; Bein, T. "Tuning the crystallinity parameters in macroporous titania films" *Journal of Materials Chemistry A* **2014**, *2*, 6504–6511.

Docampo, P.; Hanusch, F.; Stranks, S. D.; Döblinger, M.; Feckl, J. M.; Ehrensperger, M.; Minar, N. K.; Johnston, M. B.; Snaith, H. J.; Bein, T. "Solution Deposition-Conversion for Planar Heterojunction Mixed Halide Perovskite Solar Cells" *Advanced Energy Materials* **2014**, *4*, 14, 1400355.

Minar, N. K.; Kun, H.; Westermeier, C.; Döblinger, M.; Schuster, J.; Hanusch, F. C.; Nickel, B.; Ozin, G. A.; Bein, T. "A Highly-Ordered 3D Covalent Fullerene Framework" submitted to *Angewandte Chemie*, November 2014.

Minar, N. K.; Docampo, P.; Fattakhova-Rohlfing, D.; Bein, T. "Guided In-Situ Polymerization Into a Mesoporous Metal Oxide" *ready for submission.*

Minar, N. K.; Bein, T. "Fullerenol-based Organosilica" *in preparation.*

Minar, N. K.; Auras, F. A.; Li, Y.; Inagaki, S.; Bein, T. "Periodic mesoporous

Organosilica from benzothiadiazole-precursor" *in preparation.*

Presentations

N. K. Minar, J. M. Szeifert, T. Bein, Poster presentation "Assembly of Thin Mesoporous Titania Films for Hybrid Solar Cells" at the CeNS Workshop: Nanosciences: Merging Disciplines, Venice (Italy), 2010

F. Auras, N. K. Minar, J. M. Szeifert, A. Wochnik, C. Scheu, T. Bein, Poster presentation "Nanostructured Solid-State Solar Cells" at the CeNS Workshop: Nanosciences: Merging Disciplines, Venice (Italy), 2010

N. K. Minar, T. Bein, Poster presentation "Filling the Pores: In-situ Polymerization of MEH-PPV into Porous Titania" at the 4th International Conference on 'Hybrid and Organic Photovoltaics' (HOPV), Uppsala (Sweden), 2012

N. K. Minar, K. Hou, F. Hanusch, T. Bein, Poster presentation "Highly Ordered Mesoporous Fullerene Polymer" at the CeNS Workshop: Nanosciences: Soft, Solid, Alive and Kicking, Venice (Italy), 2012

N. K. Minar, K. Hou, M. Döblinger, F. Hanusch, T. Bein, Poster presentation "Highly Ordered Mesoporous Fullerene Framework" at the 25th German Zeolite Conference (DZT), Hamburg (Germany), 2013

N. K. Minar, K. Hou, M. Döblinger, F. Hanusch, T. Bein, Oral presentation "Highly Ordered Mesoporous Fullerene Framework" at the 17th International Zeolite Conference (IZC), Moscow (Russia), 2013

N. K. Minar, K. Hou, F. Hanusch, T. Bein, Poster presentation "Highly Ordered Mesoporous Fullerene Polymer" at the Solar Technologies Go Hybrid Conference - Nanosystems for Solar Energy Conversion, Munich (Germany), 2013

N. K. Minar, K. Hou, C. Westermeier, M. Döblinger, F. Hanusch, B.Nickel, T. Bein, Poster presentation "Highly Ordered Pure Fullerene PMO" at the III International

Conference - Solar Technologies Go Hybrid Conference, Wildbad Kreuth (Germany), 2014